

Growth and Characterization of cubic III-Nitrides by Molecular Beam Epitaxy

*Wachstum und Charakterisierung
kubischer III-Nitride mittels
Molekularstrahlepitaxie*

Dissertation

zur Erlangung des Doktorgrades der
Naturwissenschaften (Dr. rer. nat)

vorgelegt dem Fachbereich 07
der Justus-Liebig-Universität Gießen

von Mario Fabian Zscherp

November 2023

Erstgutachter: Prof. Sangam Chatterjee, Ph.D.
Zweitgutachter: PD Dr. Matthias T. Elm
Eingereicht: 01.11.2023
Disputation: 14.12.2023

Abstract

The increasing performance demands for next-generation optoelectronics require materials which are capable of efficient light emission at high drive currents for all visible wavelengths. Cubic group III-nitrides are promising contenders to fulfill this task, because they lack internal polarization fields and promise to cover large parts of the electromagnetic spectrum. The ternary c-In_xGa_{1-x}N alloys are particularly interesting as their band gap can be tuned from the near-ultraviolet to the near-infrared.

Their potential application in semiconductor devices demands the fabrication of high-quality thin films with smooth surfaces and low defect densities. However, the metastability of the cubic zincblende phase and the lack of suitable substrates limit the crystal quality of epitaxially grown c-III-nitrides. In addition, the growth of c-In_xGa_{1-x}N across the complete composition range has been deemed impossible due to an extensive miscibility gap for intermediate In contents. As a result, scientific publications investigating c-In_xGa_{1-x}N with In contents above 30% are scarce.

The main contributions of this dissertation focus on improving the layer quality of cubic III-nitrides and enabling the growth of c-In_xGa_{1-x}N with any In content using plasma-assisted molecular-beam epitaxy. **Publication 1** addresses the quality aspect by evaluating the impact of a c-AlN buffer layer on the growth of c-GaN on 3C-SiC. The buffer layer significantly improves the c-GaN layer quality and reduces defect density, surface roughness and hexagonal inclusions. Beyond the mere quality improvement, this is crucial for obtaining good c-GaN pseudo substrates for the subsequent growth of other III-nitrides. Subsequently, **publication 2** achieves the growth of phase pure cubic In_xGa_{1-x}N over the entire composition range. The experimental results suggest that strain prevents the spinodal decomposition and reveal CuPt-like ordering for intermediate alloy compositions. Finally, it demonstrates light emission from the thin films ranging from ultraviolet to infrared and convincingly determines the emission energy as a function of composition.

These results open up new research avenues towards materials properties of previous inaccessible compositions as well as towards device realization. This includes the fabrication of multi quantum well structures and the evaluation of their emission efficiency.

Zusammenfassung

Die steigenden Leistungsanforderungen optoelektronischer Bauteile der nächsten Generation verlangen nach Materialien, die bei hohen Betriebsströmen zu effizienter Emission von Licht im gesamten sichtbaren Spektralbereich fähig sind. Kubische Gruppe III-Nitride sind für das Erfüllen dieser Herausforderung vielversprechend, da sie keine internen Polarisationsfelder haben und weite Teile des elektromagnetischen Spektrums abdecken können. Die ternäre $c\text{-In}_x\text{Ga}_{1-x}\text{N}$ Legierung ist dabei von besonderem Interesse, da ihre Bandlücke vom ultravioletten bis infraroten Spektralbereich durchgestimmt werden kann.

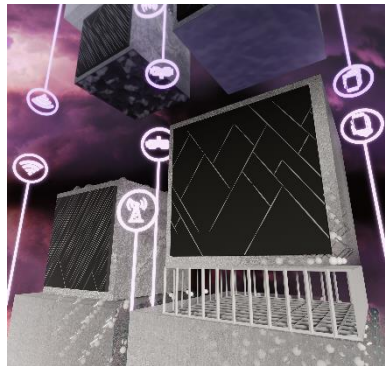
Ihre potenzielle Anwendung in Halbleiterbauteilen erfordert die Herstellung qualitativ hochwertiger Dünnschichten mit glatten Oberflächen und geringen Defektdichten. Jedoch limitiert die Metastabilität der kubischen Zinkblendenphase und der Mangel an geeigneten Substraten die Kristallqualität epitaktisch gewachsener $c\text{-III-Nitride}$. Außerdem wird das Wachstum von $c\text{-In}_x\text{Ga}_{1-x}\text{N}$ über den gesamten Zusammensetzungsbereich, auf Grund einer Mischungslücke für mittlere In-Gehälter, als unmöglich angesehen. Aufgrund dessen gibt es nur sehr wenige wissenschaftliche Veröffentlichungen, die $c\text{-In}_x\text{Ga}_{1-x}\text{N}$ mit In Gehältern oberhalb 30% untersuchen.

Die wesentlichen Beiträge dieser Dissertation konzentrieren sich auf eine Verbesserung der Schichtqualität von kubischen III-Nitriden und darauf, das Wachstum von $c\text{-In}_x\text{Ga}_{1-x}\text{N}$ mit beliebigem In Gehalt mittels plasmaunterstützter Molekularstrahlepitaxie zu möglichn. **Publikation 1** widmet sich dem Qualitätsaspekt und untersucht den Einfluss einer $c\text{-AlN}$ Pufferschicht auf das Wachstum von $c\text{-GaN}$ auf 3C-SiC. Die Pufferschicht verbessert die $c\text{-GaN}$ Schicht signifikant und verringert Defektdichte, Oberflächenrauigkeit und Anzahl hexagonaler Einschlüsse. Des Weiteren ist dies wertvoll, um möglichst gute $c\text{-GaN}$ Pseudosubstrate für das Wachstum anderer III-Nitride zu erhalten. **Publikation 2** erreicht das Wachstum von phasenreinem, kubischem $\text{In}_x\text{Ga}_{1-x}\text{N}$ über den gesamten Zusammensetzungsbereich. Die experimentellen Ergebnisse legen nahe, dass die Verspannung zur Verhinderung von spinodaler Entmischung entscheidend ist und offenbaren CuPt-artige Ordnungseffekte für mittlere In Gehälter. Außerdem zeigt die Veröffentlichung eine durstimmmbare Lichemission von ultraviolet bis infrarot und bestimmt die Kompositionsabhängigkeit der Emissionsenergie.

Diese Ergebnisse eröffnen neue Forschungsmöglichkeiten sowohl zu Eigenschaften der zuvor nicht herstellbaren Verbindungen, als auch zur Anwendung in Bauelementen. Dies beinhaltet die Herstellung von Multiquantumtopfstrukturen und der Bestimmung der Emissionseffizienz.

List of publications & individual contribution

The following peer-reviewed research articles constitute the framework of this cumulative dissertation. The main messages and the author's contribution are listed below:



Publication 1:

Zscherp, M. F.; Mengel, N.; Hofmann, D. M.; Lider, V.; Ojaghi Dogahe, B.; Becker, C.; Beyer, A.; Volz, K.; Schörmann, J.; Chatterjee, S.

AlN Buffer Enhances the Layer Quality of MBE-Grown Cubic GaN on 3C-SiC.

Cryst. Growth Des. **2022**, 22 (11), 6786–6791.
<https://doi.org/10.1021/acs.cgd.2c00927>.

Cover artwork reproduced with permission from the American Chemical Society.

This publication investigates the impact of an AlN buffer layer on the crystal quality of epitaxially grown cubic GaN on 3C-SiC. Thorough characterization reveals that the buffer layer simultaneously improves the defect density, surface morphology and phase purity of cubic GaN thin films.

M. F. Zscherp conceived the experiments under supervision of J. Schörmann and S. Chatterjee. M. F. Zscherp fabricated the samples and characterized them using XRD, SEM and AFM with assistance of J. Schörmann. N. Mengel conducted the PL measurements, whereas V. Lider and B. Ojaghi Dogahe performed the STEM study. M. F. Zscherp interpreted the XRD, AFM and PL measurements and discussed the results with all co-authors. M. F. Zscherp wrote the manuscript with input from all co-authors.



Publication 2:

Zscherp, M. F.; Jentsch, S. A.; Müller, M. J.; Lider, V.; Becker, C.; Chen, L.; Littmann, M.; Meier, F.; Beyer, A.; Hofmann, D. M.; As, D. J.; Klar, P. J.; Volz, K.; Chatterjee, S.; Schörmann, J.

Overcoming the Miscibility Gap of GaN/InN in MBE Growth of Cubic $\text{In}_x\text{Ga}_{1-x}\text{N}$.

ACS Appl. Mater. Interfaces **2023**, *15* (33), 39513–39522. <https://doi.org/10.1021/acsami.3c06319>.

Cover artwork reproduced with permission from the American Chemical Society.

This publication demonstrates the successful growth of cubic $\text{In}_x\text{Ga}_{1-x}\text{N}$ over the entire composition range by plasma-assisted molecular-beam epitaxy. Photoluminescence measurements confirm the tunability of the emission energy from ultraviolet to infrared. X-ray diffraction, transmission electron microscopy and photoluminescence studies infer a strain-induced CuPt-like ordering for intermediate indium contents.

M. F. Zscherp conceived the experiments together with J. Schörmann and S. Chatterjee. M. F. Zscherp supervised the fabrication of the samples by S. A. Jentsch and conducted preliminary experiments to develop the methodology. M. F. Zscherp, S. A. Jentsch, M. J. Müller, M. Littmann, F. Meier, V. Lider and L. Chen characterized the c- $\text{In}_x\text{Ga}_{1-x}\text{N}$ samples using AFM, SEM, PL, XRD, STEM and Raman spectroscopy. M. F. Zscherp discussed the results with all co-authors and analyzed the role of strain and ordering. M. F. Zscherp wrote the bulk of the manuscript, which was edited by all co-authors.

Additionally, I authored the following publications in fully peer-reviewed journals that are not included in this work:

Zscherp, M. F.; Glaser, J.; Becker, C.; Beyer, A.; Cop, P.; Schörmann, J.; Volz, K.; Elm, M. T.

Epitaxial Growth and Structural Characterization of Ceria Deposited by Atomic Layer Deposition on High-Surface Porous Yttria-Stabilized Zirconia Thin Films.

Cryst. Growth Des. **2020**, *20* (4), 2194–2201. <https://doi.org/10.1021/acs.cgd.9b01112>.



Zscherp, M. F.; Bastianello, M.; Nappini, S.; Magnano, E.; Badocco, D.; Gross, S.; Elm, M. T.

Impact of Inversion and Non-Stoichiometry on the Transport Properties of Mixed Zinc-Cobalt Ferrites.

J. Mater. Chem. C **2022**, *10* (8), 2976–2987.
<https://doi.org/10.1039/dltc05871a>.

Cover artwork reproduced with permission from the Royal Society of Chemistry.

Furthermore, I wrote or contributed to the following conference proceedings which were subject to committee peer-review:

Zscherp, M. F.; Jentsch, S. A.; Müller, M. J.; Littmann, M.; Meier, F.; Hofmann, D. M.; As, D. J.; Chatterjee, S.; Schörmann, J.

Growth of Cubic $In_xGa_{1-x}N$ over Whole Composition by MBE.

Proc. SPIE 12421, Gall. Nitride Mater. Devices XVIII **2023**, No. 124210B.
<https://doi.org/10.1117/12.2648296>.

Schörmann, J.; Zscherp, M. F.; Mengel, N.; Hofmann, D. M.; Lider, V.; Ojaghi Dogahe, B.; Becker, C.; Beyer, A.; Volz, K.; Chatterjee, S.

Impact of AlN Buffer Layers on MBE Grown Cubic GaN Layers.

Proc. SPIE 12421, Gall. Nitride Mater. Devices XVIII **2023**, No. 1242103.
<https://doi.org/10.1117/12.2648960>.

Contents

Abstract	IV
Zusammenfassung	V
List of publications & individual contribution	VI
Publication 1:.....	VI
Publication 2:.....	VII
Contents.....	IX
List of abbreviations.....	X
Introduction.....	1
Fundamentals.....	3
Cubic group III-nitrides	3
Strain and defects.....	7
Experimental Methods.....	10
Molecular-beam epitaxy.....	10
X-ray diffraction	13
Basic scans	13
Reciprocal space maps	15
Other measurement techniques.....	18
Atomic force microscopy	18
Scanning electron microscopy	18
Photoluminescence spectroscopy	19
Raman spectroscopy	19
Scanning transmission electron microscopy	20
Results	21
Publication 1.....	21
Publication 2.....	28
Conclusion & Outlook.....	39
Bibliography	41
Appendix.....	52
Selbstständigkeitserklärung.....	56
Danksagung	57

List of abbreviations

AFM	atomic force microscopy
BEP	beam equivalent pressure
c-	cubic
h-	hexagonal
III-nitride	group III-nitride
LED	light-emitting diode
PAMBE	plasma-assisted molecular-beam epitaxy
PL	photoluminescence
SEM	scanning electron microscopy
SF	stacking fault
STEM	scanning transmission electron microscopy
RHEED	reflection high-energy electron diffraction
RMS	root-mean-square
UHV	ultra-high vacuum
XRD	X-ray diffraction

Introduction

Group III-nitrides and their alloys are frontrunner materials for a plethora of future-shaping applications such as ultra-fast transistors¹⁻³, ultraviolet light-emitting diodes (LED) for water disinfection^{4,5} and micro-LEDs⁶⁻¹⁰. The ternary alloy $\text{In}_x\text{Ga}_{1-x}\text{N}$ sparks particular interest as its emission energy can be tuned across the entire visible spectrum¹¹⁻¹⁷. This could enable the fabrication of multi-color emitters replacing phosphor down-converters towards more efficient white LEDs¹⁸. Currently, III-nitrides are almost exclusively applied in the thermodynamically stable wurtzite phase. However, the radiative recombination rate of LEDs based on wurtzite $\text{In}_x\text{Ga}_{1-x}\text{N}$ is reduced due to internal spontaneous polarization fields¹⁹⁻²³. The strength of these fields increases with the In content and causes a severe efficiency droop for green and amber-colored LEDs^{22,24,25}.

In contrast, the metastable zincblende phase possesses no such fields²⁶⁻²⁹ because of its cubic symmetry. This renders cubic $\text{In}_x\text{Ga}_{1-x}\text{N}$ a prime contender for closing the green and amber gap. However, the heteroepitaxial growth of cubic III-nitrides faces several challenges: In general, the metastability of the zincblende phase results in a narrow window of growth parameters. The lack of suitable substrates with a matching lattice constant and high crystal quality increases the density of structural defects in the material. For the c- $\text{In}_x\text{Ga}_{1-x}\text{N}$ alloy, the differences of the two binary compounds in interatomic spacing^{15,30} and growth temperature add more challenges to the epitaxial growth. Furthermore, several publications suggest a miscibility gap for intermediate In contents ($0.3 \leq x(\text{In}) \leq (0.7)$ ^{31,32}, backed by reports of spinodal decomposition into Ga-rich and In-rich phases³³⁻³⁵. Correspondingly, the In content of previous works on c- $\text{In}_x\text{Ga}_{1-x}\text{N}$ rarely exceeds 30%, leaving more than half of the alloys' compositions unexplored.

This dissertation advances the growth and characterization of cubic nitrides with a focus on the c- $\text{In}_x\text{Ga}_{1-x}\text{N}$ alloy which embodies both, the biggest challenges as well as the greatest potential of cubic nitrides. More specifically, this work unlocks the entire composition of c- $\text{In}_x\text{Ga}_{1-x}\text{N}$ and systematically investigates the impact of the In content on the structural and optical properties.

The contributions of this dissertation towards achieving this goal can be divided into two parts. Each part explores the optimization of one aspect of the growth of c- $\text{In}_x\text{Ga}_{1-x}\text{N}$ on c-GaN by plasma-assisted molecular-beam epitaxy (PAMBE). The first part is dedicated to fabricating ideal c-GaN pseudo-substrates, whereas the second part attends to the growth of c- $\text{In}_x\text{Ga}_{1-x}\text{N}$.

Publication 1 demonstrates the impact of a c-AlN buffer layer on the growth of c-GaN on 3C-SiC/Si pseudo substrates. The buffer layer spatially separates the change of ionicity and lattice mismatch between c-GaN and 3C-SiC, and improves the crystal quality, roughness, and phase purity of c-GaN. This is vital for the quality of the c-In_xGa_{1-x}N because imperfections of the substrates tend to propagate into the epitaxially grown layer above.

Publication 2 utilizes these c-GaN/AlN/3C-SiC/Si templates and focuses on the growth of the c-In_xGa_{1-x}N layer. A sophisticated control of the growth parameters and strain enables the growth of phase pure c-In_xGa_{1-x}N over the entire composition range. Structural and optical characterization provides evidence of a CuPt-like ordering for those previously inaccessible intermediate In contents. Further, this work conclusively demonstrates the tunability of the emission energy from the ultraviolet to the infrared spectral range without a miscibility gap.

The achieved full miscibility of c-GaN and c-InN encourages further development of c-In_xGa_{1-x}N as a material system for multi-color light-emitters. Furthermore, the relatively smooth surface morphology is crucial for progressing toward the fabrication of quantum well structures. Moreover, the concepts leading to the enhanced growth of c-GaN and c-In_xGa_{1-x}N, such as introducing a buffer layer and the benefits of strain, are universally applicable to other materials. A transfer of these approaches could open the synthesis of other previously unexplored materials.

This dissertation is written in cumulative form and structured in the following way. First, it describes the basic properties of group III-nitrides and their main applications, explains the intrinsic advantage of the cubic crystal structure, and summarizes the current state of literature on cubic III-nitrides. Secondly, it gives an overview of the concepts of lattice mismatch and strain, and the formation of extended defects. Furthermore, it introduces the experimental techniques of this work with a focus on molecular-beam epitaxy and X-ray diffraction. The next section consists of the original publications that include the results of this cumulative dissertation. The last section summarizes and concludes the central findings of this dissertation and provides an outlook on future research.

Fundamentals

This chapter covers the fundamental topics of this dissertation. The first section introduces cubic group III-nitrides and contextualizes the results of this dissertation. The second section briefly explains lattice mismatch, strain and defect formation. Those are crucial concepts for interpreting the properties of epitaxially grown semiconductor thin films.

Cubic group III-nitrides

Group III-nitrides such as AlN, GaN, InN, and their alloys are crucial semiconductor materials for the current and next generation of (opto-) electronic technologies. The relevant crystal structures of the III-nitrides are the hexagonal wurtzite and the cubic zincblende modification. This section introduces the advantages and limitations of both phases and evaluates the status of cubic III-nitrides as a research topic.

At present, virtually all III-nitride based devices feature the thermodynamically stable hexagonal phase, because of its superior crystal quality. Recently, h-(Al)GaN based transistors gained popularity because they benefit from high breakdown fields^{1,2,36}, high switching frequency^{3,36} and are more efficient³ than conventional Si-based devices for high power applications such as battery charging in electric vehicles and mobile devices³⁷. Furthermore, h-In_xGa_{1-x}N is omnipresent as the active region material of efficient and bright, blue LEDs³⁸⁻⁴⁰. This breakthrough was awarded the 2014 Nobel prize in physics⁴¹. Blue h-In_xGa_{1-x}N emitter are also used in phosphor down-conversion white-light LEDs⁴². In principle, h-In_xGa_{1-x}N based LEDs could cover the entire visible part of the electromagnetic spectrum⁴³. Table 1 presents the band gaps and lattice parameters of the binary III-nitride compounds.

Table 1 Properties of cubic and hexagonal group-III-nitrides. Band gap, lattice parameters and spontaneous polarization of AlN, GaN and InN.

III-N	h-AlN	c-AlN	h-GaN	c-GaN	h-InN	c-InN
E_{gap} [eV]	6.25 ⁴³	5.4 ⁴³	3.51 ⁴³	3.299 ⁴³ 3.295 ¹³	0.78 ⁴³	0.61 ¹⁵ 0.62 ¹⁶
a [\AA]	3.112 ⁴³	4.373 ⁴⁴	3.189 ⁴³	4.51 ⁴⁵ 4.505 ³⁰	3.545 ⁴³	5.01 ¹⁵
c [\AA]	4.982 ⁴³	–	5.185 ⁴³	–	5.703 ⁴³	–
Spontaneous polarization [C/m ²]	-0.090 ⁴⁶	–	-0.034 ⁴⁶	–	-0.042 ⁴⁶	–

The band gap energies of h-GaN and h-InN range from the near-ultraviolet to the near-infrared. However, the radiant recombination rate of those devices decreases rapidly with increasing indium content which is necessary for green and amber-colored emission²⁵. This leads to a decrease in efficiency for high current densities, also referred to as “efficiency droop”. This efficiency droop originates in internal polarization fields^{19,20} of the hexagonal wurtzite structure, which separate electrons and holes²¹, decreasing the wave-function overlap and thus the rate of radiative recombination.

The wurtzite structure consists of two hexagonal close-packed sublattices, one for each atom group, which are shifted by 5/8 in [0001] direction (Figure 1a). Every group III atom is coordinated by four N-atoms forming a tetrahedron with the III-atom in its center. Each III-N bond corresponds to a local dipole moment due to the difference in electronegativities. In an ideal wurtzite lattice, the orientation of the bonds and thus, their dipole moments are such that the net dipole moment of the tetrahedron is zero²⁰.

However, the ratios of the hexagonal lattice constants a and c of III-nitrides deviate from the ideal wurtzite structure⁴⁷. This causes an anisotropy of the bond lengths d_z in [0001] direction and generates spontaneous polarization fields⁴⁸⁻⁵¹. The anisotropy and therefore the strength of the internal field in h-In_xGa_{1-x}N increases with the indium content^{24,46} (Table 1). Hence, the ratio of radiative recombination decreases, resulting in the “green and amber gap”.

Figure 1b depicts the zincblende structure, which exhibits a higher level of symmetry. Like the wurtzite phase, the zincblende structure features two cubic close-packed sublattices, shifted by 1/4 along the [111] direction. Here, all bond lengths d are equal, and the local dipoles are symmetrically ordered. Thus, the zincblende structure has no internal polarization fields and no separation of electrons and holes occurs. Therefore, cubic III-nitrides are particularly promising for optoelectronic applications, as they are free from internal fields and offer the same flexibility in band gap energies as hexagonal III-nitrides (Table 1).

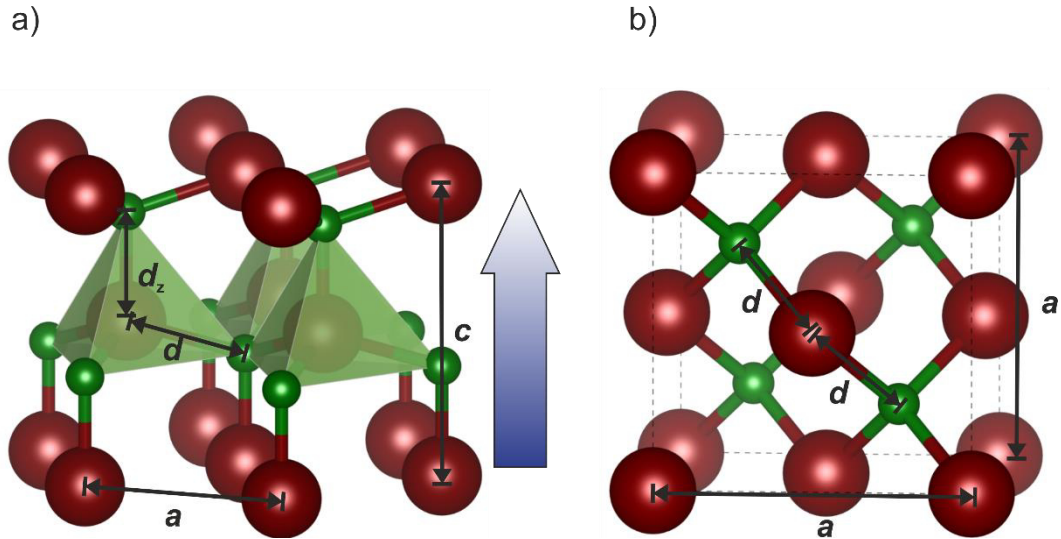


Figure 1 Crystal structures of group III-nitrides. a) Stick-and-ball model of a III-nitride wurtzite structure where the red (green) balls represent group-III (nitrogen) atoms. In III-nitrides the wurtzite structure is distorted with $d > d_z$, which causes spontaneous polarization fields (blue arrow). b) Stick-and-ball model of a III-nitride zincblende structure which possess no such internal fields due to its cubic symmetry. This figure was created using VESTA 3 software⁵².

However, the inferior structural quality of epitaxially grown samples limits their application. Major challenges of cubic group III-nitrides are the metastability of the zincblende phase, a narrow set of growth parameters and a lack of suitable substrates. Overall, the research activity on the topic of cubic nitrides peaked in the 1990s²¹ and declined after several breakthroughs in the field of hexagonal nitrides. Nonetheless, the potential benefits of fabricating devices based on the cubic phase remain important considering the intrinsic limitations of the hexagonal phase. The following section evaluates the state of the research on cubic nitrides and the contributions made in this work.

Cubic GaN is the most researched and advanced material of the c-III-nitrides. It is often used as a pseudo substrate for other cubic nitrides or the starting material for ternary alloys. Previous research efforts have investigated the role of growth parameters^{53–62,63}, the effect of layer thickness^{30,64,65}, as well as impact of stacking faults^{14,64,65} and their origin^{66–68}, to increase the layer quality of c-GaN. However, the quality of heteroepitaxially grown c-GaN thin films is still not satisfactory and significant hexagonal inclusions are common.

For the other binary compounds, c-AlN and c-InN the research activity is significantly lower. Some publications report the growth of cubic AlN^{44,57,69–71} and sporadically mention its use as a buffer layer for c-GaN^{56,58,64,72,73}. Only recently a publication explicitly investigated the impact of such a buffer layer grown by chemical vapor deposition⁷⁴. The fabrication of c-InN requires low process temperatures to avoid decomposition¹⁵, which hampers the use of some growth techniques, such as chemical vapor deposition. Reports that used plasma-

assisted molecular-beam epitaxy achieved the growth of phase pure c-InN^{15-17,75,76}, but the crystal quality is inferior to that of c-GaN.

The ternary alloy c-In_xGa_{1-x}N received substantial attention due to its potential application as a light-emitting material. However, the bulk part of c-In_xGa_{1-x}N-related publications does not exceed indium contents of 0.3^{26,27,29,77-84}. Only a few research papers report c-In_xGa_{1-x}N layers with higher In contents⁸⁵⁻⁸⁹, which are often very thin⁸⁶⁻⁸⁸ or not phase pure^{85,89}. Other works observe^{33-35,90} or predict^{31,32} spinodal decomposition into Ga-rich and In-rich phases. The spinodal decomposition is mainly driven by the difference in lattice constants of approximately 10%³². As a result, many composition-related properties of c-In_xGa_{1-x}N, such as the emission energy or the band gap energy, are not fully quantified but remain rather extrapolated.

Overall, the major roadblocks of the cubic III-nitrides are the inferior layer quality compared to the hexagonal phase and the presumed miscibility gap of cubic GaN and InN. **Publication 1** contributes towards increasing the layer quality of cubic III-nitrides, whereas **publication 2** demonstrates full miscibility of phase pure c-In_xGa_{1-x}N. This could rekindle the interest of the nitride community in the cubic phase, specifically for c-In_xGa_{1-x}N with indium contents whose light emission are most affected by the efficiency droop in wurtzite-based devices.

Strain and defects

The relation between the lattice dimensions of the substrate and the epilayer is one of the most crucial aspects of heteroepitaxy. Lattice mismatch is usually the main cause of structural defects in crystalline thin films with otherwise optimized growth parameters. The following section discusses fundamental mismatch-related phenomena in a crystal lattice, such as strain and extended defects.

In a heteroepitaxial system consisting of a cubic substrate with a lattice constant a_{sub} and a cubic epilayer with a lattice constant a_{epi} , the lattice mismatch f is defined as⁹¹

$$f = \frac{a_{\text{epi}} - a_{\text{sub}}}{a_{\text{sub}}}.$$
 (1)

Given sufficient crystallinity of both layers, this mismatch leads to elastic deformation of the crystal lattice of the epitaxial layer known as strain. Figure 2 illustrates three scenarios for the interface of substrate and epitaxial layer with $a_{\text{epi}} > a_{\text{sub}}$: strained, partially relaxed and relaxed.

a) strained epilayer b) partially relaxed epilayer c) relaxed epilayer

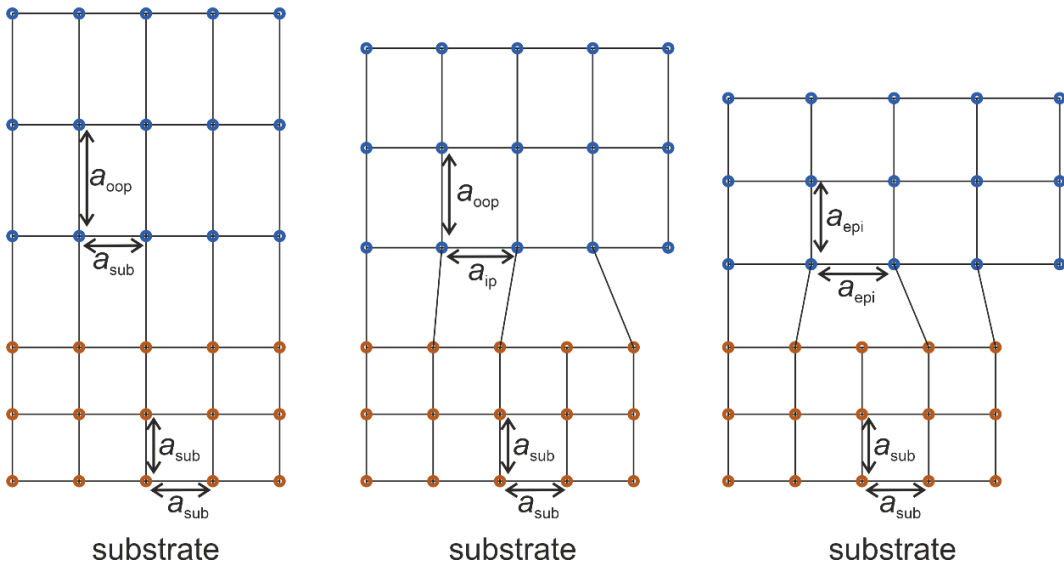


Figure 2 Epilayer-substrate interface. a) Fully strained, b) partially relaxed, and c) fully relaxed epilayer on a relaxed substrate. The lattice of the strained epilayer is tetragonally distorted, whereas relaxation occurs under defect formation.

If the epitaxial layer is fully strained (Figure 2a), the in-plane lattice constant a_{ip} equals a_{sub} . As a result, the crystal lattice of the epitaxial layer is tetragonally distorted. a_{ip} is smaller and the out-of-plane lattice constant a_{oop} is larger than the natural lattice constant a_{epi} . The correlation between the reduction of a_{ip} and

the expansion of a_{oop} is usually not one-to-one and varies depending on the elastic constants of the crystal lattice.

The uniaxial out-of-plane strain ε_{oop} describes the distortion of the epilayers' crystal lattice in the growth direction:

$$\varepsilon_{oop} = \frac{a_{oop} - a_{epi}}{a_{epi}}. \quad (2)$$

Naturally, this elastic distortion increases the lattice energy. The crystal lattice can relax toward the natural lattice constant a_{epi} under the formation of defects to relieve energy. The critical thickness of the epitaxial layer after which relaxation occurs mainly depends on the lattice mismatch⁹². Figure 2c shows the scenario of a fully relaxed epilayer, whereas Figure 2b depicts the intermediate case of a partially relaxed layer. The degree of relaxation R of the epitaxial layer in respect to the substrate is described by⁹¹

$$R = \frac{a_{ip} - a_{sub}}{a_{epi} - a_{sub}}. \quad (3)$$

This relaxation requires the formation of misfit dislocations at the substrate–epilayer interface to match the deviating lattice constants. Figure 3a schematically depicts a cross-section of such a dislocation.

a) misfit dislocation b) edge-type c) screw-type

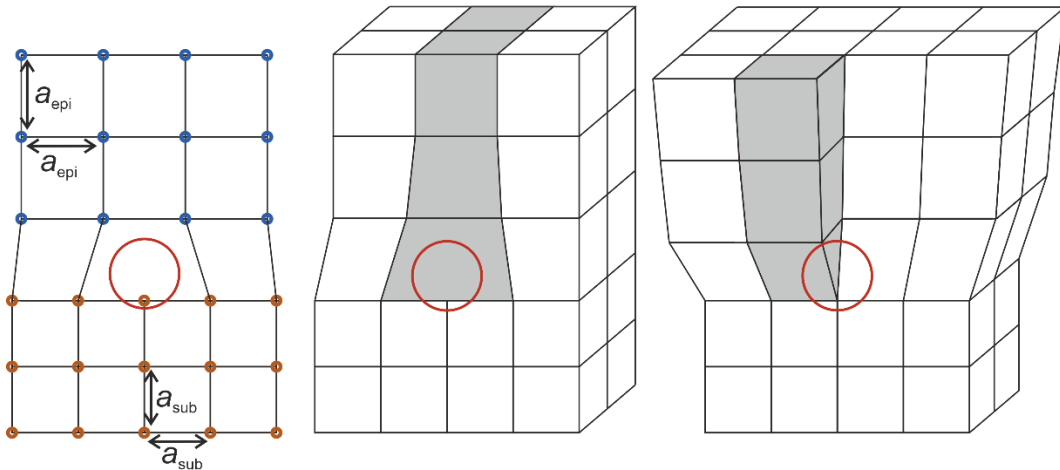


Figure 3 Defect formation at epilayer–substrate interface. a) Cross-section of a misfit dislocations due to lattice mismatch. In 3D, dislocations are either b) edge-type or c) screw-type.

In an extended crystal, dislocations are line defects which are divided into edge-type (Figure 3b) and screw-type (Figure 3c) dislocations. Threading dislocations are dislocations that propagate through the crystal lattice and are the most detrimental defect type in hexagonal wurtzite III-nitrides devices^{93–95}.

In contrast, stacking faults (SFs) are the predominant defects in cubic III-nitrides and have a negative impact on the device performance^{14,65}. A SF is a planar defect which constitutes a change of the cubic stacking sequence ABCABC in <111> direction. During epitaxial growth, stacking faults are usually introduced at imperfect interfaces such as atomic steps or during the coalescence of misaligned islands. The stacking sequence of wurtzite ABAB is very similar to the cubic sequence. Therefore, stacking faults may result in a wurtzite type sequence which can lead to the formation of hexagonal inclusions in the cubic crystal. In general, SFs propagate through the entire layer, sometimes originating in the substrate. However, two intersecting SFs with different inclination can annihilate under the formation of a dislocation^{64,66,67}. A similar reaction was predicted for the coalescence of threading dislocations^{30,96}. Therefore, the defect density typically declines with increasing film thickness. The dislocation densities of cubic nitrides can be estimated using X-ray diffraction^{30,97,98} and are typically in the order of $10^{9-11} \text{ cm}^{-2}$.

Lattice mismatch, strain and defects play major roles in the publications which frame this dissertation. In **publication 1**, an AlN buffer layer improves the substrate–epilayer interface. With buffer layer, SFs are more symmetrically distributed which enhances SF annihilation. In **publication 2**, the lattice mismatch between c-GaN and c-In_xGa_{1-x}N causes significantly strained c-In_xGa_{1-x}N layers. This strain stabilizes c-In_xGa_{1-x}N with intermediate In contents and prompts a CuPt-type ordering of In and Ga without phase separation.

Experimental Methods

This chapter describes the experimental techniques used to obtain the results of this dissertation. The first section covers molecular-beam epitaxy which I utilized to grow the cubic group III-nitride thin films. The second section explains the working principle of X-ray diffraction, as well as the different scan geometries used for the structural characterization of the epitaxially grown films. The last section briefly describes several other methods that substantially contributed towards the interpretation of the results.

Molecular-beam epitaxy

Molecular-beam epitaxy (MBE) is a physical vapor deposition technique and can produce highly crystalline thin films with sharp layer sequences and well controlled doping profiles. MBE employs ultra-high vacuum (UHV) conditions and uses elementary source materials which are available in high purity to ensure low contamination levels. The educt sources are arranged such that the reaction of the educts occurs primarily at the heated substrate surface to prevent gas phase reactions. The low background pressure and the constant supply of educts enable access to crystal phases beyond thermodynamically stable ones and achieve kinetically controlled growth.

The most important physical processes of the growth are desorption, adsorption and surface diffusion. Typical experimental setups manipulate these processes by controlling the substrate temperature T_{sub} , the surface properties of the substrate and beam flux of the educts.

Figure 4 shows the schematics of the MBE growth chamber (Riber Compact 12) that was used in this work to grow cubic III-nitrides. Three effusion cells supply the group III elements Al, Ga and In. The beam fluxes depend on the cell temperatures and can be calibrated using a moveable pressure gauge close to the sample position. The resulting pressure value is known as beam equilibrium pressure (BEP). In this setup, a radio-frequency plasma generator (Oxford Applied Research HD25) supplies reactive nitrogen species. Accordingly, this subtype of MBE is called plasma-assisted MBE (PAMBE). A turbomolecular pump and liquid nitrogen cryo shield ensure UHV conditions in the reaction chamber. Besides reducing contamination, the low background pressure allows the use of reflection high-energy electron diffraction (RHEED) for in-situ monitoring of the sample surface.

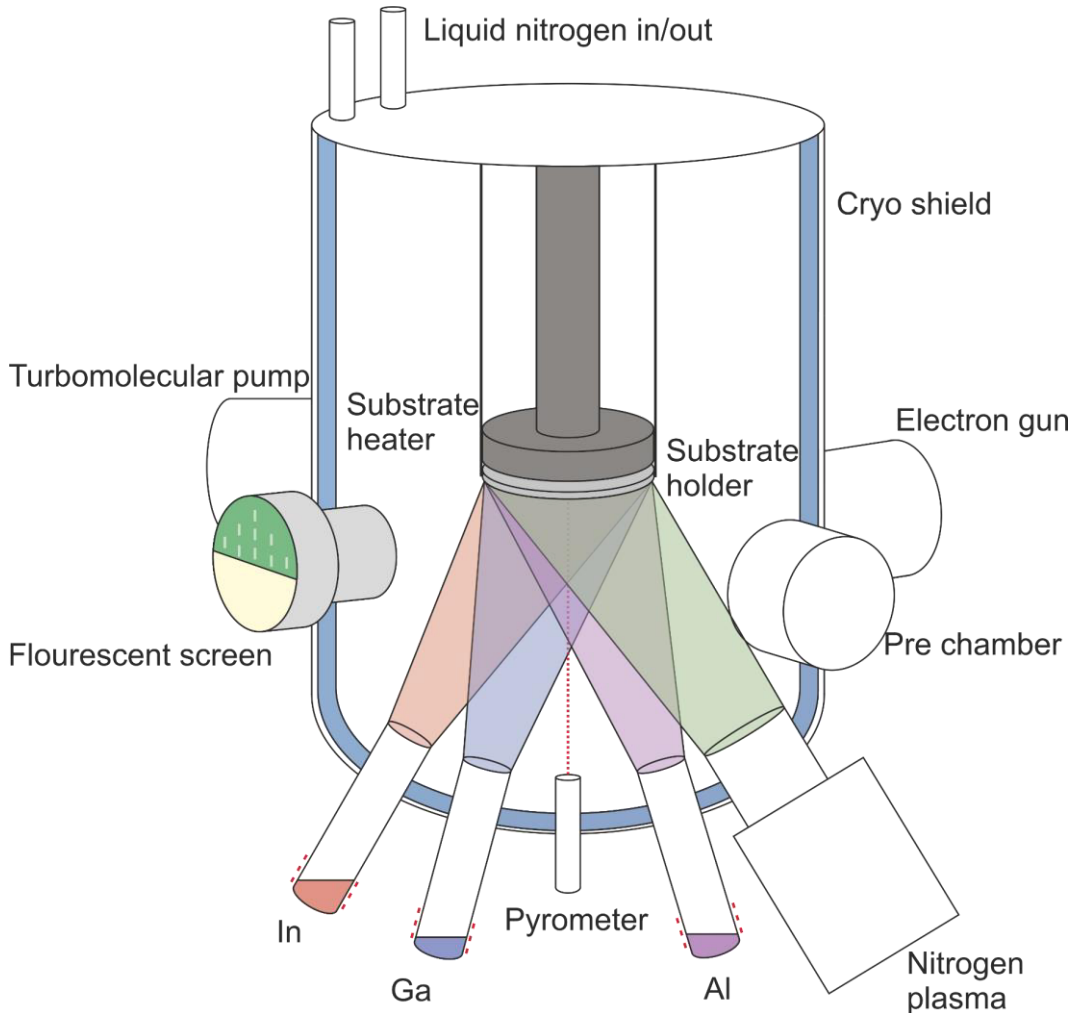


Figure 4 Schematics of the MBE main chamber. Orange, blue, purple and green shading represent the impinging materials fluxes.

RHEED is helpful for adjusting the metal-to-nitrogen ratio during the growth of cubic III-nitrides. For example, an excess of metal at the surface reduces the intensity of the diffracted electron beam on the fluorescence screen due to diffuse scattering. Therefore, measuring this intensity as a function of time during a growth interruption or in adsorption-desorption experiments provides a good understanding of the surface stoichiometry⁵⁹. For the growth of cubic III-nitrides, slightly metal-rich conditions lead to smoother surfaces and superior crystal quality, because a metal adatom layer forms, which favors layer-by-layer growth⁵⁸. Furthermore, the surface-sensitive RHEED pattern reveals the morphology of the growth front. A streaky diffraction pattern corresponds to a 2D like surface, whereas a spotty pattern infers 3D features⁹⁹. As a result, RHEED patterns are a good indication of whether the growth of the epilayer follows a layer-by-layer, island or combined island-layer growth mode.

The choice of substrate is another important aspect of MBE and a significant challenge for the heteroepitaxy of cubic III-nitrides. This work uses 3C-SiC (001)/Si pseudo substrates for the growth of cubic GaN, which generally

Experimental Methods

yield the best results of all substrates¹⁰⁰. This is in spite of a lattice mismatch of 3.4%^{45,101} and the presence of 3C-SiC anti-phase domains¹⁰². However, free-standing 3C-SiC substrates without anti-phase domains are currently not commercially available. Nevertheless, the lattice mismatch of other high-quality cubic substrates such as GaAs^{53,54,103} and MgO¹⁰⁴ is significantly higher and the layer quality of subsequently grown c-GaN inferior compared to 3C-SiC.

Overall, the available substrate options are not fully satisfactory, and the substrate–epilayer interface is a major cause for defect formation. To improve this interface, **Publication 1** introduces an AlN buffer layer between c-GaN and 3C-SiC and investigates its impact on the c-GaN layer quality. It is important to point out that the main function of the c-AlN buffer layer is not a reduction of the substrate–epilayer lattice mismatch. Indeed, the lattice constants of c-AlN and 3C-SiC are very similar^{44,101}. However, the ionicity of AlN¹⁰⁵ is higher than that of SiC but similar to GaN. Therefore, the buffer layer spatially separates the change of ionicity and the lattice mismatch, such that each buffer interface features only one kind of transition.

The lattice constant of cubic $\text{In}_x\text{Ga}_{1-x}\text{N}$, and correspondingly the lattice constant of an ideal substrate, varies with the indium content. Nonetheless, this work utilizes 600 nm thick c-GaN buffer layers for all In-compositions to ensure comparability.

The following subsection describes the growth sequence of the c- $\text{In}_x\text{Ga}_{1-x}\text{N}/\text{GaN}/\text{AlN}/\text{3C-SiC}/\text{Si}$ samples fabricated in this work. Prior to the growth of any III-nitride, the substrate was heated to $T_{\text{sub}} = 850$ °C and the so-called “Al flash” procedure was conducted to deoxidize the surface^{44,106–108}. For this procedure, the Al shutter ($\text{BEP}(\text{Al}) = 1.5 \cdot 10^{-8}$ mbar) was opened 5 times for 10 s each. The impinging Al reduces residual surface oxides under the formation of Al-suboxides, which decompose at the elevated temperatures. Afterwards, the temperature was reduced to $T_{\text{growth}} = 720$ °C for the growth of approximately 8 nm c-AlN and 600 nm c-GaN with a $\text{BEP}(\text{Al}) \approx 1.2 \cdot 10^{-7}$ mbar and $\text{BEP}(\text{Ga}) \approx 3 \cdot 10^{-7}$ mbar, respectively. The nitrogen plasma generator was operated at 200 W using a nitrogen flow of 0.7 sccm. For the subsequent growth of c- $\text{In}_x\text{Ga}_{1-x}\text{N}$, T_{growth} was lowered to 630–460 °C to enable indium incorporation. To obtain the target compositions, the metal BEPs were varied between $1.4 \cdot 10^{-8}$ and $1.1 \cdot 10^{-7}$ mbar for gallium and $9.2 \cdot 10^{-8}$ and $2.5 \cdot 10^{-7}$ mbar for indium. The thickness of the c- $\text{In}_x\text{Ga}_{1-x}\text{N}$ layers is 80–100 nm.

X-ray diffraction

X-ray diffraction (XRD) is a fundamental and versatile measurement technique for the structural characterization of crystalline materials. It can assess all lattice parameters, such as lattice constants, crystal symmetry, preferential orientation, phase purity, defects, mosaicity and strain. Furthermore, XRD is an extremely robust and reliable method because of its non-destructive nature and high instrumental precision. As a result, XRD is very prominent in the epitaxy community and is vital for the findings of this work. In **Publication 1**, XRD is used to examine the influence of the c-AlN buffer layer on the crystal quality and the number of hexagonal inclusions of the c-GaN epilayers. In **Publication 2**, XRD reciprocal space maps reveal the composition, the state of strain and the phase purity of c-In_xGa_{1-x}N layers.

In general, XRD measures the angular resolved diffraction pattern of incident X-rays which interact with the electrons of the periodic crystal lattice of the sample. The irradiated electrons emit their own, radially propagating electromagnetic field with the same wavelength and phase as the incident X-rays. These secondary waves form an interference pattern which is monitored by angular detector movements. According to the Laue condition $\mathbf{K} = \mathbf{q}$, constructive interference occurs when the scattering vector $\mathbf{K} = \mathbf{k}_{\text{incident}} - \mathbf{k}_{\text{diffracted}}$ matches a translation vector \mathbf{q} of the reciprocal lattice. Additionally, the diffraction of X-rays by the crystal lattice is often described as a reflection of the beam at the lattice planes, which are labeled by the Miller indices hkl. For constructive interference, the Bragg equation (4) describes the relation of the lattice plane spacing d_{hkl} and the angle θ between the lattice planes and the incident beam with the wavelength λ .

$$\lambda = 2d_{\text{hkl}} \sin(\theta). \quad (4)$$

Further parameters, such as the lattice constants can be derived from d_{hkl} , if the Miller indices h, k, l are known. For a cubic crystal lattice, the lattice constant a is given by:

$$a = d_{\text{hkl}} \sqrt{h^2 + k^2 + l^2}. \quad (5)$$

Basic scans

This work utilized several XRD measurement modes to obtain comprehensive information on the crystal lattice of the epitaxially grown layers. Figure 5 visualizes the different scan geometries for which θ and ω are the most relevant angles. The so-called Bragg angle θ denotes the angle between the incident X-rays and the lattice planes. To detect the diffracted beam, the angle between the incident beam and the detector must be twice this angle and is therefore

called 2θ . Additionally, ω is introduced for thin film XRD to describe the angle between incident X-rays and the sample surface. If the lattice planes (hkl) are aligned parallel to the sample surface, the reflection is called symmetric because θ equals ω (Figure 5a). Correspondingly, ω must differ from θ when measuring other, asymmetric lattice directions (Figure 5b). This ω -offset equals the angle of intersection between the lattice plane and the surface. The reciprocal space is convenient to use for the visualization of the diffraction phenomena. In reciprocal space, (hkl) lattice planes are represented by a single point. Figure 5 connects the measurement geometries in real space and the diffraction phenomena in reciprocal space.

The 2θ - ω scan geometry couples the movements of 2θ and ω by a factor of two, such that the length of \mathbf{K} is varied while its direction remains the same. In Figure 5, blue arrows represent these movements and visualize how this scan probes the reciprocal space in a certain $[hkl]$ direction. For a crystalline thin film with a strictly cubic structure, a symmetric 2θ - ω scan allows quick assessment of the lattice constant using equation (4) and (5).

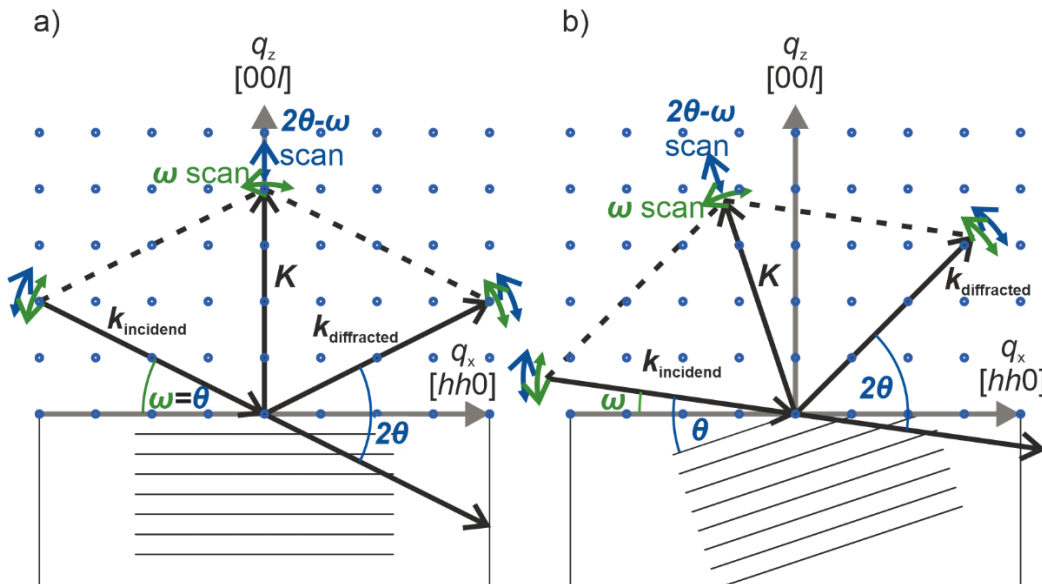


Figure 5 Scan geometries of basic XRD scans. a) Symmetric scan to assess lattice planes parallel to the surface. Blue (green) arrows indicate the movements to perform 2θ - ω scans (ω scans). b) Asymmetric scan geometry to measure surface-tilted planes.

When performing a ω -scan ("rocking curve"), the detector moves in skew-symmetry corresponding to a variation of the incident angle ω , as indicated by green arrows in Figure 5. In the reciprocal space, this changes the direction of \mathbf{K} but not its length and measures the broadening of the reciprocal lattice point. This broadening corresponds to the mosaicity and therefore crystal quality of an epitaxially grown thin film. The term "mosaicity" encompasses the spread in size, tilt and twist of grains within the thin film³⁰. Furthermore, microstrain and compositional inhomogeneities contribute to the broadening of a ω -scan.

Overall, measuring the linewidth $\Delta\omega$ of the rocking curve is a robust method to evaluate the crystal quality of an epitaxially grown layer. In thin films, mosaicity is associated with the formation of threading dislocations. Thus, it is common to use $\Delta\omega$ to estimate the threading dislocation density D_{TD} , assuming random orientation of grains, as given by^{30,97,98}

$$D_{TD} = \frac{(\Delta\omega)^2}{2\pi \cdot \ln 2 \cdot b_{TD}^2} \quad (6)$$

where b_{TD} is the Burgers vector of the dislocation with a value of $b_{TD} = a / \sqrt{2}$ and a is the lattice constant.

Reciprocal space maps

Reciprocal space maps combine several 2θ - ω scans at different ω angles to investigate an area section of the reciprocal space. The maps are either displayed in angular or reciprocal coordinates q_x , q_z ¹⁰⁹

$$q_x = \frac{2\pi}{\lambda} (\cos(2\theta - \omega) - \cos(\omega)) \quad (7)$$

and

$$q_z = \frac{2\pi}{\lambda} (\sin(2\theta - \omega) + \sin(\omega)). \quad (8)$$

The area scans detect misorientation, strain, composition and secondary phases which are difficult to find by line scans. In **publication 1**, reciprocal space maps around the (002) c-GaN reflection reveal that the AlN buffer layer drastically reduces the number of hexagonal inclusions. The amount is estimated using the intensity ratios of the wurtzite $\{-10-11\}$ and the zincblende (002) reflections. The space maps are crucial for this because the weak wurtzite reflections are in the vicinity of the c-GaN reflection but not intersecting the (002) 2θ - ω line scan.

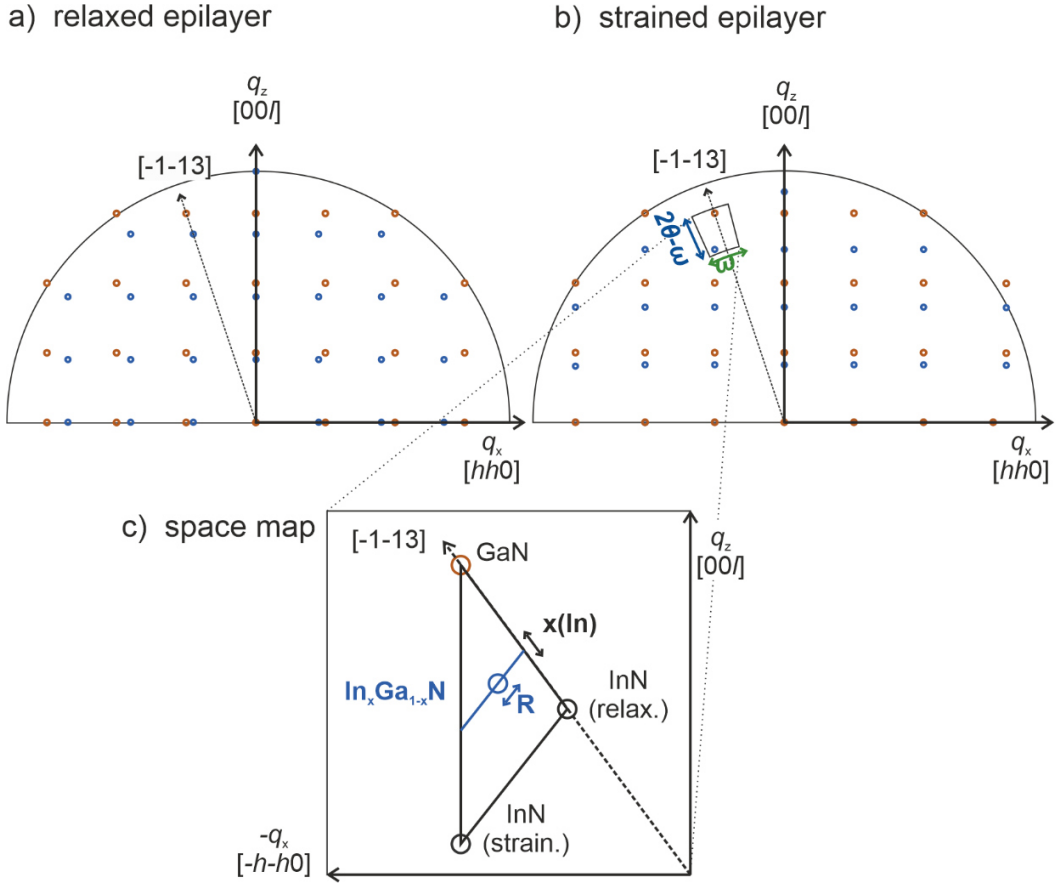


Figure 6 Reciprocal space of an heteroepitaxial material. a) Reciprocal space of a relaxed epilayer on a cubic substrate where blue (orange) dots represent the lattice planes of the epilayer (substrate). b) Reciprocal space of a strained epilayer with indications of the basic XRD scans that compose a space map. c) Schematic reciprocal space map around a $(-1-13)$ reflection of an $c\text{-In}_x\text{Ga}_{1-x}\text{N}$ layer grown on $c\text{-GaN}$. Geometric considerations yield the degree of relaxation R and the indium content $x(\text{In})$.

Furthermore, reciprocal space maps are particularly useful to understand the relation between substrate and an epitaxially grown layer. Figure 6 compares the reciprocal space of a relaxed and of a strained epitaxially-grown layer on a cubic substrate with $a_{\text{epi}} > a_{\text{sub}}$. Figure 6a presents the case of a relaxed, cubic epilayer. In the 2D projection of the reciprocal space, the points which represent the lattice planes (hkl) of the epilayer (blue) and the substrate (orange) both form a quadratic grid. The distance between these points in reciprocal space is inversely correlated to the lattice constants. In the scenario of Figure 6a, the reciprocal points of epilayer and substrate, which correspond to the same (hkl) , are connected by a dashed line along $[hkl]$. This is not the case for the strained epilayer (Figure 6b), because its crystal lattice is tetragonal distorted. Instead, the reciprocal points of the fully strained epilayer (blue) form a rectangular pattern. The change of the reciprocal coordinates q_x and q_z inversely mirrors the change of the real space lattice dimensions. In q_x direction, the spacing of the blue epilayer points increases such that layer and substrate are aligned, whereas

their spacing in q_z direction decreases. However, the distance in q_z between the blue epilayer and the orange substrate points increases.

Therefore, reciprocal space maps are convenient and precise tools for the quantification of strain and for determining the composition. In **publication 2**, reciprocal space maps around the asymmetric (-1-13) reflections of the c-GaN pseudo substrate and the c-In_xGa_{1-x}N epilayer are used for this purpose. The reciprocal coordinates of the fully strained and fully relaxed c-InN epilayer can be calculated using the elastic constants^{30,43,91,110}. Knowing those coordinates, the degree of relaxation and the composition can be obtained from simple geometric considerations. These are illustrated in Figure 6c, which overlays the position of the (-1-13) c-In_xGa_{1-x}N reflection, of the relaxed c-GaN, of the fully strained c-InN and of the fully relaxed c-InN. The binary compounds form a triangle that confines the position of the c-In_xGa_{1-x}N reflection. In Figure 6c, the blue line intersecting the c-In_xGa_{1-x}N reflection represents all possible reciprocal coordinates of c-In_xGa_{1-x}N with a certain x (In) and various degrees of relaxation. The position of the c-In_xGa_{1-x}N reflection on the blue line equals the degree of relaxation. Furthermore, the relaxed lattice constant can be obtained from the intersection of the blue line with the black line which connects c-GaN and c-InN (relaxed). The relaxed lattice constant translates directly to an indium content x (In) assuming that Vegard's law holds true for c-In_xGa_{1-x}N.

Additionally, the in-plane and out-of-plane lattice constants can be directly derived from the reciprocal space coordinates, q_x and q_z , of the c-In_xGa_{1-x}N reflection:

$$q_x = \frac{2\pi}{a_{ip}} \sqrt{h^2 + k^2} \quad (9)$$

and

$$q_z = \frac{2\pi}{a_{oop}} \sqrt{l^2}. \quad (10)$$

Consequently, the state of strain can be calculated using the lattice constants and the equations (2) and (3).

Two measurement instruments were used to acquire the diffraction data used in this work. Both instruments use a Cu K_{α1} ($\lambda = 1.54056$ Å) source with a Ge (220) monochromator and can perform additional tilting and rotating movements. The Panalytical X'Pert Pro MRD uses a conventional 1.6 kW sealed tube X-Ray source and 0D detector. In contrast, the Rigaku SmartLab diffractometer operates a 9-kW rotating anode source and a multi-dimensional pixel (HyPix3000) detector, which significantly shortens the measurement time for areal scans.

Additional measurement techniques

Atomic force microscopy

Atomic force microscopy (AFM) scans the surface morphology with high topological resolution^{111,112}. The measuring probe consist of a horizontal cantilever with a 10–50 nm sharp tip which faces the sample's surface. Piezoelectric elements control the cantilever movement in all directions. Attractive forces, such as van der Waals, electrostatic and magnetic forces bend the cantilever towards the sample. The deflection of the cantilever indicates the strength of the attractive forces and is measured by laser reflection. In general, the distance between the surface atoms of tip and sample determines the strength of the attractive forces and enables high topological resolution.

The simplest measurement mode is the static contact mode where the probe touches the surface and detects either the cantilever deflection or the required height adjustment to keep the deflection constant. Alternatively, a dynamic mode oscillates the cantilever and detects changes in frequency or amplitude^{111,112} and adjusts the cantilever height accordingly. This can be implemented with and without intermittent sample contact and significantly reduces the damage to sample and probe. In this work, a Bruker Multimode 8 was operated in a dynamic, non-contact mode using Bruker SCANASYST-AIR probes.

Scanning electron microscopy

Scanning electron microscopy (SEM) uses a focused electron beam to obtain high resolution images of a sample's surface. A set of magnetic and electrostatic condenser lenses, deflection coils and apertures control the shape, size and position of the scanning electron beam spot on the sample¹¹³. This enables fast imaging with a magnification that can be varied over several orders of magnitude. The electrons' wavelength is significantly lower than in optical systems due to acceleration voltages of several kV. Hence, the resolution of SEM is limited by spot size and the interaction volume but not by diffraction.

The interaction of the impinging electron beam and the sample produces various signals, such as secondary electrons, that are used for imaging. Secondary electrons, caused by inelastic scattering, are likely to be reabsorbed before reaching the detector and are therefore surface-sensitive. Their intensity depends on the topography and the sample's composition^{113,114}. Overlying the measured intensity with the beam position yields the secondary electron image, which resembles the sample's morphology. In this work, a JEOL JSM-7001F instrument was used to investigate the surface morphology complementary to AFM. Furthermore, images of samples' cross-section estimate the layer thicknesses of c-In_xGa_{1-x}N and c-GaN.

Photoluminescence spectroscopy

Photoluminescence spectroscopy (PL) is a fast and nondestructive characterization method measuring the sample's light emission after photoexcitation (Figure 7a). The absorption of a photon excites an electron from the valence band to the conduction band leaving a hole behind. Under Coulomb interaction, electron and hole form an electron-hole pair which is often called exciton. After excitation, the electron and the hole undergo various relaxation processes, mainly scattering with phonons, until they reach the band edges. There, the electron-hole pair can recombine directly or relax even further to a defect state with lower energy before recombining¹¹⁵. The electron-hole recombination can be radiative under photon emission or non-radiative where the transition energy dissipates in the form of phonons or Auger electrons. PL spectroscopy measures the emitted photons and assigns their energy signature to excitonic transitions, such as free or defect-bound excitons. This is useful to detect defects, evaluate their concentration and to determine the main emission energy of a material.

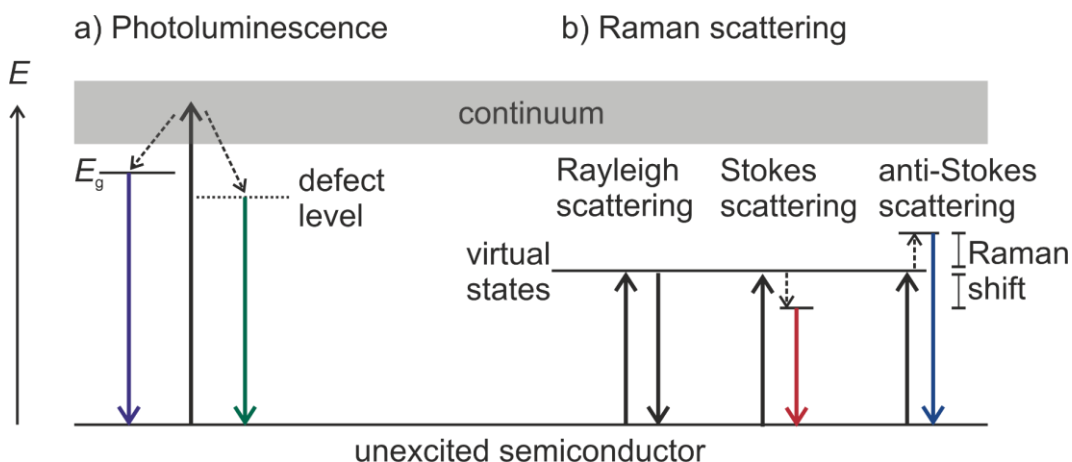


Figure 7 Optical spectroscopy. a) Basic principle of photoluminescence where radiative recombination occurs after photoexcitation. Full arrows represent optical transitions, whereas dotted arrows refer to relaxation processes. b) Energy level diagram of elastic and inelastic light scattering. Raman spectroscopy measures the difference in photon energy due to phonon interaction.

Raman spectroscopy

Raman spectroscopy measures the inelastic scattering of light by a material under emission or absorption of a phonon¹¹⁵. Figure 7b shows a simplified energy level diagram of the states involved in the Raman scattering process. The energy of the inelastically scattered photons can be lower or higher than that of an elastically scattered photon (Rayleigh scattering). Stokes scattering refers to a lowered photon energy, whereas anti-Stokes scattering denotes an increase in photon energy. The difference in energy (Raman shift) corresponds to the energy of the phonon involved in the scattering process. In semiconductor

Experimental Methods

physics, Raman spectroscopy investigates structural properties such as crystallinity, crystal orientation and composition.

Scanning transmission electron microscopy

Scanning transmission electron microscopy and energy-dispersive X-ray spectroscopy studies were conducted using an JEOL JEM-2200FS microscope in cooperation with AG Volz at Philipps-University Marburg.

Results

Publication 1

AlN Buffer Enhances the Layer Quality of MBE-Grown Cubic GaN on 3C-SiC

Zscherp, M. F.; Mengel, N.; Hofmann, D. M.; Lider, V.; Ojaghi Dogahe, B.; Becker, C.; Beyer, A.; Volz, K.; Schörmann, J.; Chatterjee, S.

Cryst. Growth Des. **2022**, 22 (11), 6786–6791

<https://doi.org/10.1021/acs.cgd.2c00927>

Reprinted with permission. Copyright 2022 American Chemical Society

AlN Buffer Enhances the Layer Quality of MBE-Grown Cubic GaN on 3C-SiC

Mario F. Zscherp, Nils Mengel, Detlev M. Hofmann, Vitalii Lider, Badrosadat Ojaghi Dogahe, Celina Becker, Andreas Beyer, Kerstin Volz, Jörg Schörmann, and Sangam Chatterjee*



Cite This: *Cryst. Growth Des.* 2022, 22, 6786–6791



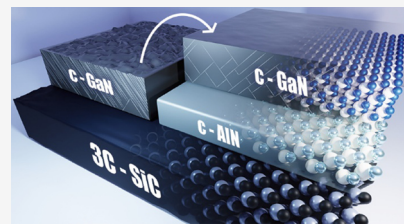
Read Online

ACCESS |

Metrics & More

Article Recommendations

ABSTRACT: Cubic nitrides are candidate materials for next-generation optoelectronic applications as they possess no internal fields and promise to cover large parts of the electromagnetic spectrum from the deep UV toward the mid-infrared. Their successful application demands high-quality epitaxial growth of c-GaN as a base material. This infers a virtually perfect crystallinity as well as smooth surfaces and interfaces despite the limited availability of suitable substrate materials. Here, we systematically introduce pre-growth treatments and c-AlN buffer layers to optimize c-GaN epitaxial layers. Optimized growth parameters yield extremely small surface roughness values below 1 nm root mean square of phase pure c-GaN layers with very limited stacking fault densities as highlighted by scanning transmission electron microscopy. The crystallinity is monitored by X-ray diffraction and surpasses the current standards. We study the effects of the pre-growth procedures on the optical response by photoluminescence spectroscopy and reconfirm the high structural quality of the epitaxial layers. The combined optimization of all layer properties through the universally applicable approach allows for the growth of more complex quantum structures toward device applications.



INTRODUCTION

The increasing performance demands for next-generation electronics foster materials development beyond the well-established silicon-based technology. Wide-bandgap semiconductor materials such as SiC or GaN are prime candidates for this. They promise efficient handling of the high power densities,^{1,2} which are required for unlocking the full potential of renewable and sustainable energy sources. Furthermore, nitrides allow for high switching speeds required by 6G communications and beyond.³ In optoelectronics, GaN is the prototypical representative of the hexagonal wurtzite group-III-nitrides and its alloys, which cover a vast range of emission wavelengths.⁴ Such devices are commonly grown along the *c*-axis. However, the spontaneous piezoelectric polarization fields perpendicular to the surface decrease the overlap of electron and hole wavefunctions and, thus, typically, the device efficiencies. This challenge is even enhanced in $\text{In}_x\text{Ga}_{1-x}\text{N}$ -based devices. The “green gap” refers to their reduced efficiency in green-wavelength LEDs.⁵ The zincblende phase of group-III-nitrides possesses no internal piezoelectric fields due to the inherent cubic crystal symmetry^{6–9} and is predicted to be beneficial for optoelectronic applications.

The metastability of cubic III-nitrides results in a small growth window. Furthermore, the availability of suitable substrates for heteroepitaxial growth that feature both low lattice mismatch and satisfying crystal quality is limited. 3C-SiC (001)/Si pseudo-substrates are the most common choice for c-GaN epitaxy as free-standing 3C-SiC substrates are

currently not commercially available and the lattice mismatch of alternate high-quality cubic substrates such as GaAs^{10–12} or MgO¹³ is significantly higher. Regardless, the residual lattice mismatch of 3.4%^{14,15} between c-GaN and 3C-SiC causes the formation of misfit dislocations at the interface. Their reduction enhances the crystal quality of heteroepitaxial c-GaN. Therefore, the substrate-epilayer interface needs optimization because defects such as dislocations and stacking faults (SFs) originate here and spread through the bulk layer.¹⁶

One route to circumvent these issues is the introduction of a thin c-AlN buffer layer between the 3C-SiC substrate and the c-GaN epilayer. Conceptually, the c-AlN buffer spatially separates the lattice mismatch and change of ionicity between the substrate and the c-GaN layers: the cubic AlN is virtually lattice matched to the 3C-SiC with a residual lattice mismatch of only 0.3%.^{14,17} At the same time, its ionicity is very similar to that of c-GaN.¹⁸ As a result, each interface of the buffer layer represents a transition of a single lattice property only and allows for individual optimization thereof. The virtues of such AlN as a buffer layer are barely explored for the epitaxy of cubic GaN, even though the growth of cubic AlN on 3C-SiC

Received: August 15, 2022

Revised: September 23, 2022

Published: October 6, 2022



has already been established.^{17,19–22} Few works report the sporadic use of AlN as a buffer^{23–27} or as an interlayer²⁸ yet without explicitly investigating neither the AlN layer itself nor its impact on a subsequent GaN layer. Only very recently, a systematic study of cubic $\text{Al}_x\text{Ga}_{(1-x)}\text{N}$ nucleation layers for the growth of c-GaN by metalorganic vapor-phase epitaxy (MOVPE) was reported and may be indicative of an increasing interest on the impact of the buffer layer.²⁹

This work systematically explores the potential of such interfaces and, consequently, growth optimization and presents smooth, plasma-assisted molecular beam epitaxy (MBE)-grown c-AlN buffer layers for the epitaxy of c-GaN on 3C-SiC/Si pseudo-substrates. The special focus lies on unraveling the influence of the pre-growth substrate preparation and the buffer layer on the layer quality of c-GaN. Thorough characterization reveals that the c-AlN buffer significantly improves the defect density, surface roughness, and phase purity of the c-GaN layer.

■ EXPERIMENTAL SECTION

Cubic GaN epilayers with a thickness of ca. 600 nm were grown on an 8 nm thin c-AlN buffer layer at 720 °C by plasma-assisted MBE on commercially available 10 μm thick 3C-SiC pseudo-substrates deposited on Si(100) by MOVPE (NovaSiC). The growth rate of c-GaN is approximately 400 nm/h. The MBE chamber (Riber Compact12) was equipped with standard effusion cells yielding constant beam equivalent pressures (BEP) of ca. 4.5×10^{-7} and 1.3×10^{-7} mbar for gallium and aluminum, respectively. An Oxford Applied Research HD25 radio frequency plasma source provided activated nitrogen atoms. In-situ reflection high energy electron diffraction (RHEED) monitored the growth to ensure slightly metal-rich growth conditions³⁰ for both c-AlN and c-GaN. Growing AlN under nitrogen-rich conditions or increasing the thickness of the AlN layer leads to 3D growth with the diminishing improvement of the GaN layer. The substrates were heated to $T_{\text{sub}} = 850$ °C after a standard degreasing procedure. The aluminum shutter (BEP(Al) = 1.5×10^{-8} mbar) was repeatedly opened five times for 10 s in order to deoxidize the surface. This “Al flash” procedure has been introduced using Ga^{31–33} and later adopted for the growth of c-AlN.¹⁷

Two sets of c-GaN reference samples were grown without an AlN buffer layer. These allow disentangling the impact of the Al flash and of the AlN buffer layer on the properties of the GaN epilayer. The first reference was grown without the Al flash, whereas the second GaN reference was grown after flashing with aluminum.

High-resolution X-ray diffraction (HRXRD) using a Panalytical X’Pert Pro MRD diffractometer provides structural insights. The layer thickness was estimated from cross-sectional images obtained with a JEOL JSM-7001F scanning electron microscope.

The surface morphologies were investigated by atomic force microscopy (AFM) with a Bruker Multimode 8 in ScanAsyst Air mode using Bruker SCANASYST-AIR probes. The root-mean-square (RMS) roughness was extracted from $6 \times 6 \mu\text{m}^2$ scans using the Gwyddion software.

The photoluminescence (PL) was measured using a custom setup featuring a closed-cycle He cold-finger cryostat with the samples at 20 K in a vacuum. A HeCd laser (325 nm, 0.18 mW excitation power) provided sample excitation. The PL signal was focused by an achromatic lens on the entrance slit of a 25 cm Cerny Tuner spectrograph where it was spectrally dispersed and detected by a thermoelectrically cooled open electrode Si charge-coupled device camera. All spectra were corrected for background signal and the spectral response of the experimental setup.

A standard transmission electron microscopy (TEM) lamella preparation procedure³⁴ has been used by means of the focused ion beam (FIB) JIB-4601F, whereafter deposition of the protection layer (with carbon and tungsten) and lifting out of the protected area, the sample was thinned down to the thickness of 300 nm with 30 kV

energy Ga-ion beam. In order to reduce the damage caused by Ga ions, low-energy ion beams (15, 10, and 5 kV) with low currents (300–30 pA) have been used for fine thinning as well as polishing. This leads to a few tens of nm thick TEM lamella.

Scanning transmission electron microscopy (STEM) investigations have been performed using a double-aberrations-corrected JEOL JEM-2200FS microscope operated at 200 kV. Using the annular dark-field (ADF) detector, two imaging modes were applied. First, the high angle ADF (HAADF) mode has been used to obtain high-resolution images of the structure of the material interfaces. Second, the low angle ADF (LAADF) imaging mode has been chosen in order to visualize the defects in the samples. Energy-dispersive X-ray spectroscopy (EDX) inside the microscope has been used to generate composition maps.

■ RESULTS AND DISCUSSION

RHEED offers in-situ monitoring of the surface during all stages of the growth process. The initial steps of the growth procedure leading to a smooth c-AlN buffer layer are displayed in Figure 1. The RHEED pattern following the degassing step

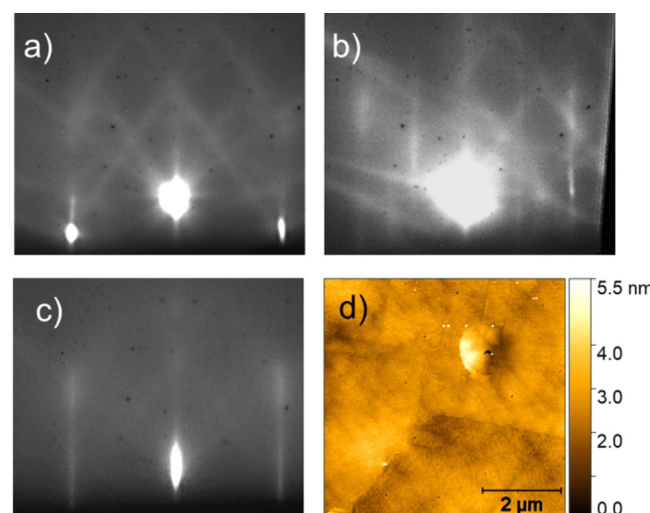


Figure 1. RHEED images of the 3C-SiC surface before (a) and after (b) the Al flash revealing the emerging 2×4 reconstruction. (c) Streaky 1×1 RHEED pattern after the growth of the AlN buffer indicating 2D growth. (d) $6 \times 6 \mu\text{m}$ AFM scan of a c-AlN reference sample preserving the substrate’s surface.

is spotty with a 1×1 reconstruction (Figure 1a). The Al flash changes the surface reconstruction such that the spotty 1×1 pattern transitions to a streaky 2×4 pattern^{35–37} (Figure 1b). This indicates a successful removal of residual oxides and an improvement of the surface roughness. The streaky 1×1 pattern after the growth of an optimized 8 nm c-AlN buffer layer (Figure 1c) indicates a smooth surface and a 2D growth regime. Notably, more metal-rich or nitrogen-rich growth conditions result in higher surface roughness of the AlN buffer layer. The RHEED pattern observed during the growth of c-GaN is similar to that of c-AlN, validating the choice of growth parameters.

Ex-situ analysis verifies the 2D growth of c-AlN. AFM of the surface of a c-AlN reference sample shows that the surface is smooth across an area of $6 \times 6 \mu\text{m}^2$ with an RMS roughness of 0.45 nm (Figure 1d). There is no change in surface roughness compared to the bare substrate, which strongly suggests conformal 2D growth. This is corroborated by the boundary between two anti-phase domains of the 3C-SiC/Si pseudo-

substrate³⁸ observed in the bottom half of the image, which suggests that the surface morphology of the AlN layer is limited by the substrate.

Complementary STEM imaging of a cross-section of a c-AlN buffer between c-GaN and 3C-SiC reveals the impact of the AlN buffer on the formation and distribution of defects in the subsequently grown c-GaN layers. Figure 2a shows an LAADF-

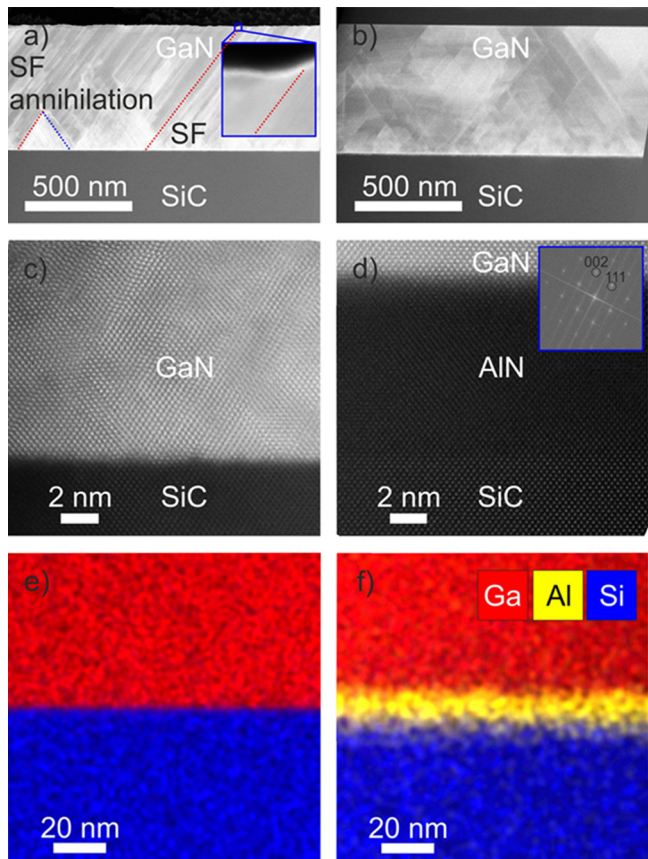


Figure 2. Defect-sensitive LAADF STEM measurements of the GaN layer on 3C-SiC without and with a c-AlN buffer layer are shown in (a) and (b), respectively. The inset in (a) highlights the formation of facets due to SFs penetrating the surface. High-resolution HAADF images of the same samples are shown in (c) and (d). FFT analysis [inset of (d)] confirms the zincblende crystal structure. The corresponding EDX elemental maps in (e) and (f) reveal a homogeneous chemical composition of all layers.

STEM image of a c-GaN layer grown without Al flash or AlN buffer on 3C-SiC. Figure 2b displays a c-GaN layer grown using an AlN buffer. The LAADF imaging method is well suited to detect defects such as SFs. These are the dominant planar defects. They are observed as bright lines propagating through the entire GaN layer.^{16,39} Two SFs with different inclinations can annihilate when they intersect. This then results in the decrease of the overall defect density.²⁷ This annihilation occurs particularly often during the first 200 nm of the GaN layer (Figure 2a). Note that more SFs are observable in the Ga-polar [110] viewing direction compared to the perpendicular N-polar [110] direction, which is in accordance with the previous finding in GaP.⁴⁰ Additionally, in the Ga-polar [110] direction more SFs are found on one type of {111} planes (marked in red in Figure 2a) than on the other ones (marked in blue) in the sample without AlN buffer. This infers

only a few annihilation opportunities³⁹ and, consequently, a high defect density throughout the whole GaN layer. The inset in Figure 2a demonstrates how SFs lead to the formation of facets on the surface, which increases the roughness. This is also observable in the AFM measurements. On the other hand, the GaN layer grown with an AlN buffer layer (Figure 2b) features a symmetric distribution of SFs, a lower defect density, and a smooth surface.

Moreover, Figure 2c provides atomically resolved insight into the interfaces between the substrate and the c-GaN layer. HR-STEM (Figure 2d) clearly resolves the smooth interface of c-AlN and 3C-SiC. The low lattice mismatch fosters extremely little defect formation at the interface. The inset in Figure 2d shows the corresponding FFT, which highlights the zincblende crystal structure of the sample.

Additional EDX analysis (Figure 2f) of the c-AlN buffer layer between the substrate and the c-GaN layer confirms a homogeneous chemical composition of the AlN layer with no significant intermixing with GaN or SiC on the nanometer scale.

We assess the impact of the Al flash and the AlN buffer layer on the quality of c-GaN epilayers by XRD and AFM. Figure 3a shows several key quality parameters for the three different sample designs, which are as follows: (I) c-GaN directly grown on 3C-SiC without Al flash and AlN buffer, (II) c-GaN grown on 3C-SiC after performing an Al flash (without AlN buffer), and (III) c-GaN grown on a c-AlN buffer layer that was grown on 3C-SiC after an Al flash. The AlN buffer simultaneously improves all key performance parameters of the c-GaN layer as it renders narrow XRD linewidth, small RMS roughness, and phase-pure material, that is, extremely low number of SFs which, sometimes, are considered as hexagonal inclusions.

The ω -full width at half maximum (FWHM) of the (002) GaN reflection is related to the threading dislocation density and the grain size and should be minimal for reliable device engineering. The optimized c-GaN layers with a thickness of about 600 nm show a $\Delta\omega = 20.0$ arcmin. These samples underwent a pre-growth Al flash procedure and include an optimized AlN buffer layer. This is nearly half the width of the reference sample on untreated 3C-SiC, which shows a $\Delta\omega = 34.8$ arcmin. These values infer a dislocation density in the order of 10^9 cm^{-2} .⁴¹⁻⁴³

The RMS roughness is another characteristic layer property that needs to be minimized for the fabrication of multi-layered heterostructures. Optimized samples including Al flash and smooth c-AlN buffer feature an RMS roughness of 0.75 nm. This is about one order of magnitude lower than other reported roughness values of c-GaN layers on 3C-SiC, which typically vary between 4 and 10 nm.^{44,45} Notably, already the slightly Ga-rich growth conditions yield a smooth surface with a roughness of about 2.6 nm even without flashing or a buffer layer.

Furthermore, the phase purity of the cubic phase is estimated by the intensity ratio of the hexagonal (10–11) reflection and the cubic (002) reflection from the reciprocal space maps taking into account the structure factors of each reflection. In the case of GaN directly grown on untreated 3C-SiC, about 16.6% hexagonal inclusions nucleate on (111) facets of the cubic layer. This is significantly reduced to 8.8% when adding an Al flashing step to the growth procedure. The combination of Al flash and AlN buffer layer renders phase pure zincblende GaN. The residual ratio of hexagonal inclusions in cubic GaN is now estimated to be less than 0.3%.

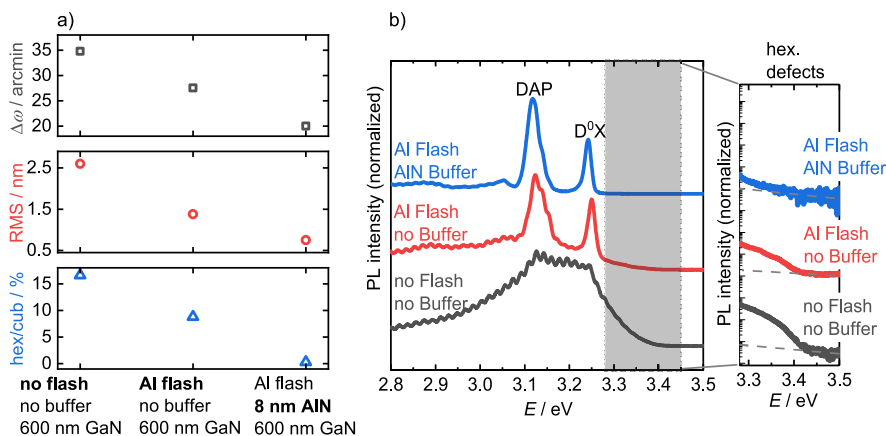


Figure 3. (a,b) impact of the Al flash and of the c-AlN buffer on the properties of the 600 nm thick c-GaN layer. (a) ω -FWHM of the (002) reflection, RMS roughness, and intensity ratio of the hexagonal (10–11) reflection to the cubic (002) reflection. (b) cw-PL spectra at 20 K with a magnification of the high energy shoulder.

PL spectra showcase the impact of Al flash and AlN buffer on the optical properties (Figure 3b). GaN grown directly on untreated 3C-SiC exhibits one broad emission peak centered at 3.18 eV. The intensity modulation of the signal at low energies is caused by substrate interference. The Al flash and the AlN buffer yield two narrow PL peaks at 3.12 eV and 3.24 eV, respectively. These correspond to the donor–acceptor pair recombination (DAP) and neutral donor-bound exciton recombination (D^0X), respectively.²⁸ The FWHM of the D^0X peak of the GaN layer with AlN buffer at 20 K is 16 meV. The inset of Figure 3b shows the high-energy shoulder in a semi-logarithmic plot to elucidate the contributions of hexagonal defects. The emission of hexagonal defects is minimized due to the AlN buffer corroborating the low ratio of hexagonal inclusions presented in Figure 3a.

Conceptually, the c-AlN buffer spatially separates the lattice mismatch and change of ionicity between the substrate and the c-GaN layers: the cubic AlN is virtually lattice matched to the 3C-SiC with a residual lattice mismatch of only 0.3%.^{14,17} At the same time, its ionicity is very similar to that of c-GaN.¹⁸ As a result, each interface of the buffer layer represents a transition of a single lattice property only and allows for individual optimization thereof.

The FWHM of ω -scans is suitable data to compare the quality of the epitaxial layers in this work to literature data on other cubic GaN layers grown on comparable 3C-SiC/Si substrates. These values directly reflect the density of structural defects.^{41–43} Furthermore, they are extremely robust as they are reproducibly measured and commonly reported in most publications featuring epitaxial growth. However, it is important to consider the layer thickness d when comparing $\Delta\omega$ of thin films as $\Delta\omega$ decreases with increasing layer thickness.^{27,46,47} This is depicted in Figure 4, by dark gray symbols representing the samples of this work. The thickest film shows the narrowest $\Delta\omega$. In general, this phenomenon is associated with coalescence of threading dislocations, which is theoretically described by the glide model of Ayers.⁴⁸ This trend is empirically approximated by $\Delta\omega(d) \propto d^{-1/3}$ ⁴⁷ corresponding to the dashed blue line in Figure 4.

The set of 600 nm thick c-GaN layers grown on 3C-SiC/Si with Al flash but no AlN buffer (green, crossed square) compares well with state-of-the-art c-GaN on 3C-SiC/Si substrates grown by MOVPE (green squares) and MBE (blue circles). Moreover, the addition of the AlN buffer yields

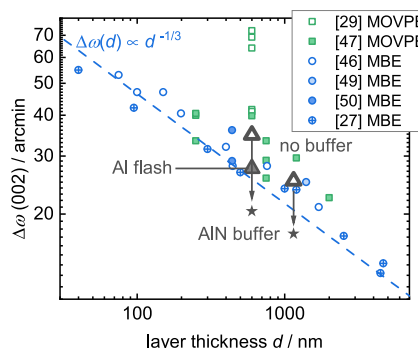


Figure 4. Decreasing XRD- $\Delta\omega$ of GaN layers with increasing layer thicknesses. The samples of this work are represented by dark gray symbols, while green squares and blue circles refer to other c-GaN layers grown by MOVPE^{29,47} and MBE^{27,46,49,50} on comparable 3C-SiC substrates, respectively.

an additionally reduced $\Delta\omega$ (stars) significantly below the literature values. Thus, the c-AlN buffer provides excellent layer quality of c-GaN on comparable substrates. Figure 4 also presents the $\Delta\omega$ of c-GaN layers with a thickness of 1150 nm, which is reduced from 25.3 to 17.4 arcmin due to the AlN buffer.

CONCLUSIONS

Pre-growth Al flash treatment and a thin c-AlN buffer between the substrate and epilayer enhance the epitaxial growth of c-GaN on 3C-SiC. This improves virtually all layer quality parameters. Thorough characterization with XRD, AFM, STEM, and PL reveals a significant reduction of the defect density, surface roughness, and SFs, which are sometimes referred to as hexagonal inclusions of the c-GaN layers. Exemplary 600 nm-thick c-GaN layers regularly show $\Delta\omega$ of 20.0 arcmin and a RMS roughness of 0.75 nm on 3C-SiC/Si substrates. The simultaneous improvement of all relevant quality parameters without any inherent drawback highlights the progress by a c-AlN buffer layer for the advancement of cubic GaN. Our observations infer that the spatial separation of the lattice mismatch and change of ionicity are instrumental for the enhanced materials properties of the GaN layer and, thus, inherently for any successive growth or fabrication and device properties. In particular, the low roughness enables the

use of c-GaN as templates for the growth of more complex heterostructures, for example, (In,Al)GaN.

■ AUTHOR INFORMATION

Corresponding Author

Sangam Chatterjee — Institute of Experimental Physics I and Center for Materials Research, Justus Liebig University Giessen, 35392 Giessen, Germany;  orcid.org/0000-0002-0237-5880; Email: Sangam.Chatterjee@exp1.physik.uni-giessen.de

Authors

Mario F. Zscherp — Institute of Experimental Physics I and Center for Materials Research, Justus Liebig University Giessen, 35392 Giessen, Germany;  orcid.org/0000-0003-3515-5232

Nils Mengel — Institute of Experimental Physics I and Center for Materials Research, Justus Liebig University Giessen, 35392 Giessen, Germany

Detlev M. Hofmann — Institute of Experimental Physics I and Center for Materials Research, Justus Liebig University Giessen, 35392 Giessen, Germany

Vitalii Lider — Materials Science Center and Faculty of Physics, Philipps-University Marburg, 35032 Marburg, Germany;  orcid.org/0000-0003-4493-9370

Badrosadat Ojaghi Dogahe — Materials Science Center and Faculty of Physics, Philipps-University Marburg, 35032 Marburg, Germany

Celina Becker — Materials Science Center and Faculty of Physics, Philipps-University Marburg, 35032 Marburg, Germany

Andreas Beyer — Materials Science Center and Faculty of Physics, Philipps-University Marburg, 35032 Marburg, Germany;  orcid.org/0000-0001-6533-0631

Kerstin Volz — Materials Science Center and Faculty of Physics, Philipps-University Marburg, 35032 Marburg, Germany

Jörg Schörmann — Institute of Experimental Physics I and Center for Materials Research, Justus Liebig University Giessen, 35392 Giessen, Germany;  orcid.org/0000-0001-7244-2201

Complete contact information is available at:

<https://pubs.acs.org/10.1021/acs.cgd.2c00927>

Notes

The authors declare no competing financial interest.

■ ACKNOWLEDGMENTS

The funding was provided by the Deutsche Forschungsgemeinschaft (DFG, German Research Foundation), Project-ID 223848855-SFB 1083 and the European regional development fund through the Innovation Laboratory High-Performance Materials.

■ REFERENCES

- (1) Casady, J. B.; Johnson, R. W. Status of silicon carbide (SiC) as a wide-bandgap semiconductor for high-temperature applications: a review. *Solid-State Electron.* **1996**, *39*, 1409–1422.
- (2) Morkoç, H.; et al. Large-band-gap SiC, III-V nitride, and II-VI ZnSe-based semiconductor device technologies. *J. Appl. Phys.* **1994**, *76*, 1363–1398.
- (3) Jia, W.; Sensale-Rodriguez, B. Terahertz metamaterial modulators based on wide-bandgap semiconductor lateral Schottky diodes. *Opt. Mater. Express* **2022**, *12*, 940–948.
- (4) Ambacher, O. Growth and applications of Group III-nitrides. *J. Phys. D: Appl. Phys.* **1998**, *31*, 2653–2710.
- (5) Humphreys, C. J.; et al. The atomic structure of polar and non-polar InGaN quantum wells and the green gap problem. *Ultramicroscopy* **2017**, *176*, 93–98.
- (6) As, D. J. Cubic group-III nitride-based nanostructures—basics and applications in optoelectronics. *Microelectron. J.* **2009**, *40*, 204–209.
- (7) Abe, M.; et al. Cubic GaN/AlGaN HEMTs on 3C-SiC Substrate for Normally-O ff. *IEICE Trans:Electron.* **2006**, *E89-C*, 1057–1063.
- (8) Li, S.; Schörmann, J.; As, D. J.; Lischka, K. Room temperature green light emission from nonpolar cubic InGaN/GaN multi-quantum-wells. *Appl. Phys. Lett.* **2007**, *90*, No. 071903.
- (9) Schörmann, J.; Potthast, S.; As, D. J.; Lischka, K. Near ultraviolet emission from nonpolar cubic Al_xGa_{1-x}N/GaN quantum wells. *Appl. Phys. Lett.* **2006**, *89*, 131910.
- (10) Strite, S.; et al. An investigation of the properties of cubic GaN grown on GaAs by plasma-assisted molecular-beam epitaxy. *J. Vac. Sci. Technol., B: Microelectron. Nanometer Struct.-Process., Meas., Phenom.* **1991**, *9*, 1924.
- (11) Okumura, H.; Misawa, S.; Yoshida, S. Epitaxial growth of cubic and hexagonal GaN on GaAs by gas-source molecular-beam epitaxy. *Appl. Phys. Lett.* **1991**, *59*, 1058–1060.
- (12) Yang, H.; Brandt, O.; Ploog, K. MBE growth of cubic GaN on GaAs substrates. *Phys. Status Solidi B* **1996**, *194*, 109–120.
- (13) Powell, R. C.; Lee, N. E.; Kim, Y. W.; Greene, J. E. Heteroepitaxial wurtzite and zinc-blende structure GaN grown by reactive-ion molecular-beam epitaxy: Growth kinetics, microstructure, and properties. *J. Appl. Phys.* **1993**, *73*, 189–204.
- (14) Yakimova, R.; Vasiliauskas, R.; Eriksson, J.; Syväjärvi, M. Progress in 3C-SiC growth and novel applications. *Mater. Sci. Forum* **2012**, *711*, 3–10.
- (15) Novikov, S. V.; et al. Molecular beam epitaxy as a method for the growth of freestanding zinc-blende (cubic) GaN layers and substrates. *J. Vac. Sci. Technol., B: Nanotechnol. Microelectron.: Mater., Process., Meas., Phenom.* **2010**, *28*, C3B1–C3B6.
- (16) Vacek, P.; et al. Defect structures in (001) zincblende GaN/3C-SiC nucleation layers. *J. Appl. Phys.* **2021**, *129*, 155306.
- (17) Schupp, T.; Lischka, K.; As, D. J. MBE growth of atomically smooth non-polar cubic AlN. *J. Cryst. Growth* **2010**, *312*, 1500–1504.
- (18) Haynes, W. M., Lide, D. R., Bruno, T. J. CRC Handbook of Chemistry and Physics 97th edition. CRC Taylor & Francis Group.
- (19) Okumura, H.; et al. Growth of cubic III-nitrides by gas source MBE using atomic nitrogen plasma: GaN, AlGaN and AlN. *J. Cryst. Growth* **1998**, *189–190*, 390–394.
- (20) Koizumi, T.; et al. Growth and characterization of cubic AlGaN and AlN epilayers by RF-plasma assisted MBE. *J. Cryst. Growth* **1999**, *201–202*, 341–345.
- (21) Martinez-Guerrero, E.; et al. Growth control of cubic GaN and GaAlN (GaInN) Alloys by RHEED oscillations. *Phys. Status Solidi A* **1999**, *176*, 497–501.
- (22) Jonnard, P.; et al. Electronic structure of wurtzite and zinc-blende AlN. *Eur. Phys. J. B* **2004**, *42*, 351–359.
- (23) Gerthsen, D.; et al. Molecular beam epitaxy (MBE) growth and structural properties of GaN and AlN on 3C-SiC(001) substrates. *J. Cryst. Growth* **1999**, *200*, 353–361.
- (24) Goldys, E. M.; Godlewski, M.; Langer, R.; Barski, A. Surface morphology of cubic and wurtzite GaN films. *Appl. Surf. Sci.* **2000**, *153*, 143–149.
- (25) Martinez-Guerrero, E.; et al. Modified Stranski-Krastanov Growth in Stacked Layers of Self-Assembled Cubic GaN/AlN Quantum Dots. *Phys. Status Solidi A* **2001**, *188*, 711–714.
- (26) Martinez-Guerrero, E.; Chabuel, F.; Daudin, B.; Rouvière, J. L.; Mariette, H. Control of the morphology transition for the growth of cubic GaN/AlN nanostructures. *Appl. Phys. Lett.* **2002**, *81*, 5117–5119.

- (27) Martinez-Guerrero, E.; et al. Structural properties of undoped and doped cubic GaN grown on SiC(001). *J. Appl. Phys.* **2002**, *91*, 4983–4987.
- (28) Church, S. A.; et al. Photoluminescence studies of cubic GaN epilayers. *Phys. Status Solidi B* **2017**, *254*, No. 1600733.
- (29) Gundimeda, A.; et al. Influence of Al_xGa_{1-x}N nucleation layers on MOVPE-grown zincblende GaN epilayers on 3C-SiC/Si(001). *J. Phys. D: Appl. Phys.* **2022**, *55*, 175110.
- (30) Schörmann, J.; Potthast, S.; As, D. J.; Lischka, K. In situ growth regime characterization of cubic GaN using reflection high energy electron diffraction. *Appl. Phys. Lett.* **2007**, *90*, No. 041918.
- (31) Wright, S.; Kroemer, H. Reduction of oxides on silicon by heating in a gallium molecular beam at 800°C. *Appl. Phys. Lett.* **1980**, *36*, 210–211.
- (32) Kaplan, R.; Parrill, T. M. Reduction of SiC surface oxides by a Ga molecular beam: LEED and electron spectroscopy studies. *Surf. Sci.* **1986**, *165*, L45–L52.
- (33) Brown, A. S.; et al. The impact of SiC substrate treatment on the heteroepitaxial growth of GaN by plasma assisted MBE. *Cryst. Res. Technol.* **2005**, *40*, 997–1002.
- (34) Schaffer, M.; Schaffer, B.; Ramasse, Q. Sample preparation for atomic-resolution STEM at low voltages by FIB. *Ultramicroscopy* **2012**, *114*, 62–71.
- (35) Soukiassian, P. Atomic control of Si-terminated cubic silicon carbide (100) surfaces: Morphology and self-organized atomic lines. *Mater. Sci. Eng., B* **1999**, *61–62*, 506–515.
- (36) Bustarret, E.; et al. Interracial strain in 3C-SiC/Si(100) pseudo-substrates for cubic nitride epitaxy. *Phys. Status Solidi A* **2003**, *195*, 18–25.
- (37) Schupp, T.; et al. MBE growth of cubic AlN on 3C-SiC substrate. *Phys. Status Solidi A* **2010**, *207*, 1365–1368.
- (38) Kemper, R. M.; et al. Anti-phase domains in cubic GaN. *J. Appl. Phys.* **2011**, *110*, 123512.
- (39) Lee, L. Y.; et al. Investigation of stacking faults in MOVPE-grown zincblende GaN by XRD and TEM. *J. Appl. Phys.* **2019**, *125*, 105303.
- (40) Beyer, A.; et al. Influence of crystal polarity on crystal defects in GaP grown on exact Si (001). *J. Appl. Phys.* **2011**, *109*, No. 083529.
- (41) Gay, P.; Hirsch, P. B.; Kelly, A. The estimation of dislocation densities in metals from X-ray data. *Acta Metall.* **1953**, *1*, 315–319.
- (42) Dunn, C. G.; Koch, E. F. Comparison of dislocation densities of primary and secondary recrystallization grains of Si-Fe. *Acta Metall.* **1957**, *5*, 548–554.
- (43) Metzger, T.; et al. Defect structure of epitaxial GaN films determined by transmission electron microscopy and triple-axis X-ray diffractometry. *Philos. Mag. A* **1998**, *77*, 1013–1025.
- (44) Lee, L. Y.; et al. Effect of growth temperature and V/III-ratio on the surface morphology of MOVPE-grown cubic zincblende GaN. *J. Appl. Phys.* **2018**, *124*, 105302.
- (45) Meier, F.; et al. Selective area growth of cubic gallium nitride on silicon (001) and 3C-silicon carbide (001). *AIP Adv.* **2021**, *11*, No. 075013.
- (46) Kemper, R. M.; et al. STEM-CL investigations on the influence of stacking faults on the optical emission of cubic GaN epilayers and cubic GaN/AlN multi-quantum wells. *Phys. Status Solidi C* **2015**, *12*, 469–472.
- (47) Frentrup, M.; et al. X-ray diffraction analysis of cubic zincblende III-nitrides. *J. Phys. D: Appl. Phys.* **2017**, *50*, 433002.
- (48) Ayers, J. E. New model for the thickness and mismatch dependencies of threading dislocation densities in mismatched heteroepitaxial layers. *J. Appl. Phys.* **1995**, *78*, 3724–3726.
- (49) Kemper, R. M.; et al. Formation of defects in cubic GaN grown on nano-patterned 3C-SiC (001). *Phys. Status Solidi C* **2012**, *9*, 1028–1031.
- (50) Kemper, R. M.; et al. Growth of cubic GaN on nano-patterned 3C-SiC/Si (0 0 1) substrates. *J. Cryst. Growth* **2011**, *323*, 84–87.

Publication 2

Overcoming the Miscibility Gap of GaN/InN in MBE Growth of Cubic In_xGa_{1-x}N

Zscherp, M. E.; Jentsch, S. A.; Müller, M. J.; Lider, V.; Becker, C.; Chen, L.; Littmann, M.; Meier, F.; Beyer, A.; Hofmann, D. M.; As, D. J.; Klar, P. J.; Volz, K.; Chatterjee, S.; Schörmann, J.

ACS Appl. Mater. Interfaces **2023**, *15* (33), 39513–39522

<https://doi.org/10.1021/acsami.3c06319>

Reprinted with permission. Copyright 2023 American Chemical Society

Overcoming the Miscibility Gap of GaN/InN in MBE Growth of Cubic $\text{In}_x\text{Ga}_{1-x}\text{N}$

Mario Fabian Zscherp, Silas Aurel Jentsch, Marius Johannes Müller, Vitalii Lider, Celina Becker, Limei Chen, Mario Littmann, Falco Meier, Andreas Beyer, Detlev Michael Hofmann, Donat Josef As, Peter Jens Klar, Kerstin Volz, Sangam Chatterjee, and Jörg Schörmann*



Cite This: *ACS Appl. Mater. Interfaces* 2023, 15, 39513–39522



Read Online

ACCESS |

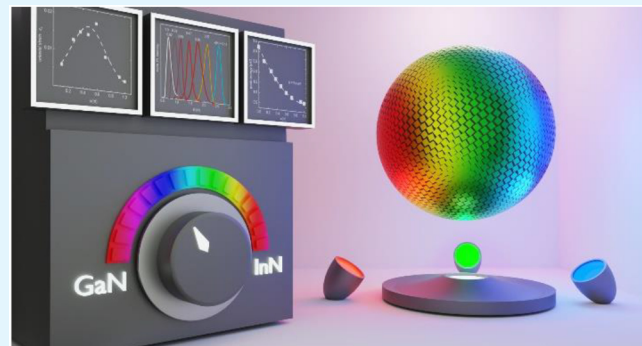
Metrics & More

Article Recommendations

Supporting Information

ABSTRACT: The lack of internal polarization fields in cubic group-III nitrides makes them promising arsenic-free contenders for next-generation high-performance electronic and optoelectronic applications. In particular, cubic $\text{In}_x\text{Ga}_{1-x}\text{N}$ semiconductor alloys promise band gap tuning across and beyond the visible spectrum, from the near-ultraviolet to the near-infrared. However, realization across the complete composition range has been deemed impossible due to a miscibility gap corresponding to the amber spectral range. In this study, we use plasma-assisted molecular beam epitaxy (PAMBE) to fabricate cubic $\text{In}_x\text{Ga}_{1-x}\text{N}$ films on c-GaN/AlN/3C-SiC/Si template substrates that overcome this challenge by careful adjustment of the growth conditions, conclusively closing the miscibility gap. X-ray diffraction reveals the composition, phase purity, and strain properties of the $\text{In}_x\text{Ga}_{1-x}\text{N}$ films. Scanning transmission electron microscopy reveals a CuPt-type ordering on the atomistic scale in highly alloyed films with $x(\text{In}) \approx 0.5$. Layers with much lower and much higher indium content exhibit statistical distributions of the cations Ga and In. Notably, this CuPt-type ordering results in a spectrally narrower emission compared to that of statistically disordered zincblende materials. The emission energies of the films range from 3.24 to 0.69 eV and feature a quadratic bowing parameter of $b = 2.4$ eV. In contrast, the LO-like phonon modes that are observed by Raman spectroscopy exhibit a one-mode behavior and shift linearly from c-GaN to c-InN.

KEYWORDS: molecular beam epitaxy, $\text{In}_x\text{Ga}_{1-x}\text{N}$, strain, miscibility, cubic III-nitrides, TEM, optical properties



INTRODUCTION

Light-emitting semiconductor devices with sufficient quantum efficiencies that are able to operate across the complete visible spectrum and are based on the same epitaxially grown semiconductor alloy system will disruptively change the landscape of optoelectronic applications and devices. They will eliminate the need for phosphors in white light-emitting diodes (LEDs) and potentially yield multiple color lasers or illuminators such as micro-LEDs.¹ Zincblende $\text{In}_x\text{Ga}_{1-x}\text{N}$ is a prime contender for these tasks, as its direct band gap is tunable from the near-ultraviolet^{2,3} toward the near-infrared.^{4–6} Unlike the thermodynamically stable hexagonal wurtzite phase, the cubic crystal structure is free of internal piezoelectric fields,^{7–10} which commonly reduce the radiative recombination of electrons and holes.¹¹ This advantage becomes more important with increasing In content, as a larger In content also increases the piezoelectric fields and greatly reduces the efficiency of green and amber h- $\text{In}_x\text{Ga}_{1-x}\text{N}$ -based LEDs.

However, growing metastable c- $\text{In}_x\text{Ga}_{1-x}\text{N}$ films that have good epitaxial quality is difficult due to largely different lattice

constants,^{4,12} significantly different growth temperatures for the two binary compounds, and a lack of substrates for homoepitaxy. As a result, reports of the phase-pure growth of c- $\text{In}_x\text{Ga}_{1-x}\text{N}$ with more than 30% In content are scarce, and numerous works predict^{13,14} and report^{15–17} spinodal decomposition with the formation of an additional In-rich phase. In most cases, c- $\text{In}_x\text{Ga}_{1-x}\text{N}$ is heteroepitaxially grown on c-GaN. This interface can induce a significant amount of strain in the c- $\text{In}_x\text{Ga}_{1-x}\text{N}$ layers, depending on the indium content and the layer thickness. As a result, the cubic crystal symmetry is distorted tetragonally, and in-plane and out-of-plane lattice constants deviate from each other. Neglecting this distortion usually leads to an overestimation of the indium content by up

Received: May 3, 2023

Accepted: July 21, 2023

Published: August 2, 2023



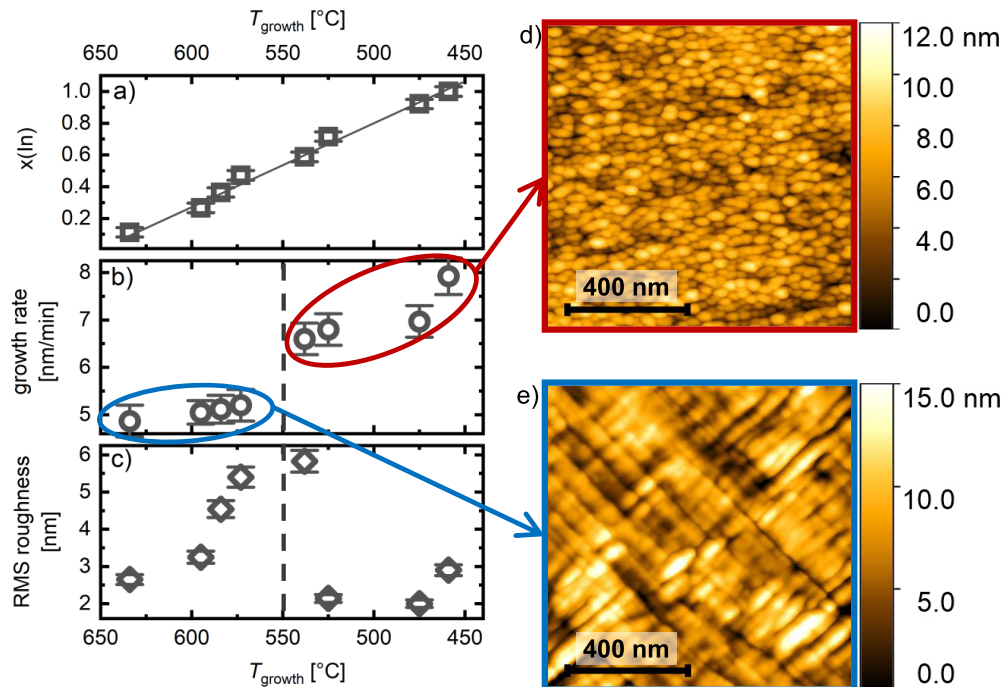


Figure 1. Impact the growth temperature T_{growth} has on the $\text{c-In}_x\text{Ga}_{1-x}\text{N}$ epitaxial layer. As T_{growth} decreases, (a) the indium content increases linearly, (b) the growth rate showcases two distinct regimes, and (c) the roughness increases to a maximum (though it is lowest at low temperatures). Two $1 \times 1 \mu\text{m}^2$ AFM scans show the morphology of (d) the low-temperature regime and (e) the high-temperature regime.

to 20%. Therefore, it is important to consider such strain in order to understand the impact indium content has on the optical properties of $\text{c-In}_x\text{Ga}_{1-x}\text{N}$.

In this work, we report phase-pure cubic $\text{In}_x\text{Ga}_{1-x}\text{N}$ layers with $0 \leq x(\text{In}) \leq 1$ grown on $\text{c-GaN}/\text{AlN}/\text{3C-SiC}/\text{Si}(001)$ templates by plasma-assisted molecular beam epitaxy (PAMBE). We demonstrate the continuous tunability of the indium content by carefully adjusting the growth temperature and the metal fluxes. Furthermore, we emphasize the role of strain in enabling full miscibility of c-GaN and c-InN . Comprehensive characterization of the layers illustrates the impact indium content has on the nanoscopic crystal lattice and on the optical response of the cubic $\text{In}_x\text{Ga}_{1-x}\text{N}$ layers.

EXPERIMENTAL SECTION

Cubic $\text{In}_x\text{Ga}_{1-x}\text{N}$ layers are grown on c-GaN templates at T_{growth} , ranging from 460 to 630 °C, by PAMBE. All epitaxial layers feature a thickness of approximately 80–100 nm. The indium contents $x(\text{In})$ of the various layers grown are 0.11, 0.27, 0.36, 0.47, 0.59, 0.72, 0.92, and 1. The c-GaN templates, with thicknesses of approximately 600 nm, are grown using an 8 nm c-AlN buffer¹⁸ on commercial 3C-SiC/Si(001) pseudo substrates (NovaSiC). The MBE chamber (Riber Compact 12) is equipped with standard effusion cells and an Oxford Applied Research HD25 radio frequency plasma source. The growth surface is monitored by *in situ* reflection high energy electron diffraction (RHEED). For $\text{c-In}_x\text{Ga}_{1-x}\text{N}$ growth, the sensitivity-corrected beam equivalent pressures (BEP) of gallium and indium are varied between 1.4×10^{-8} and 1.1×10^{-7} mbar and between 9.2×10^{-8} and 2.5×10^{-7} mbar, respectively.

High-resolution X-ray diffraction (HRXRD), using a Rigaku SmartLab diffractometer that operates a 9 kW rotating Cu anode, provides the initial structural characterization, including the determination of the indium content. The thickness of the $\text{c-In}_x\text{Ga}_{1-x}\text{N}$ layers is determined from cross-sectional scanning electron microscopy images, obtained with a JEOL JSM-7001F instrument, and confirmed by X-ray reflectivity measurements. A Bruker

Multimode 8 atomic force microscope (AFM), operating in the ScanAsyst Air mode and using Bruker SCANASYST-AIR probes, yields the surface morphology. Gwyddion software is used for image processing and deriving the root-mean-square (RMS) roughness.

Because the optical properties are of particular interest for potential future applications, we studied the low-temperature ($T \approx 20$ K) photoluminescence (PL) of the samples. Three different measurement setups are used to cover the large variation in emission energies, all of which feature a laser diode at 405 nm for excitation. Samples with $x(\text{In}) < 0.5$ are measured using an excitation power of $P_{\text{exc},1} = 6.9$ mW and a thermoelectrically (TE) cooled, ultraviolet-optimized back-illuminated CCD camera. Samples with higher In content ($0.5 < x(\text{In}) < 0.75$) are measured using $P_{\text{exc},2} = 22$ mW and a 1.7 μm TE-cooled InGaAs array detector. For samples with $x(\text{In}) > 0.75$, a 2.2 μm TE-cooled InGaAs array detector is used with $P_{\text{exc},3} = 23$ mW.

The scanning transmission electron microscopy (STEM) investigations in the present study employ a double-aberrations-corrected JEOL JEM-2200FS microscope, operating at 200 kV with an annular dark-field (ADF) detector. Two imaging modes are used, namely the high-angle ADF (HAADF) and the low-angle ADF (LAADF) imaging modes. The former mode is utilized to obtain high-resolution images of the material's structure, while the latter mode is used to visualize the defects in the sample. Energy-dispersive X-ray spectroscopy (EDX) is used to generate composition maps and determine the local In concentration.

Raman spectra are recorded at room temperature using a Renishaw inVia Raman spectrometer combined with a Leica optical microscope in a backscattering geometry. A 405 nm line from a C-FLEX laser combiner (HÜBNER Photonics) is used as the excitation source. The laser power is typically a few milliwatts. A 50X objective is used to focus the laser light onto the sample and collect the scattered light. The collected light is dispersed by a 1800 lines per millimeter diffraction grating in the spectrometer and is then focused onto a charge-coupled device (CCD) detector.

RESULTS AND DISCUSSION

The III/III and III/V ratios are adjusted carefully in order to grow $\text{c-In}_x\text{Ga}_{1-x}\text{N}$ across the whole composition range. In

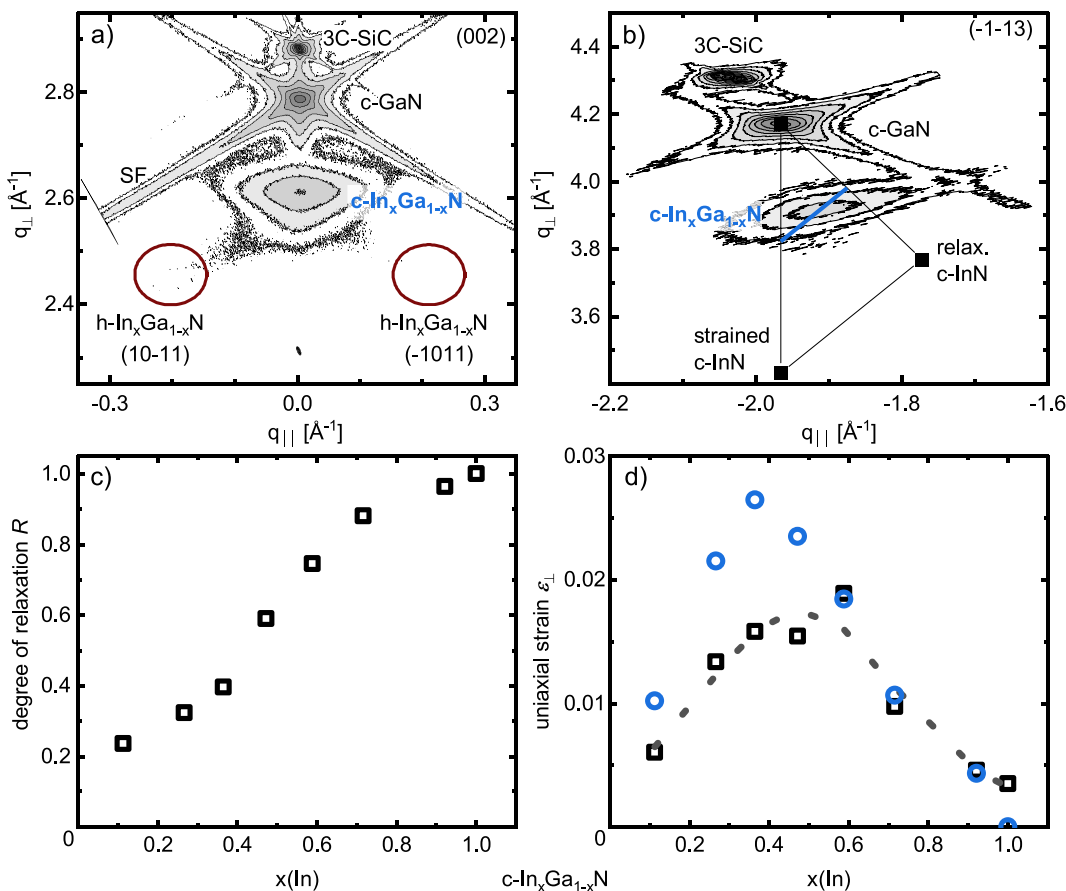


Figure 2. Selected reciprocal space maps of a sample with $x(\text{In}) = 0.47$, centered at (a) the symmetric (002) reflection and (b) the asymmetric ($-1-13$) reflection of c-GaN. The space maps reveal a pure cubic phase and a single, but strained, c-In_xGa_{1-x}N phase. (c) The degree of relaxation continuously increases with $x(\text{In})$, whereas (d) the uniaxial strain is highest for intermediate indium content (the dashed line serves as a guide for the eye). Black squares represent the strain calculated using the $2\theta-\omega$ scans, and the blue circles denote the strain derived from the degree of relaxation of the binary compounds.

general, metal-rich growth conditions lead to smooth surfaces and phase-pure cubic epitaxial layers,^{18,19} whereas the In/Ga ratio is vital for tuning the alloy's composition. However, the growth temperature T_{growth} governs the maximum In content of the thin film due to the low binding energy of In–N. The impact of T_{growth} on the growth rate, the morphology, and the surface roughness of the c-In_xGa_{1-x}N layers is detailed in Figure 1.

Figure 1a shows that the In content $x(\text{In})$ increases linearly as the growth temperature decreases. Next, we observe two distinct growth regimes, where a sharp increase in the growth rate from 5.2 to 6.6 nm/min occurs at $T_{\text{growth}} \cong 550^\circ\text{C}$ (Figure 1b). Correspondingly, AFM imaging reveals two different surface morphologies that are dependent on the growth temperature. For low temperatures ($T_{\text{growth}} < 550^\circ\text{C}$), we observe small, round crystallites ($d_{\text{cryst}} \approx 50 \text{ nm}$, Figure 1d). In contrast, for high temperatures ($T_{\text{growth}} > 550^\circ\text{C}$), the c-In_xGa_{1-x}N surface exhibits elongated crystallites (Figure 1e). Additionally, the RMS roughness increases with decreasing temperature, reaching a maximum value of 5.8 nm at $T_{\text{growth}} = 538^\circ\text{C}$ (Figure 1c). However, the height of the round crystallites decreases rapidly for even lower temperatures and high In content, yielding smooth surfaces with an RMS roughness of approximately 2 nm.

The differences in morphology are in concordance with in situ RHEED observations (Figure S1) at the initial c-In_xGa_{1-x}N growth. In the high-temperature regime, the streaky pattern of c-GaN is retained for several minutes. For lower growth temperatures, the RHEED pattern immediately shifts to oval-shaped reflections with the start of c-In_xGa_{1-x}N growth. This indicates different nucleation processes of c-In_xGa_{1-x}N on c-GaN for these two cases. Overall, these results highlight the crucial role growth temperature plays on the indium content, growth rate, and morphology.

Mapping the reciprocal space of both the symmetric (002) and asymmetric ($-1-13$) reflections by using HRXRD is essential for investigating and validating the crystal structure of the c-In_xGa_{1-x}N alloys. In particular, any hexagonal inclusions are important to quantify, as they can nucleate on cubic (111) facets. Figure 2a shows an exemplary reciprocal space map centered at the (002) reflection of c-GaN. The red circles mark the expected position of the (10-11) and (-1011) reflections of hexagonal In_xGa_{1-x}N. The intensity ratio of the hexagonal {10-11} reflection and the cubic (002) reflection is an indication of the proportion of hexagonal inclusions. This ratio is below 2% for all of the ternary c-In_xGa_{1-x}N samples in this study, which confirms the purity of the cubic zincblende phase. Furthermore, we do not observe any secondary c-In_xGa_{1-x}N reflections on the (002) or ($-1-13$) space maps, which would

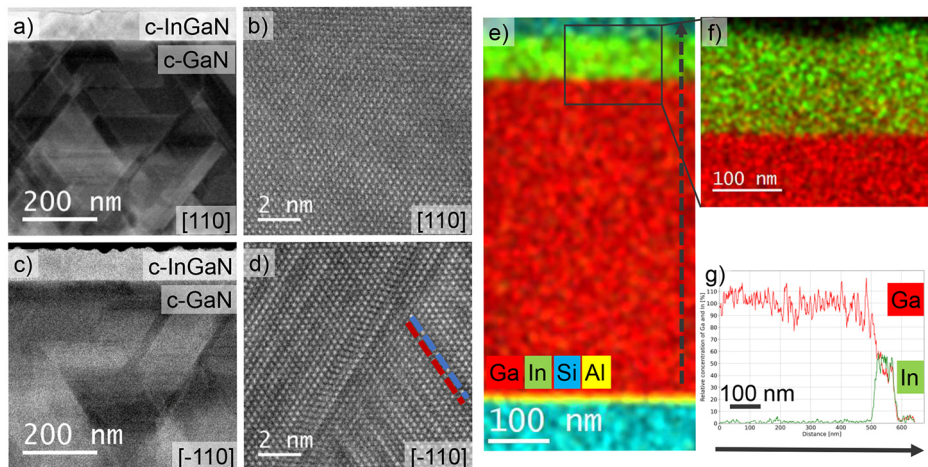


Figure 3. (a, c) STEM measurements of a sample with $x(\text{In}) = 0.47$; the defect-sensitive LAADF images show propagating stacking faults in the (a) [110] and (c) [-110] directions. (b, d) HR-HAADF images that reveal short-range CuPt-type ordering, as indicated by the red and blue dashed lines. (e, f) EDX imaging that confirms an overall homogeneous chemical composition. (g) Quantitative EDX, performed as a line scan along the black dashed line in (e), verifies the indium concentration obtained by HRXRD.

have implied spinodal decomposition into a Ga-rich and an In-rich phase, regardless of the In content. This demonstrates the full miscibility of the $c\text{-In}_x\text{Ga}_{1-x}\text{N}$ alloys. The line widths of the ω -rocking curves of the (002) $c\text{-In}_x\text{Ga}_{1-x}\text{N}$ reflection range from 30 to 140 arcmin, depending on the composition.²⁰

Strain is another aspect of the crystal structure that requires consideration, in addition to establishing the phase purity of the $c\text{-In}_x\text{Ga}_{1-x}\text{N}$ layers. For example, a standard $2\theta-\omega$ scan along [002] will be misleading in determining the indium content of partially strained $c\text{-In}_x\text{Ga}_{1-x}\text{N}$ epitaxial layers. This is because [002] is only related to the out-of-plane lattice constant a_{\perp} ; thus, this kind of scan can lead to an overestimation of the In content by up to 20%. Conversely, measuring the asymmetric reciprocal space maps of the (-1-13) reflection avoids any overestimation. This is because the (-1-13) reflections are related to both the in-plane and the out-of-plane lattice constants. Comparing the position of the $c\text{-In}_x\text{Ga}_{1-x}\text{N}$ reflection to the positions of c-GaN, the fully relaxed $c\text{-InN}$, and the fully strained $c\text{-InN}$ (Figure 2b) allows one to assess the true In content and the theoretical relaxed lattice constant a_{relax} according to Vegard's law. Using the in-plane lattice constant a_{\parallel} , the degree of relaxation R relative to the c-GaN substrate is given by²¹

$$R = \frac{a_{\parallel} - a_{\text{GaN}}}{a_{\text{relax}} - a_{\text{GaN}}} \quad (1)$$

Furthermore, the deviation of a_{\perp} from a_{relax} determines the uniaxial out-of-plane strain ε_{\perp} :

$$\varepsilon_{\perp} = \frac{a_{\perp} - a_{\text{relax}}}{a_{\text{relax}}} \quad (2)$$

Overall, the degree of relaxation increases with increasing $x(\text{In})$ (Figure 2c) due to an increasing lattice mismatch. This lattice mismatch causes a decrease in the critical thickness and, thus, faster relaxation.

In contrast, the uniaxial out-of-plane strain is highest for intermediate Ga and In contents (Figure 2d). To verify the consistency of these results, we calculated the out-of-plane strain by using two different approaches. In Figure 2d, the black squares represent the measured strain using eq 2, with a_{\perp} having been obtained via $2\theta-\omega$ scans. The blue circles denote

the calculated strain derived from the degree of relaxation using the linearly interpolated elastic constants^{21,22} of the binary compounds.^{23,24} For intermediate $x(\text{In})$, it was found that the measured strain is lower than predicted by the elastic constants. This implies that the $c\text{-In}_x\text{Ga}_{1-x}\text{N}$ layers with those compositions are not stress-free and that the elastic medium approximation is not completely accurate.²¹ In both cases, the trend of the uniaxial strain as a function of the In content resembles that of the miscibility gap in the c-GaN/InN phase diagram.^{13,14} Furthermore, theoretical calculations of the mixing free energy predict that spinodal decomposition is suppressed in fully strained $c\text{-In}_x\text{Ga}_{1-x}\text{N}$ layers on c-GaN.^{13,25} Even though the $c\text{-In}_x\text{Ga}_{1-x}\text{N}$ thin epitaxial films in this work are only partially strained (Figure 2c), the uniaxial strain is highest for the very compositions for which thermodynamics favors decomposition. This indicates that the strong uniaxial strain at intermediate $x(\text{In})$ is sufficient to counteract the predicted spinodal decomposition and is the reason for the presented full miscibility of our $c\text{-In}_x\text{Ga}_{1-x}\text{N}$ layers.

The high structural quality of the layers is confirmed by STEM images in both the [110] and [-110] directions. Exemplary images of a sample with $x(\text{In}) = 0.47$ reveal its atomic arrangement, defects, and composition. It is known that extended defects such as stacking faults are a major cause of performance loss in device applications.²⁶ Figure 3a,c show defect-sensitive LAADF-STEM images of $c\text{-In}_x\text{Ga}_{1-x}\text{N}$ on c-GaN along the two perpendicular directions. The majority of the stacking faults (SF) in the $c\text{-In}_x\text{Ga}_{1-x}\text{N}$ layer in the [110] direction (Figure 3a) originate in the c-GaN layer and penetrate the GaN/ $c\text{-In}_x\text{Ga}_{1-x}\text{N}$ interface. Those stacking faults form at the interfaces of 3C-SiC/AlN/GaN and propagate through the entire epitaxial layer if no SF annihilation process occurs.^{18,27-29} Therefore, reducing the number of SFs in the c-GaN substrate should also decrease the SF concentration in the $c\text{-In}_x\text{Ga}_{1-x}\text{N}$ layer. Apart from the SFs, the HR-HAADF image (Figure 3b) of $c\text{-In}_x\text{Ga}_{1-x}\text{N}$ shows the expected zincblende structure.

In contrast, the LAADF image of the [-110] direction (Figure 3c) shows fewer defects in c-GaN, and the $c\text{-In}_x\text{Ga}_{1-x}\text{N}$ layer appears to be homogeneous. Nevertheless, the corresponding HR-HAADF image (Figure 3d) of the c-

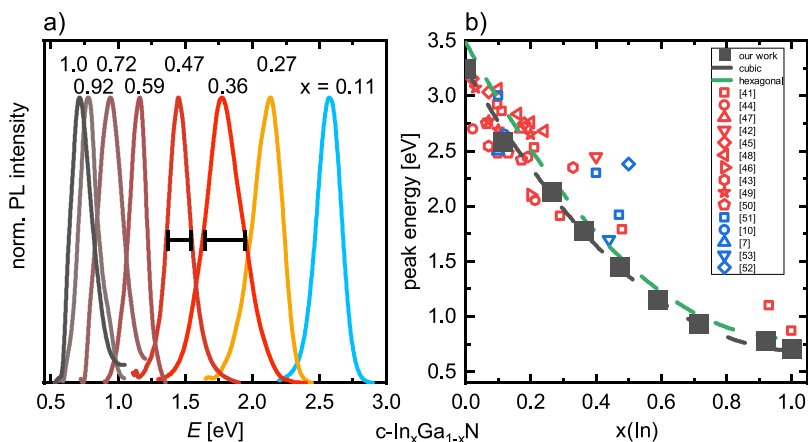


Figure 4. (a) Normalized low-temperature ($T \approx 20$ K) photoluminescence spectra of $\text{c-In}_x\text{Ga}_{1-x}\text{N}$ over the whole composition range, where x denotes indium content. (b) Peak emission energy vs $x(\text{In})$, where the black squares denote data points of this work, the red symbols refer to the emission energies of bulk $\text{c-In}_x\text{Ga}_{1-x}\text{N}$, and the blue symbols refer to the quantum structures. All data besides the black squares are taken from the literature. The bowing of the peak emission energy with $x(\text{In})$ is best described by a bowing coefficient of $b = 2.4$ eV (dashed black line).

$\text{In}_x\text{Ga}_{1-x}\text{N}$ layer reveals a parallel periodic arrangement of darker and brighter contrast along the [111] planes, which are indicated by the red and blue dashed lines, respectively. These can be assigned to In- and Ga-rich regions, respectively, based on the atomic number (Z) sensitivity of the STEM imaging. Similar arrangements, where every other layer shows brighter contrast, are known as CuPt-type ordering in the literature.^{30,31} However, the ordering observed in our samples is less periodic. Notably, this ordering is visible only in one of the two viewing directions (Figure 3d), but not in the perpendicular direction (Figure 3b). This implies the formation of sheets of In-rich and In-poor regions, rather than chains. The observed contrast would also be compatible with stacking faults that are buried in the viewing direction within the TEM sample. However, we think this is very unlikely, since the TEM sample is rather thin compared to the extensions of the stacking faults. Thus, the probability of finding a buried stacking fault would be very low. Moreover, a corresponding sample with $x(\text{In}) = 0.21$ does not show these intensity fluctuations on the {111} planes (Figure S2). CuPt-type ordering has already been observed in other highly alloyed ternary zincblende III–V materials, such as $\text{InAs}_x\text{Sb}_{1-x}$ and $\text{Ga}_x\text{In}_{1-x}\text{P}$.^{33–35} For cubic nitride alloys, this kind of ordering has not been experimentally observed to date. Nonetheless, theoretical studies of alloy energies using a cluster expansion method predict the formation of ordered phase structures in cubic nitride alloys due to strain.^{36,37} This prediction is consistent with the presented data, considering the strong uniaxial strain for samples with intermediate In content (Figure 2d).

EDX imaging of a cross section of a 3C-SiC/AlN/GaN/ $\text{In}_x\text{Ga}_{1-x}\text{N}$ sample with $x(\text{In}) = 0.47$ (Figure 3e) confirms the homogeneous chemical composition of the $\text{c-In}_x\text{Ga}_{1-x}\text{N}$ layer (Figure 3f) on larger scale lengths. Quantitative EDX analysis (Figure 3g) yields an indium content of 0.49 ± 0.12 , which is in excellent agreement with the value obtained from HRXRD.

So far, the analysis of the XRD reciprocal space maps and the EDX data gives evidence of the growth of partially relaxed $\text{c-In}_x\text{Ga}_{1-x}\text{N}$ films on c-GaN/AlN/3C-SiC/Si templates over the complete composition range. LAADF investigations reveal the distribution of the SFs in the [110] and [-110] directions, and HR-HAADF images reveal an atomistic scale CuPt-type ordering in the highly alloyed samples ($x \approx 0.5$). Next, we investigate the impact of these features on the optical

properties of the films by low-temperature photoluminescence spectroscopy and ambient-temperature micro-Raman spectroscopy.

Figure 4a shows the low-temperature photoluminescence (PL) spectra of the $\text{c-In}_x\text{Ga}_{1-x}\text{N}$ films for compositions ranging from $x(\text{In}) = 0.11–1.0$. All spectra exhibit broad, singular emission peaks with a full width at half-maximum (FWHM) of approximately 150–300 meV. Including pure c-GaN,¹⁸ the emission energies range from 3.24 to 0.71 eV, thus covering the spectral range from the near-ultraviolet (382 nm) to the near-infrared (1750 nm). The presented PL peak positions and corresponding literature data are plotted in Figure 4b as a function of the alloy composition. The presented $\text{c-In}_x\text{Ga}_{1-x}\text{N}$ data (filled black squares) are ~200 meV lower in energy for low $x(\text{In})$ ³⁸ and ~100 meV lower in energy for intermediate and high $x(\text{In})$ ^{39,40} compared to data for h- $\text{In}_x\text{Ga}_{1-x}\text{N}$ films taken from the literature (green dashed line^{39,40}). This roughly accounts for the difference in the band gap energies between the two structural modifications.^{2–6,39} Notably, while several publications report bulk cubic $\text{In}_x\text{Ga}_{1-x}\text{N}$ alloys with compositions up to 45% indium,^{41–43} data for $x > 0.9$ are more scarce.⁴¹ We go beyond these state-of-the-art reporting by obtaining emissions across the entire composition range, including the range between $x(\text{In}) = 0.5$ and 0.9. A quadratic bowing coefficient and the binary emission energies $E(\text{GaN}) = 3.24$ eV¹⁸ and $E(\text{InN}) = 0.69$ eV⁴ describe the entire composition range according to

$$E(\text{In}_x\text{Ga}_{1-x}\text{N}) = E(\text{GaN})(1 - x) + E(\text{InN})x - bx(1 - x) \quad (3)$$

A bowing coefficient of $b = 2.4$ eV yields the best fit (dashed black line in Figure 4b). This value is slightly lower than the bowing of the emission energy in hexagonal $\text{In}_x\text{Ga}_{1-x}\text{N}$ ($b \approx 2.8$ eV).^{39,40} Compared to other cubic $\text{In}_x\text{Ga}_{1-x}\text{N}$ epilayers, the emission energies reported here for low indium content ($x(\text{In}) < 0.3$) align rather well with other bulk-like thin film samples.^{41,43–50} For larger alloy compositions ($0.3 < x(\text{In}) < 0.5$), reports on the optical properties of $\text{c-In}_x\text{Ga}_{1-x}\text{N}$ are sparse. We observe emission peaks at significantly lower energies than those of other $\text{c-In}_x\text{Ga}_{1-x}\text{N}$ layers^{41–43} or multi quantum wells.^{51–53} The most recent study, ref 54, determines a significantly smaller bowing of $b = 1.4$ eV by ellipsometry measurements, which might be caused by the somewhat higher

energy values that are measured in the very highly alloyed samples with $x(\text{In}) > 0.9$ and the lack of data for $x(\text{In}) > 0.5$ (see Figure 4b). The discrepancies may also arise from the fact that our emissions may be caused by recombinations that are localized in the potential valleys of the alloys, which ellipsometry may be less sensitive to.

Investigating the photoluminescence line shape in more detail reveals that its FWHM (Figure 5) increases for alloy

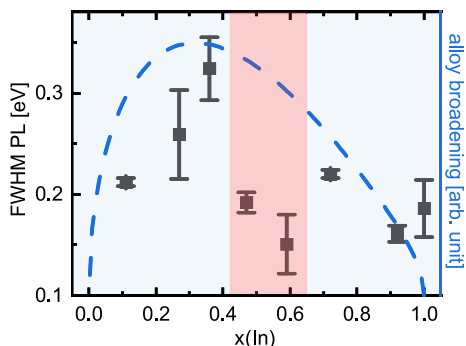


Figure 5. The FWHM values of the low-temperature PL measurements vs $x(\text{In})$. The blue dashed line represents the calculated alloy broadening due to the statistical occupation of the cation sites with Ga and In. The intermediate indium content values with narrower FWHM are highlighted in red.

concentrations up to $x(\text{In}) \leq 0.36$ and drops for $x(\text{In}) = 0.47$ and $x(\text{In}) = 0.59$. The line width broadens again for high In concentrations ($x(\text{In}) > 0.72$). The inhomogeneous broadening of radiative recombination in ternary semiconductor materials such as $c\text{-In}_x\text{Ga}_{1-x}\text{N}$ is frequently attributed to statistical fluctuations in the composition. The spectral broadening σ_0 is given by $\sigma_0 = (dE_g(x)/dx)\sigma_{\text{v}}$ ⁵⁵ with x representing the indium content and $E_g(x)$ the composition-dependent band gap. It is known that $\sigma_x^2 = x(1-x)/(cV_{\text{exc}})$, where $c = 4a_0^{-3}$ is the cation concentration⁵⁶ and $V_{\text{exc}} = 10\pi a_{\text{B},x}^{-2}$ is the exciton volume.^{55,57,58} Thus, σ_0 then becomes

$$\sigma_0 = \frac{dE_g(x)}{dx} \sqrt{\frac{x(1-x)}{ca_{\text{B},x}^{-2}}} \quad (4)$$

where $a_{\text{B},x}$ is the Bohr radius within a hydrogen model for recombination, modified by the dielectric constant ϵ and the effective masses present in the semiconductor.⁵⁹ We expect a dependence like the one given by the blue dashed line in Figure 5 if this description holds true for the entire composition range x . While the model describes the observed broadening reasonably well for low and high indium content values, the FWHM values in the intermediate indium content range ($0.47 \leq x(\text{In}) \leq 0.59$) are significantly lower than predicted. This composition range (highlighted in red) coincides with the CuPt-type ordering effect that was observed in the HR-HAADF images of the TEM investigation (Figure 3d). Because the ordering effect is on the mesoscopic scale, it has a strong effect on only the emission line width, not on the peak energy. Nevertheless, the results show that the material quality of our $c\text{-In}_x\text{Ga}_{1-x}\text{N}$ in the critical composition range of $0.47 \leq x(\text{In}) \leq 0.59$ is sufficient to exhibit radiative recombination.

Preliminary PL experiments also show the emission of our In-rich $c\text{-In}_x\text{Ga}_{1-x}\text{N}$ films at room temperature. The intensities of the spectra are about an order of magnitude lower than the

ones at 20 K, and the emission maxima shift slightly to lower energies (approximately by 30 meV). Both properties are typical for emissions caused by shallow bound recombination.

Raman spectroscopy monitors the effect In content has on the phonon structure in the films. These dynamic properties of the crystal lattice also reflect the crystal symmetry and, thus, yield additional information about its structural properties, possible phase segregation, or phase transitions. Figure 6

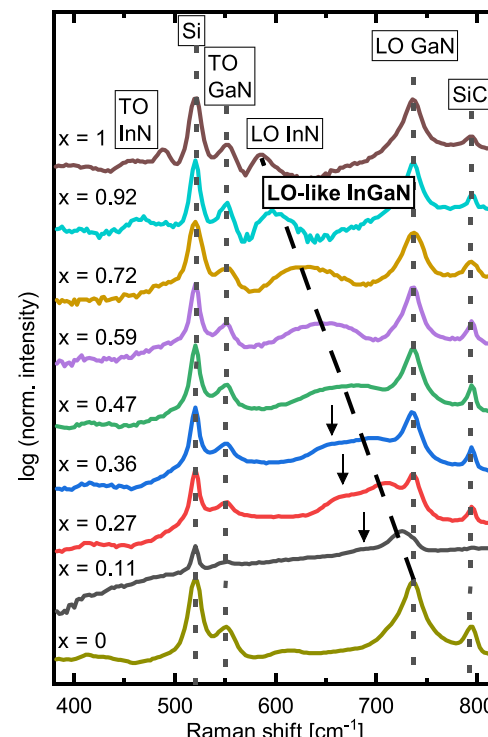


Figure 6. Raman spectra ($\lambda_{\text{exc}} = 405 \text{ nm}$) of $c\text{-In}_x\text{Ga}_{1-x}\text{N}$ ($0 \leq x \leq 1$). Substrate peaks are denoted by vertical dotted lines. The $c\text{-In}_x\text{Ga}_{1-x}\text{N}$ LO-like mode (black dashed line) shifts with the indium content amount. Black arrows highlight the positions of the secondary peaks that emerge for the low indium content spectra.

depicts the Raman spectra recorded in backscattering geometry from the (001) surfaces of the series of $c\text{-In}_x\text{Ga}_{1-x}\text{N}$ layers. The full range of $x(\text{In})$ is covered, and both binary thin films are included as references. However, due to the high penetration depth of the exciting laser light (405 nm), strong buffer and substrate modes are also visible for all $x(\text{In})$ samples, denoted by dashed lines in Figure 6.

The Raman spectra of $c\text{-In}_x\text{Ga}_{1-x}\text{N}$ epitaxial layers reveal a Raman signal which shifts linearly with $x(\text{In})$ from $c\text{-GaN}$ (737 cm^{-1} ⁶⁰) to $c\text{-InN}$ (586 cm^{-1} ⁶²). The frequency of this Raman signal is consistent with the longitudinal (LO) phonon frequency in both binary materials. This finding strongly suggests that this semiconductor alloy system exhibits a one-mode behavior that is in accordance with theoretical predictions given by the modified random-element isodisplacement (MREI) model.⁶³ In addition, a second Raman signal, which also shifts with $x(\text{In})$, is distinguishable in the vicinity of the LO-like signal for In content values in the range of $0.11 \leq x(\text{In}) \leq 0.36$ (indicated by small black arrows in Figure 6). In the In-rich samples ($0.47 \leq x(\text{In}) \leq 0.92$), either these two peaks have merged into one broad signal or the LO mode is considerably broadened. In the case of the binary $c\text{-InN}$

epitaxial film, the mode is narrower again. The most commonly given (and often correct) explanation for the broadening of the LO phonon signal is alloy disorder. The origin of additional broad Raman signals, such as the second signal observed here in close vicinity to the LO-like mode of the alloy, is often second-order Raman scattering.⁶⁴ However, in our case, it seems unlikely that second-order Raman scattering is the origin of the additional peaks seen here, based on the phonon dispersions calculated for c-GaN and c-InN.^{65,66} In our series of samples, preliminary experimental evidence suggests that both effects (i.e., the strong broadening of the LO-like phonon signal at high $x(\text{In})$ and the occurrence of a second signal at lower $x(\text{In})$) may be related to short-range CuPt-type ordering, which yields alternating In- and Ga-rich lattice planes along the [111] direction. This phenomenon is well-known from $\text{Ga}_{1-x}\text{In}_x\text{P}$ alloys with intermediate $x(\text{In})$.^{67,68} The ideal structure that corresponds to the CuPt-type ordering is a rhombohedral crystal structure, where the cubic [111] direction acts as a high symmetry three-fold rotational axis and there is a basis of four atoms (2 N, 1 Ga, 1 In) per unit cell instead of two atoms, as in zincblende crystals. In the idealized structure, the alternating (111) planes of the Ga and In atoms lead to a reduction in the cubic symmetry, accompanied by a doubling of the real space unit cell along the (111) direction. The latter corresponds to a first approximation of a bisection of the zincblende Brillouin zone between the Γ - and L-point. As a result, the zincblende phonon dispersions along this direction are basically folded back to the Γ -point. This means that two LO-like phonons (A_1 symmetry in case of the corresponding rhombohedral structure) become allowed in the presence of CuPt-type ordering. Furthermore, the theoretical work that has been done on phonon dispersions of c-GaN and c-InN^{65,66} reports that the LO phonon dispersion of c-InN between Γ and L is flatter than that of c-GaN. This suggests that two LO-like Raman signals are observable at lower In content (as indicated by the arrows in Figure 6) but then merge into one broader feature at higher In content. The frequency difference between the two signals can be estimated from the LO phonon dispersion of the corresponding zincblende material. The frequency difference calculated based on the values for c-GaN is in reasonable agreement with the frequency difference between the two Raman features observed in the spectra.

Although the transverse (TO) modes of zincblende materials are forbidden in the backscattering from (100) surfaces, corresponding modes can be discerned in the spectra of the binary materials at 551 cm^{-1} (c-GaN^{60,61,69}) and 458 cm^{-1} (c-InN^{62,65,66}). No clear signals can be discerned for the alloy thin films; this is because the anticipated Raman signals are covered by the strong signals of the LO phonon of the Si substrate and the TO mode of the c-GaN buffer layer.

CONCLUSIONS

The present work shows that the miscibility gap of c-GaN and c-InN can be overcome by sophisticated strain management in the MBE growth of cubic $\text{c-In}_x\text{Ga}_{1-x}\text{N}$ films on c-GaN/AlN/3C-SiC/Si templates. The substrate temperature governs the indium content, the growth rate, and the morphology of the film. Thorough characterization using HRXRD, Raman spectroscopy, and EDX confirms a singular, partially strained, cubic crystal phase. HR-STEM images reveal a modified CuPt-type ordering in $\text{c-In}_x\text{Ga}_{1-x}\text{N}$ when $x \approx 0.5$, which is further supported by the FWHM of the emission line width. Low-temperature photoluminescence demonstrates the tunability of

the emission energy from the near-ultraviolet to the near-infrared with a bowing coefficient of 2.4 eV. Our results encourage further efforts toward device fabrication including electrical characterization and thermal stability, as well as the growth of quantum structures for a higher emission yield and spectral optimizations.

ASSOCIATED CONTENT

Supporting Information

The Supporting Information is available free of charge at <https://pubs.acs.org/doi/10.1021/acsami.3c06319>.

Figure S1: RHEED images of samples grown at high and low growth temperatures. Figure S2: HR-STEM image of a $\text{c-In}_x\text{Ga}_{1-x}\text{N}$ layer with $x(\text{In}) = 0.21$ (PDF)

AUTHOR INFORMATION

Corresponding Author

Jörg Schörmann – Institute of Experimental Physics I and Center for Materials Research, Justus Liebig University Giessen, D-35392 Giessen, Germany;  orcid.org/0000-0001-7244-2201; Email: Joerg.Schoermann@exp1.physik.uni-giessen.de

Authors

Mario Fabian Zscherp – Institute of Experimental Physics I and Center for Materials Research, Justus Liebig University Giessen, D-35392 Giessen, Germany;  orcid.org/0000-0003-3515-5232

Silas Aurel Jentsch – Institute of Experimental Physics I and Center for Materials Research, Justus Liebig University Giessen, D-35392 Giessen, Germany

Marius Johannes Müller – Institute of Experimental Physics I and Center for Materials Research, Justus Liebig University Giessen, D-35392 Giessen, Germany;  orcid.org/0009-0005-2187-0122

Vitalii Lider – Materials Science Center and Faculty of Physics, Philipps-University Marburg, D-35032 Marburg, Germany;  orcid.org/0000-0003-4493-9370

Celina Becker – Materials Science Center and Faculty of Physics, Philipps-University Marburg, D-35032 Marburg, Germany

Limei Chen – Institute of Experimental Physics I and Center for Materials Research, Justus Liebig University Giessen, D-35392 Giessen, Germany

Mario Littmann – Department of Physics, Paderborn University, D-33098 Paderborn, Germany;  orcid.org/0000-0003-0875-3720

Falco Meier – Department of Physics, Paderborn University, D-33098 Paderborn, Germany

Andreas Beyer – Materials Science Center and Faculty of Physics, Philipps-University Marburg, D-35032 Marburg, Germany;  orcid.org/0000-0001-6533-0631

Detlev Michael Hofmann – Institute of Experimental Physics I and Center for Materials Research, Justus Liebig University Giessen, D-35392 Giessen, Germany

Donat Josef As – Department of Physics, Paderborn University, D-33098 Paderborn, Germany

Peter Jens Klar – Institute of Experimental Physics I and Center for Materials Research, Justus Liebig University Giessen, D-35392 Giessen, Germany;  orcid.org/0000-0002-4513-0330

Kerstin Volz — *Materials Science Center and Faculty of Physics, Philipps-University Marburg, D-35032 Marburg, Germany*

Sangam Chatterjee — *Institute of Experimental Physics I and Center for Materials Research, Justus Liebig University Giessen, D-35392 Giessen, Germany;* orcid.org/0000-0002-0237-5880

Complete contact information is available at:

<https://pubs.acs.org/10.1021/acsami.3c06319>

Notes

The authors declare no competing financial interest.

ACKNOWLEDGMENTS

Financial support was provided by the German Science Foundation (DFG) through the following schemes: F.M. was supported by DFG Project AS 107/7-1 and M.L. by the transregional collaborative research center TRR 142 project B02, Project 231447078; the authors from Marburg and Giessen acknowledge SFB 1083 (Project 223848855). Additionally, the work was supported through the European Regional Development Fund (ERDF) within the innovation laboratory high-performance materials FPG990 0005/2018.

REFERENCES

- (1) Binks, D. J.; Dawson, P.; Oliver, R. A.; Wallis, D. J. Cubic GaN and InGaN/GaN Quantum Wells. *Appl. Phys. Rev.* **2022**, *9* (4), 041309.
- (2) Feneberg, M.; Röppischer, M.; Cobet, C.; Esser, N.; Schörmann, J.; Schupp, T.; As, D. J.; Hörich, F.; Bläsing, J.; Krost, A.; Goldhahn, R. Optical Properties of Cubic GaN from 1 to 20 eV. *Phys. Rev. B* **2012**, *85* (15), 155207.
- (3) Church, S. A.; Hammersley, S.; Mitchell, P. W.; Kappers, M. J.; Sahonta, S. L.; Frentrup, M.; Nilsson, D.; Ward, P. J.; Shaw, L. J.; Wallis, D. J.; Humphreys, C. J.; Oliver, R. A.; Binks, D. J.; Dawson, P. Photoluminescence Studies of Cubic GaN Epilayers. *Phys. Status Solidi Basic Res.* **2017**, *254* (8), 1600733.
- (4) Schörmann, J.; As, D. J.; Lischka, K.; Schley, P.; Goldhahn, R.; Li, S. F.; Löffler, W.; Hetterich, M.; Kalt, H. Molecular Beam Epitaxy of Phase Pure Cubic InN. *Appl. Phys. Lett.* **2006**, *89* (26), 261903.
- (5) Hsiao, C. L.; Liu, T. W.; Wu, C. T.; Hsu, H. C.; Hsu, G. M.; Chen, L. C.; Shiao, W. Y.; Yang, C. C.; Gällström, A.; Holtz, P. O.; Chen, C. C.; Chen, K. H. High-Phase-Purity Zinc-Blende InN on r-Plane Sapphire Substrate with Controlled Nitridation Pretreatment. *Appl. Phys. Lett.* **2008**, *92* (11), 111914.
- (6) Nishida, K.; Kitamura, Y.; Hijikata, Y.; Yaguchi, H.; Yoshida, S. Epitaxial Growth of Hexagonal and Cubic InN Films. *Phys. Status Solidi Basic Res.* **2004**, *241* (12), 2839–2842.
- (7) Chichibu, S. F.; Sugiyama, M.; Onuma, T.; Kitamura, T.; Nakanishi, H.; Kuroda, T.; Tackeuchi, A.; Sota, T.; Ishida, Y.; Okumura, H. Localized Exciton Dynamics in Strained Cubic In_{0.1}Ga_{0.9}N/GaN Multiple Quantum Wells. *Appl. Phys. Lett.* **2001**, *79* (26), 4319.
- (8) Church, S. A.; Quinn, M.; Cooley-Greene, K.; Ding, B.; Gundimeda, A.; Kappers, M. J.; Frentrup, M.; Wallis, D. J.; Oliver, R. A.; Binks, D. J. Photoluminescence Efficiency of Zincblende InGaN/GaN Quantum Wells. *J. Appl. Phys.* **2021**, *129* (17), 175702. DOI: [10.1063/5.0046649](https://doi.org/10.1063/5.0046649).
- (9) Schörmann, J.; Potthast, S.; As, D. J.; Lischka, K. Near Ultraviolet Emission from Nonpolar Cubic Al_xGa_{1-x}N/GaN Quantum Wells. *Appl. Phys. Lett.* **2006**, *89* (13), No. 131910.
- (10) Li, S.; Schörmann, J.; As, D. J.; Lischka, K. Room Temperature Green Light Emission from Nonpolar Cubic InGaN/GaN Multi-Quantum-Wells. *Appl. Phys. Lett.* **2007**, *90* (7), No. 071903.
- (11) Tsai, Y. C.; Leburton, J. P.; Bayram, C. Quenching of the Efficiency Droop in Cubic Phase InGaN Light-Emitting Diodes. *IEEE Trans. Electron Devices* **2022**, *69* (6), 3240–3245.
- (12) Novikov, S. V.; Zainal, N.; Akimov, A. V.; Staddon, C. R.; Kent, A. J.; Foxon, C. T. Molecular Beam Epitaxy as a Method for the Growth of Freestanding Zinc-Blende (Cubic) GaN Layers and Substrates. *J. Vac. Sci. Technol. B, Nanotechnol. Microelectron. Mater. Process. Meas. Phenom.* **2010**, *28* (3), C3B1–C3B6.
- (13) Teles, L. K.; Furthmüller, J.; Scolfaro, L. M. R.; Tabata, A.; Leite, J. R.; Bechstedt, F.; Frey, T.; As, D. J.; Lischka, K. Phase Separation and Gap Bowing in Zinc-Blende InGaN, InAlN, BGaN, and BAlN Alloy Layers. *Phys. E* **2002**, *13*, 1086–1089.
- (14) Ferhat, M.; Bechstedt, F. First-Principles Calculations of Gap Bowing in In_xGa_{1-x}N and In_xAl_{1-x}N Alloys: Relation to Structural and Thermodynamic Properties. *Phys. Rev. B* **2002**, *65* (7), 1–7.
- (15) Husberg, O.; Khartchenko, A.; As, D. J.; Vogelsang, H.; Frey, T.; Schikora, D.; Lischka, K.; Noriega, O. C.; Tabata, A.; Leite, J. R. Photoluminescence from Quantum Dots in Cubic GaN/InGaN/GaN Double Heterostructures. *Appl. Phys. Lett.* **2001**, *79* (9), 1243–1245.
- (16) Husberg, O.; Khartchenko, A.; As, D. J.; Lischka, K.; Silveira, E.; Noriega, O. C.; Fernandez, J. R. L.; Leite, J. R. Thermal Annealing of Cubic-InGaN/GaN Double Heterostructures. *phys. stat. sol. (c)* **2002**, *0* (1), 293–297.
- (17) Silveira, E.; Tabata, A.; Leite, J. R.; Trentin, R.; Lemos, V.; Frey, T.; As, D. J.; Schikora, D.; Lischka, K. Evidence of Phase Separation in Cubic In_xGa_{1-x}N Epitaxial Layers by Resonant Raman Scattering. *Appl. Phys. Lett.* **1999**, *75* (23), 3602.
- (18) Zscherp, M. F.; Mengel, N.; Hofmann, D. M.; Lider, V.; Ojaghi Dogahe, B.; Becker, C.; Beyer, A.; Volz, K.; Schörmann, J.; Chatterjee, S. AlN Buffer Enhances the Layer Quality of MBE-Grown Cubic GaN on 3C-SiC. *Cryst. Growth Des.* **2022**, *22* (11), 6786–6791.
- (19) Schörmann, J.; Potthast, S.; As, D. J.; Lischka, K. In Situ Growth Regime Characterization of Cubic GaN Using Reflection High Energy Electron Diffraction. *Appl. Phys. Lett.* **2007**, *90* (4), No. 041918.
- (20) Zscherp, M. F.; Jentsch, S. A.; Müller, M. J.; Littmann, M.; Meier, F.; Hofmann, D. M.; As, D. J.; Chatterjee, S.; Schörmann, J. Growth of Cubic In_xGa_{1-x}N over Whole Composition by MBE. *Proc. SPIE 12421, Gall. Nitride Mater. Devices XVIII* **2023**, *12421* (March), 78–83.
- (21) Dunstan, D. J. Strain and Strain Relaxation in Semiconductors. *J. Mater. Sci. Mater. Electron.* **1997**, *8*, 337–375.
- (22) Frentrup, M.; Lee, L. Y.; Sahonta, S. L.; Kappers, M. J.; Massabuau, E.; Gupta, P.; Oliver, R. A.; Humphreys, C. J.; Wallis, D. J. X-Ray Diffraction Analysis of Cubic Zincblende III-Nitrides. *J. Phys. D: Appl. Phys.* **2017**, *50* (43), 433002.
- (23) Wright, A. F. Elastic Properties of Zinc-Blende and Wurtzite AlN, GaN, and InN. *J. Appl. Phys.* **1997**, *82* (6), 2833–2839.
- (24) Vurgaftman, I.; Meyer, J. R. Band Parameters for Nitrogen-Containing Semiconductors. *J. Appl. Phys.* **2003**, *94* (6), 3675–3696.
- (25) Tabata, A.; Teles, L. K.; Scolfaro, L. M. R.; Leite, J. R.; Kharchenko, A.; Frey, T.; As, D. J.; Schikora, D.; Lischka, K.; Furthmüller, J.; Bechstedt, F. Phase Separation Suppression in InGaN Epitaxial Layers Due to Biaxial Strain. *Appl. Phys. Lett.* **2002**, *80* (5), 769–771.
- (26) Kemper, R. M.; Veit, P.; Mietze, C.; Dempewolf, A.; Wecker, T.; Bertram, F.; Christen, J.; Lindner, J. K. N.; As, D. J. STEM-CL Investigations on the Influence of Stacking Faults on the Optical Emission of Cubic GaN Epilayers and Cubic GaN/AlN Multi-Quantum Wells. *Phys. Status Solidi Curr. Top. Solid State Phys.* **2015**, *12* (4–5), 469–472.
- (27) Martinez-Guerrero, E.; Bellet-Amalric, E.; Martinet, L.; Feuillet, G.; Daudin, B.; Mariette, H.; Holliger, P.; Dubois, C.; Bru-Chevallier, C.; Nze, P. A.; Chassagne, T.; Ferro, G.; Monteil, Y. Structural Properties of Undoped and Doped Cubic GaN Grown on SiC(001). *J. Appl. Phys.* **2002**, *91* (8), 4983–4987.
- (28) Lee, L. Y.; Frentrup, M.; Vacek, P.; Kappers, M. J.; Wallis, D. J.; Oliver, R. A. Investigation of Stacking Faults in MOVPE-Grown

- Zincblende GaN by XRD and TEM. *J. Appl. Phys.* **2019**, *125* (10), No. 105303.
- (29) Vacek, P.; Frentrup, M.; Lee, L. Y.; Massabuau, F. C. P.; Kappers, M. J.; Wallis, D. J.; Gröger, R.; Oliver, R. A. Defect Structures in (001) Zincblende GaN/3C-SiC Nucleation Layers. *J. Appl. Phys.* **2021**, *129* (15), 155306 DOI: [10.1063/5.0036366](https://doi.org/10.1063/5.0036366).
- (30) Johansson, C. H.; Linde, J. O. Gitterstruktur und elektrisches Leitvermögen der Mischkristallreihen Au-Cu, Pd-Cu und Pt-Cu. *Ann. Phys.* **1927**, *387* (4), 449–478.
- (31) Walker, C. B. X-Ray Measurement of Order in CuPt. *J. Appl. Phys.* **1952**, *23* (1), 118–123.
- (32) Jen, H. R.; Ma, K. Y.; Stringfellow, G. B. Long-Range Order in InAsSb. *Appl. Phys. Lett.* **1989**, *54* (12), 1154–1156.
- (33) Srivastava, G. P.; Martins, J. L.; Zunger, A. Atomic Structure and Ordering in Semiconductor Alloys. *Phys. Rev. B* **1985**, *31* (4), 2561–2564.
- (34) Bellon, P.; Chevalier, J. P.; Martin, G. P.; Dupont-Nivet, E.; Thiebaut, C.; Andre, J. P. Chemical Ordering in $\text{Ga}_x\text{In}_{1-x}\text{P}$ Semiconductor Alloy Grown by Metalorganic Vapor Phase Epitaxy. *Appl. Phys. Lett.* **1988**, *52* (7), 567–569.
- (35) Kondow, M.; Kakibayashi, H.; Minagawa, S. ORDERED STRUCTURE IN OMVPE-GROWN $\text{Ga}_0.\text{Si}_{0.5}\text{P}$. *J. Cryst. Growth* **1988**, *88*, 291–296.
- (36) Teles, L. K.; Ferreira, L. G.; Leite, J. R.; Scolfaro, L. M. R.; Kharchenko, A.; Husberg, O.; As, D. J.; Schikora, D.; Lischka, K. Strain-Induced Ordering in $\text{In}_x\text{Ga}_{1-x}\text{N}$ Alloys. *Appl. Phys. Lett.* **2003**, *82* (24), 4274–4276.
- (37) Teles, L. K.; Marques, M.; Ferreira, L. G.; Scolfaro, L. M. R.; Leite, J. R. Phase Separation, Effects of Biaxial Strain, and Ordered Phase Formations in Cubic Nitride Alloys. *Microelectronics J.* **2004**, *35*, 53–57.
- (38) Islam, M. R.; Kaysir, M. R.; Islam, M. J.; Hashimoto, A.; Yamamoto, A. MOVPE Growth of $\text{In}_x\text{Ga}_{1-x}\text{N}$ ($x \sim 0.4$) and Fabrication of Homo-Junction Solar Cells. *J. Mater. Sci. Technol.* **2013**, *29* (2), 128–136.
- (39) Kazazis, S. A.; Papadomanolaki, E.; Androulidaki, M.; Kayambaki, M.; Iliopoulos, E. Optical Properties of InGaN Thin Films in the Entire Composition Range. *J. Appl. Phys.* **2018**, *123* (12), 125101 DOI: [10.1063/1.5020988](https://doi.org/10.1063/1.5020988).
- (40) Moret, M.; Gil, B.; Ruffenach, S.; Briot, O.; Giesen, C.; Heukens, M.; Rushworth, S.; Leese, T.; Succi, M. Optical, Structural Investigations and Band-Gap Bowing Parameter of GaInN Alloys. *J. Cryst. Growth* **2009**, *311* (10), 2795–2797.
- (41) Compeán García, V. D.; Orozco Hinostroza, I. E.; Escobosa Echavarria, A.; López Luna, E.; Rodríguez, A. G.; Vidal, M. A. Bulk Lattice Parameter and Band Gap of Cubic $\text{In}_x\text{Ga}_{1-x}\text{N}$ (001) Alloys on MgO (100) Substrates. *J. Cryst. Growth* **2015**, *418*, 120–125.
- (42) Brandt, O.; Müllhäuser, J. R.; Trampert, A.; Ploog, K. H. Properties of Cubic (In,Ga)N Grown by Molecular Beam Epitaxy. *Mater. Sci. Eng., B* **1999**, *59* (1–3), 73–79.
- (43) Lemos, V.; Silveira, E.; Leite, J. R.; Tabata, A.; Trentin, R.; Scolfaro, L. M. R.; Frey, T.; As, D. J.; Schikora, D.; Lischka, K. Evidence for Phase-Separated Quantum Dots in Cubic InGaN Layers from Resonant Raman Scattering. *Phys. Rev. Lett.* **2000**, *84* (16), 3666–3669.
- (44) Chichibu, S. F.; Sugiyama, M.; Kuroda, T.; Tackeuchi, A.; Kitamura, T.; Nakanishi, H.; Sota, T.; DenBaars, S. P.; Nakamura, S.; Ishida, Y.; Okumura, H. Band Gap Bowing and Exciton Localization in Strained Cubic $\text{In}_x\text{Ga}_{1-x}\text{N}$ Films Grown on 3C-SiC (001) by RF Molecular-Beam Epitaxy. *Appl. Phys. Lett.* **2001**, *79* (22), 3600–3602.
- (45) Goldhahn, R.; Scheiner, J.; Shokhovets, S.; Frey, T.; Köhler, U.; As, D. J.; Lischka, K. Refractive Index and Gap Energy of Cubic $\text{In}_x\text{Ga}_{1-x}\text{N}$. *Appl. Phys. Lett.* **2000**, *76* (3), 291–293.
- (46) Kitamura, T.; Cho, S. H.; Ishida, Y.; Ide, T.; Shen, X. Q.; Nakanishi, H.; Chichibu, S.; Okumura, H. Growth and Characterization of Cubic InGaN Epilayers on 3C-SiC by RF MBE. *J. Cryst. Growth* **2001**, *227*–*228*, 471–475.
- (47) Müllhäuser, J. R.; Jenichen, B.; Wassermeier, M.; Brandt, O.; Ploog, K. H. Characterization of Zinc Blende $\text{In}_x\text{Ga}_{1-x}\text{N}$ Grown by Radio Frequency Plasma Assisted Molecular Beam Epitaxy on GaAs (001). *Appl. Phys. Lett.* **1997**, *71* (7), 909–911.
- (48) Sun, X. L.; Wang, Y. T.; Yang, H.; Zheng, L. X.; Xu, D. P.; Li, J. B.; Wang, Z. G. Strain and Photoluminescence Characterization of Cubic (In,Ga)N Films Grown on GaAs(001) Substrates. *J. Appl. Phys.* **2000**, *87* (8), 3711–3714.
- (49) Holst, J.; Hoffmann, A.; Rudloff, D.; Bertram, F.; Riemann, T.; Christen, J.; Frey, T.; As, D. J.; Schikora, D.; Lischka, K. The Origin of Optical Gain in Cubic InGaN Grown by Molecular Beam Epitaxy. *Appl. Phys. Lett.* **2000**, *76* (20), 2832–2834.
- (50) Pacheco-Salazar, D. G.; Leite, J. R.; Cerdeira, F.; Meneses, E. A.; Li, S. F.; As, D. J.; Lischka, K. Photoluminescence Measurements on Cubic InGaN Layers Deposited on a SiC Substrate. *Semicond. Sci. Technol.* **2006**, *21* (7), 846–851.
- (51) Orozco Hinostroza, I. E.; Avalos-Borja, M.; Compeán García, V. D.; Zamora, C. C.; Rodríguez, A. G.; López Luna, E.; Vidal, M. A. Tuning Emission in Violet, Blue, Green and Red in Cubic GaN/InGaN/GaN Quantum Wells. *J. Cryst. Growth* **2016**, *435*, 110–113.
- (52) Chichibu, S. F.; Setoguchi, A.; Azuhata, T.; Müllhäuser, J.; Sugiyama, M.; Mizutani, T.; Deguchi, T.; Nakanishi, H.; Sota, T.; Brandt, O.; Ploog, K. H.; Mukai, T.; Nakamura, S. Effective Localization of Quantum Well Excitons in InGaN Quantum Well Structures with High InN Mole Fraction. *phys. stat. sol. (a)* **2000**, *180*, 321–325.
- (53) Compeán-García, V.D.; Hernandez-Vazquez, O.; Garcia-Hernandez, S.A.; Luna, E.L.; Vidal, M.A. Critical Thickness as a Function of the Indium Molar Fraction in Cubic $\text{In}_x\text{Ga}_{1-x}\text{N}$ and the Influence in the Growth of Nanostructures. *Mater. Sci. Semicond. Process.* **2020**, *115*, 105101.
- (54) Vilchis, H.; Compeán-García, V. D.; Orozco-Hinostroza, I. E.; López-Luna, E.; Vidal, M. A.; Rodríguez, A. G. Complex Refractive Index of $\text{In}_x\text{Ga}_{1-x}\text{N}$ Thin Films Grown on Cubic (100) GaN/MgO. *Thin Solid Films* **2017**, *626*, 55–59.
- (55) Grundmann, M.; Dietrich, C. P. Lineshape Theory of Photoluminescence from Semiconductor Alloys. *J. Appl. Phys.* **2009**, *106* (12), No. 123521.
- (56) Schubert, E. F.; Göbel, E. O.; Horikoshi, Y.; Ploog, K.; Queisser, H. J. Alloy Broadening in Photoluminescence Spectra of $\text{Al}_x\text{Ga}_{1-x}\text{As}$. *Phys. Rev. B* **1984**, *30* (2), 813–820.
- (57) Goede, O.; John, L.; Hennig, D. Compositional Disorder-Induced Broadening for Free Excitons in II-VI Semiconducting Mixed Crystals. *Phys. stat. sol. b* **1978**, *89*, K183.
- (58) Zimmermann, R. Theory of Exciton Linewidth in II-VI Semiconductor Mixed Crystals. *J. Cryst. Growth* **1990**, *101* (1–4), 346–349.
- (59) Fritsch, D.; Schmidt, H.; Grundmann, M. Band-Structure Pseudopotential Calculation of Zinc-Blende and Wurtzite AlN, GaN, and InN. *Phys. Rev. B - Condens. Matter Mater. Phys.* **2003**, *67* (23), 1–13.
- (60) Yaguchi, H.; Wu, J.; Zhang, B.; Segawa, Y.; Nagasawa, H.; Onabe, K.; Shiraki, Y. Micro Raman and Micro Photoluminescence Study of Cubic GaN Grown on 3C-SiC(0 0 1) Substrates by Metalorganic Vapor Phase Epitaxy. *J. Cryst. Growth* **1998**, *195* (1–4), 323–327.
- (61) Giehler, M.; Ramsteiner, M.; Brandt, O.; Yang, H.; Ploog, K. H. Optical Phonons of Hexagonal and Cubic GaN Studied by Infrared Transmission and Raman Spectroscopy. *Appl. Phys. Lett.* **1995**, *67* (6), 733–735.
- (62) Tabata, A.; Lima, A. P.; Teles, L. K.; Scolfaro, L. M. R.; Leite, J. R.; Lemos, V.; Schöttker, B.; Frey, T.; Schikora, D.; Lischka, K. Structural Properties and Raman Modes of Zinc Blende InN Epitaxial Layers. *Appl. Phys. Lett.* **1999**, *74* (3), 362–364.
- (63) Grille, H.; Schnittler, C.; Bechstedt, F. Phonons in Ternary Group-III Nitride Alloys. *Phys. Rev. B - Condens. Matter Mater. Phys.* **2000**, *61* (9), 6091–6105.
- (64) Haboeck, U.; Siegle, H.; Hoffmann, A.; Thomsen, C. Lattice Dynamics in GaN and AlN Probed with First- and Second-Order Raman Spectroscopy. *Phys. Status Solidi C* **2003**, *0* (6), 1710–1731.

- (65) Xia, H.; Feng, Y.; Patterson, R.; Jia, X.; Shrestha, S.; Conibeer, G. Theoretical Calculation of the Vibrational and Thermal Properties of Wurtzite InN-GaN Multiple Quantum Well Superlattice. *J. Appl. Phys.* **2013**, *113* (16), 164304.
- (66) Bağcı, S.; Duman, S.; Tütüncü, H. M.; Srivastava, G. P. Ab Initio Calculations of Phonon Dispersion Relations for Bulk and (1 1 0) Surface of Cubic InN. *J. Phys. Chem. Solids* **2009**, *70* (2), 444–450.
- (67) Gant, T. A.; Dutta, M.; El-Masry, N. A.; Bedair, S. M.; Stroscio, M. A. Raman Study of Ordering in Ga_{1-x}In_xP. *Phys. Rev. B* **1992**, *46* (7), 3834–3838.
- (68) Mintairov, A. M.; Merz, J. L.; Vlasov, A. S.; Vinokurov, D. V. Observation of a Martensitic Transition in the Raman Spectra of Spontaneously Ordered GaInP Alloys. *Semicond. Sci. Technol.* **1998**, *13* (10), 1140–1147.
- (69) Baron, E.; Feneberg, M.; Goldhahn, R.; Deppe, M.; Tacken, F.; As, D. J. Optical Evidence of Many-Body Effects in the Zincblende Al_xGa_{1-x}N Alloy System. *J. Phys. D. Appl. Phys.* **2021**, *54* (2), 025101.

Conclusion & Outlook

This dissertation advances the growth of cubic group III-nitrides using plasma-assisted molecular-beam epitaxy and reveals previously unreported materials properties. The publications of this work address multiple aspects that previously limited the application of cubic III-nitrides with emphasis on the ternary alloy $c\text{-In}_x\text{Ga}_{1-x}\text{N}$. They improve the layer quality of c-III-nitrides and overcome the miscibility gap of c-GaN and c-InN.

Publication 1 enhances the epitaxial growth of c-GaN on 3C-SiC by introducing a thin c-AlN buffer layer between substrate and epilayer. The c-AlN buffer spatially separates the change of ionicity and the lattice mismatch of c-GaN and 3C-SiC. Thorough characterization with HRXRD, AFM, STEM and PL proves that the addition of the buffer layer improves the crystal quality, surface roughness, phase purity and optical properties of cubic GaN beyond current standards. These smooth c-GaN layers, with an RMS roughness below 1 nm, are used as pseudo-substrates for the subsequent heteroepitaxial growth of other cubic nitride compounds.

Publication 2 demonstrates the growth of $c\text{-In}_x\text{Ga}_{1-x}\text{N}$ layers on these c-GaN templates with $x(\text{In})$ spanning the entire composition range. The substrate temperature is the most important growth parameter. It governs the indium content, growth rate and surface morphology. Structural characterization including reciprocal space mapping confirms a singular, partially strained, cubic phase. Further strain analysis reveals that the uniaxial out-of-plane strain is especially high for intermediate $x(\text{In})$ and suggests that this strain prevents spinodal decomposition into a Ga-rich and an In-rich phase. The alloys in the intermediate composition regime and their properties were previously inaccessible. STEM images infer a modified CuPt-type ordering along the [11] direction for $c\text{-In}_x\text{Ga}_{1-x}\text{N}$ with $x(\text{In}) \approx 0.5$. These findings are corroborated by the photoluminescence linewidth, which is narrower for intermediate $x(\text{In})$. However, Raman spectroscopy suggests the presence of short-range ordering independent of composition. Low-temperature photoluminescence demonstrates the tunability of the emission energy from the near-ultraviolet to the near-infrared. The continuity of data points allows a reliable determination of the bowing coefficient ($b = 2.4$ eV) of the emission energy without the need for extrapolation.

With the successful demonstration of the tunability of composition and emission energy, $c\text{-In}_x\text{Ga}_{1-x}\text{N}$ alloys now fulfill a fundamental requirement for their application in multi-color light-emitting diodes. The path towards this goal is full of research and developments opportunities: For example, the layer quality of $c\text{-In}_x\text{Ga}_{1-x}\text{N}$ still retains significant development potential. A promising approach is employing unconventional growth schemes such as a modulated growth sequence where the Ga and In shutters are alternatingly opened¹¹⁶.

Conclusion & Outlook

Using this modulated binary growth could increase stabilization of the cubic phase in thicker layers and offers intrinsic advantages for fabricating nanostructures¹¹⁷. Another approach is replacing the c-AlN buffer with a compositionally graded c-AlGaN multi-layer^{118,119}. This promises a successive decrease in lattice mismatch and could lead to additional improvement of the c-GaN pseudo-substrate. In addition, GaP/Si (001) could be an alternative substrate choice which facilitates the integration in silicon technologies.

The low surface roughness of the c-In_xGa_{1-x}N layers of this work is very encouraging for the fabrication of multi quantum well structures which require smooth interfaces. If implemented correctly, the quantum confinement in such structures enhances the emission yield. Experimentally, this can be verified by comparing the excitation power to the integrated luminescence intensity captured by an Ulbricht sphere^{115,120}. Ultimately, the path towards device fabrication demands control of the carrier population by doping. Si or Ge could be used as n-type^{121,122} dopant, whereas Mg is a p-type dopant^{123,124}. Implementing this will require careful evaluation of the carrier concentration and the majority carrier polarity, for example by Hall measurements.

The key concepts of this work are also applicable to other materials beyond cubic nitrides. Buffer layers are already commonly used in heteroepitaxy to improve crystal quality. Similarly, strain could be purposely utilized to unlock the miscibility of other highly mismatched alloys such as B_xGa_{1-x}N, B_xAl_{1-x}N, In_xAl_{1-x}N and Ga₂(O_{1-x}S_x)₃ and to synthesize novel materials.

Bibliography

- (1) Lidow, A.; de Rooij, M.; Strydom, J.; Reusch, D.; Glaser, J. *GaN Transistors for Efficient Power Conversion*, 3rd ed.; John Wiley & Sons, 2019.
- (2) Yanagihara, M.; Uemoto, Y.; Ueda, T.; Tanaka, T.; Ueda, D. Recent Advances in GaN Transistors for Future Emerging Applications. *Phys. Status Solidi Appl. Mater. Sci.* **2009**, 206 (6), 1221–1227. <https://doi.org/10.1002/pssa.200880968>.
- (3) Sun, R.; Lai, J.; Chen, W.; Zhang, B. GaN Power Integration for High Frequency and High Efficiency Power Applications: A Review. *IEEE Access* **2020**, 8, 15529–15542. <https://doi.org/10.1109/ACCESS.2020.2967027>.
- (4) Würtele, M. A.; Kolbe, T.; Lipsz, M.; Külberg, A.; Weyers, M.; Kneissl, M.; Jekel, M. Application of GaN-Based Ultraviolet-C Light Emitting Diodes - UV LEDs - for Water Disinfection. *Water Res.* **2011**, 45 (3), 1481–1489. <https://doi.org/10.1016/j.watres.2010.11.015>.
- (5) Kneissl, M.; Seong, T. Y.; Han, J.; Amano, H. The Emergence and Prospects of Deep-Ultraviolet Light-Emitting Diode Technologies. *Nat. Photonics* **2019** 134 **2019**, 13 (4), 233–244. <https://doi.org/10.1038/S41566-019-0359-9>.
- (6) Lin, R.; Liu, X.; Zhou, G.; Qian, Z.; Cui, X.; Tian, P. InGaN Micro-LED Array Enabled Advanced Underwater Wireless Optical Communication and Underwater Charging. *Adv. Opt. Mater.* **2021**, 9 (12). <https://doi.org/10.1002/adom.202002211>.
- (7) Lu, S.; Li, J.; Huang, K.; Liu, G.; Zhou, Y.; Cai, D.; Zhang, R.; Kang, J. Designs of InGaN Micro-LED Structure for Improving Quantum Efficiency at Low Current Density. *Nanoscale Res. Lett.* **2021**, 16 (99). <https://doi.org/10.1186/s11671-021-03557-4>.
- (8) Horng, R. H.; Ye, C. X.; Chen, P. W.; Iida, D.; Ohkawa, K.; Wu, Y. R.; Wuu, D. S. Study on the Effect of Size on InGaN Red Micro-LEDs. *Sci. Rep.* **2022**, 12 (1324). <https://doi.org/10.1038/s41598-022-05370-0>.
- (9) White, R. C.; Li, H.; Khouri, M.; Lynsky, C.; Iza, M.; Keller, S.; Sotta, D.; Nakamura, S.; DenBaars, S. P. InGaN-Based MicroLED Devices Approaching 1% EQE with Red 609 nm Electroluminescence on Semi-Relaxed Substrates. *Crystals* **2021**, 11 (11), 1364. <https://doi.org/10.3390/cryst11111364>.
- (10) Choi, H. W.; Jeon, C. W.; Dawson, M. D.; Edwards, P. R.; Martin, R. W. Fabrication and Performance of Parallel-Addressed InGaN Micro-LED Arrays. *IEEE PHOTONICS Technol. Lett.* **2003**, 15 (4), 510–512. <https://doi.org/https://doi.org/10.1109/LPT.2003.809257>.
- (11) Kazazis, S. A.; Papadomanolaki, E.; Androulidaki, M.; Kayambaki, M.; Iliopoulos, E. Optical Properties of InGaN Thin Films in the Entire Composition Range. *J. Appl. Phys.* **2018**, 123 (125101). <https://doi.org/10.1063/1.5020988>.
- (12) Moret, M.; Gil, B.; Ruffenach, S.; Briot, O.; Giesen, C.; Heuken, M.; Rushworth, S.; Leese, T.; Succi, M. Optical, Structural Investigations and Band-Gap Bowing Parameter of GaInN Alloys. *J. Cryst. Growth* **2009**, 311 (10), 2795–2797. <https://doi.org/10.1016/j.jcrysGro.2009.01.009>.

Bibliography

- (13) Feneberg, M.; Röppischer, M.; Cobet, C.; Esser, N.; Schörmann, J.; Schupp, T.; As, D. J.; Hörich, F.; Bläsing, J.; Krost, A.; Goldhahn, R. Optical Properties of Cubic GaN from 1 to 20 EV. *Phys. Rev. B* **2012**, *85* (155207), 1-. <https://doi.org/10.1103/PhysRevB.85.155207>.
- (14) Church, S. A.; Hammersley, S.; Mitchell, P. W.; Kappers, M. J.; Sahonta, S. L.; Frentrup, M.; Nilsson, D.; Ward, P. J.; Shaw, L. J.; Wallis, D. J.; Humphreys, C. J.; Oliver, R. A.; Binks, D. J.; Dawson, P. Photoluminescence Studies of Cubic GaN Epilayers. *Phys. Status Solidi Basic Res.* **2017**, *254* (8). <https://doi.org/10.1002/pssb.201600733>.
- (15) Schörmann, J.; As, D. J.; Lischka, K.; Schley, P.; Goldhahn, R.; Li, S. F.; Löffler, W.; Hetterich, M.; Kalt, H. Molecular Beam Epitaxy of Phase Pure Cubic InN. *Appl. Phys. Lett.* **2006**, *89* (261903). <https://doi.org/10.1063/1.2422913>.
- (16) Hsiao, C. L.; Liu, T. W.; Wu, C. T.; Hsu, H. C.; Hsu, G. M.; Chen, L. C.; Shiao, W. Y.; Yang, C. C.; Gällström, A.; Holtz, P. O.; Chen, C. C.; Chen, K. H. High-Phase-Purity Zinc-Blende InN on r -Plane Sapphire Substrate with Controlled Nitridation Pretreatment. *Appl. Phys. Lett.* **2008**, *92* (111914). <https://doi.org/10.1063/1.2898214>.
- (17) Nishida, K.; Kitamura, Y.; Hijikata, Y.; Yaguchi, H.; Yoshida, S. Epitaxial Growth of Hexagonal and Cubic InN Films. *Phys. Status Solidi Basic Res.* **2004**, *241* (12), 2839–2842. <https://doi.org/10.1002/pssb.200405049>.
- (18) Pattison, M.; Hansen, M.; Bardsley, N.; Elliott, C.; Lee, K.; Pattison, L.; Tsao, J. 2019 Lighting Research and Development Opportunities. *Rep. No. DOE/EE-2008 8189 (U.S. Dep. Energy, Off. Energy Effic. Renew. Energy)* **2020**, No. January. <https://doi.org/https://doi.org/10.2172/1618035>.
- (19) Tsai, Y. C.; Leburton, J. P.; Bayram, C. Quenching of the Efficiency Droop in Cubic Phase InGaN Light-Emitting Diodes. *IEEE Trans. Electron Devices* **2022**, *69* (6), 3240–3245. <https://doi.org/10.1109/TED.2022.3167645>.
- (20) Ren, C. X. Polarisation Fields in III-Nitrides: Effects and Control. *Mater. Sci. Technol. (United Kingdom)* **2016**, *32* (5), 418–433. <https://doi.org/10.1179/1743284715Y.0000000103>.
- (21) Binks, D. J.; Dawson, P.; Oliver, R. A.; Wallis, D. J. Cubic GaN and InGaN/GaN Quantum Wells. *Appl. Phys. Rev.* **2022**, *9* (041309). <https://doi.org/10.1063/5.0097558>.
- (22) Humphreys, C. J.; Grif, J. T.; Tang, F.; Oehler, F.; Findlay, S. D.; Zheng, C.; Etheridge, J.; Martin, T. L.; Bagot, P. A. J.; Moody, M. P.; Sutherland, D.; Dawson, P.; Schulz, S.; Zhang, S.; Fu, W. Y.; Zhu, T.; Kappers, M. J.; Oliver, R. A. The Atomic Structure of Polar and Non-Polar InGaN Quantum Wells and the Green Gap Problem. *Ultramicroscopy* **2017**, *176*, 93–98. <https://doi.org/10.1016/j.ultramic.2017.01.019>.
- (23) Lähnemann, J.; Brandt, O.; Jahn, U.; Pfüller, C.; Roder, C.; Dogan, P.; Grosse, F.; Belabbes, A.; Bechstedt, F.; Trampert, A.; Geelhaar, L. Direct Experimental Determination of the Spontaneous Polarization of GaN. *Phys. Rev. B - Condens. Matter Mater. Phys.* **2012**, *86* (8), 1–5. <https://doi.org/10.1103/PhysRevB.86.081302>.

- (24) Bernardini, F.; Fiorentini, V.; Vanderbilt, D. Spontaneous Polarization and Piezoelectric Constants of III-V Nitrides. *Phys. Rev. B - Condens. Matter Mater. Phys.* **1997**, *56* (16), R10024–R10027. <https://doi.org/10.1103/PhysRevB.56.R10024>.
- (25) Auf Der Maur, M.; Pecchia, A.; Penazzi, G.; Rodrigues, W.; Di Carlo, A. Efficiency Drop in Green InGaN/GaN Light Emitting Diodes: The Role of Random Alloy Fluctuations. *Phys. Rev. Lett.* **2016**, *116* (2), 1–5. <https://doi.org/10.1103/PhysRevLett.116.027401>.
- (26) Chichibu, S. F.; Sugiyama, M.; Onuma, T.; Kitamura, T.; Nakanishi, H.; Kuroda, T.; Tackeuchi, A.; Sota, T.; Ishida, Y.; Okumura, H. Localized Exciton Dynamics in Strained Cubic $\text{In}_{0.1}\text{Ga}_{0.9}\text{N}/\text{GaN}$ Multiple Quantum Wells. *Appl. Phys. Lett.* **2001**, *79* (26). <https://doi.org/10.1063/1.1428404>.
- (27) Church, S. A.; Quinn, M.; Cooley-Greene, K.; Ding, B.; Gundimeda, A.; Kappers, M. J.; Frentrup, M.; Wallis, D. J.; Oliver, R. A.; Binks, D. J. Photoluminescence Efficiency of Zincblende InGaN/GaN Quantum Wells. *J. Appl. Phys.* **2021**, *129* (17). <https://doi.org/10.1063/5.0046649>.
- (28) Schörmann, J.; Potthast, S.; As, D. J.; Lischka, K. Near Ultraviolet Emission from Nonpolar Cubic $\text{Al}_x\text{Ga}_{1-x}\text{N}/\text{GaN}$ Quantum Wells. *Appl. Phys. Lett.* **2006**, *89* (13), 131910. <https://doi.org/10.1063/1.2357587>.
- (29) Li, S.; Schörmann, J.; As, D. J.; Lischka, K. Room Temperature Green Light Emission from Nonpolar Cubic $\text{In}_{x}\text{Ga}_{1-x}\text{N}/\text{GaN}$ Multi-Quantum-Wells. *Appl. Phys. Lett.* **2007**, *90* (7), 071903. <https://doi.org/10.1063/1.2475564>.
- (30) Frentrup, M.; Lee, L. Y.; Sahonta, S. L.; Kappers, M. J.; Massabuau, F.; Gupta, P.; Oliver, R. A.; Humphreys, C. J.; Wallis, D. J. X-Ray Diffraction Analysis of Cubic Zincblende III-Nitrides. *J. Phys. D. Appl. Phys.* **2017**, *50* (43). <https://doi.org/10.1088/1361-6463/aa865e>.
- (31) Teles, L. K.; Furthmuller, J.; Scolfaro, L. M. R.; Tabata, A.; Leite, J. R.; Bechstedt, F.; Frey, T.; As, D. J.; Lischka, K. Phase Separation and Gap Bowing in Zinc-Blende InGaN, InAlN, BGaN, and BAlN Alloy Layers. *Phys. E* **2002**, *13*, 1086–1089. [https://doi.org/10.1016/S1386-9477\(02\)00309-0](https://doi.org/10.1016/S1386-9477(02)00309-0).
- (32) Ferhat, M.; Bechstedt, F. First-Principles Calculations of Gap Bowing in $\text{In}_{x}\text{Ga}_{1-x}\text{N}$ and $\text{In}_{x}\text{Al}_{1-x}\text{N}$ Alloys: Relation to Structural and Thermodynamic Properties. *Phys. Rev. B* **2002**, *65* (7), 1–7. <https://doi.org/10.1103/PhysRevB.65.075213>.
- (33) Husberg, O.; Khartchenko, A.; As, D. J.; Vogelsang, H.; Frey, T.; Schikora, D.; Noriega, O. C.; Tabata, A.; Leite, J. R. Photoluminescence from Quantum Dots in Cubic GaN / InGaN / GaN Double Heterostructures. *Appl. Phys. Lett.* **2001**, *79* (9), 1243–1245. <https://doi.org/10.1063/1.1396314>.
- (34) Husberg, O.; Khartchenko, A.; As, D. J.; Lischka, K.; Silveira, E.; Noriega, O. C.; Fernandez, J. R. L.; Leite, J. R. Thermal Annealing of Cubic-InGaN / GaN Double Heterostructures. *phys. stat. sol. c* **2002**, *0* (1), 293–297. <https://doi.org/10.1002/pssc.200390046>.
- (35) Silveira, E.; Tabata, A.; Leite, J. R.; Trentin, R.; Lemos, V.; Frey, T.; As, D. J.; Schikora, D.; Lischka, K. Evidence of Phase Separation in Cubic $\text{In}_{x}\text{Ga}_{1-x}\text{N}$ Epitaxial Layers by Resonant Raman Scattering. *Appl. Phys. Lett.* **1999**, *75* (23). <https://doi.org/10.1063/1.125401>.

Bibliography

- (36) Jia, W.; Sensale-Rodriguez, B. Terahertz Metamaterial Modulators Based on Wide-Bandgap Semiconductor Lateral Schottky Diodes. *Opt. Mater. Express* **2022**, *12* (3), 940–948. <https://doi.org/https://doi.org/10.1364/OME.451027>.
- (37) Keshmiri, N.; Wang, D.; Agrawal, B.; Hou, R.; Emadi, A. Current Status and Future Trends of GaN HEMTs in Electrified Transportation. *IEEE Access* **2020**, *8*, 70553–70571. <https://doi.org/10.1109/ACCESS.2020.2986972>.
- (38) Amano, H.; Asahi, T.; Akasaki, I. Stimulated Emission Near Ultraviolet at Room Temperature from a GaN Film Grown on Sapphire by MOVPE Using an AlN Buffer Layer. *Jpn. J. Appl. Phys.* **1990**, *29* (2), L205–L206. <https://doi.org/10.1143/JJAP.29.L205>.
- (39) Isamu Akasaki; Hiroshi Amano; Masahiro Kito; Kazumasa Hiramatsu. Photoluminescence of Mg-Doped p-Type GaN and Electroluminescence of GaN p-n Junction LED. *J. Lumin.* **1991**, *48–49* (PART 2), 666–670. [https://doi.org/10.1016/0022-2313\(91\)90215-H](https://doi.org/10.1016/0022-2313(91)90215-H).
- (40) Nakamura, S.; Mukai, T.; Senoh, M. Candela-class High-brightness InGaN/AlGaN Double-heterostructure Blue-light-emitting Diodes. *Appl. Phys. Lett.* **1994**, *64* (13), 1687–1689. <https://doi.org/10.1063/1.111832>.
- (41) Akasaki, I.; Amano, H.; Nakamura, S. The Nobel Prize in Physics 2014. *R. Swedish Acad. Sci.* **2014**. <https://doi.org/10.1063/1.4770511>.
- (42) Narukawa, Y.; Ichikawa, M.; Sanga, D.; Sano, M.; Mukai, T. White Light Emitting Diodes with Super-High Luminous Efficacy. *J. Phys. D. Appl. Phys.* **2010**, *43* (35), 354002. <https://doi.org/10.1088/0022-3727/43/35/354002>.
- (43) Vurgaftman, I.; Meyer, J. R. Band Parameters for Nitrogen-Containing Semiconductors. *J. Appl. Phys.* **2003**, *94* (6), 3675–3696. <https://doi.org/10.1063/1.1600519>.
- (44) Schupp, T.; Lischka, K.; As, D. J. MBE Growth of Atomically Smooth Non-Polar Cubic AlN. *J. Cryst. Growth* **2010**, *312* (9), 1500–1504. <https://doi.org/10.1016/j.jcrysGro.2010.01.040>.
- (45) Novikov, S. V.; Zainal, N.; Akimov, A. V.; Staddon, C. R.; Kent, A. J.; Foxon, C. T. Molecular Beam Epitaxy as a Method for the Growth of Freestanding Zinc-Blende (Cubic) GaN Layers and Substrates. *J. Vac. Sci. Technol. B, Nanotechnol. Microelectron. Mater. Process. Meas. Phenom.* **2010**, *28* (3), C3B1–C3B6. <https://doi.org/10.1116/1.3276426>.
- (46) Zoroddu, A.; Bernardini, F.; Ruggerone, P.; Fiorentini, V. First-Principles Prediction of Structure, Energetics, Formation Enthalpy, Elastic Constants, Polarization, and Piezoelectric Constants of AlN, GaN, and InN: Comparison of Local and Gradient-Corrected Density-Functional Theory. *Phys. Rev. B - Condens. Matter Mater. Phys.* **2001**, *64* (4), 1–6. <https://doi.org/10.1103/PhysRevB.64.045208>.
- (47) Mattila, T.; Zunger, A. Predicted Bond Length Variation in Wurtzite and Zinc-Blende InGaN and AlGaN Alloys. *J. Appl. Phys.* **1999**, *85* (1), 160–167. <https://doi.org/10.1063/1.369463>.

- (48) Ambacher, O.; Majewski, J.; Miskys, C.; Link, A.; Hermann, M.; Eickhoff, M.; Stutzmann, M.; Bernardini, F.; Fiorentini, V.; Tilak, V.; Schaff, B.; Eastman, L. F. Pyroelectric Properties of Al(In)GaN/GaN Hetero- and Quantum Well Structures. *J. Phys. Condens. Matter* **2002**, *14* (13), 3399–3434. <https://doi.org/10.1088/0953-8984/14/13/302>.
- (49) Leroux, M.; Grandjean, N.; Laügt, M.; Massies, J.; Gil, B.; Lefebvre, P. Quantum Confined Stark Effect Due to Built-in Internal Polarization Fields in (Al, Ga)N/GaN Quantum Wells. *Phys. Rev. B - Condens. Matter Mater. Phys.* **1998**, *58* (20), R13371–R13374. <https://doi.org/10.1103/PhysRevB.58.R13371>.
- (50) Grandjean, N.; Damilano, B.; Dalmasso, S.; Leroux, M.; Laügt, M.; Massies, J. Built-in Electric-Field Effects in Wurtzite AlGaN/GaN Quantum Wells. *J. Appl. Phys.* **1999**, *86* (7), 3714–3720. <https://doi.org/10.1063/1.371241>.
- (51) Lefebvre, P.; Morel, A.; Gallart, M.; Taliercio, T.; Allègre, J.; Gil, B.; Mathieu, H.; Damilano, B.; Grandjean, N.; Massies, J. High Internal Electric Field in a Graded-Width InGaN/GaN Quantum Well: Accurate Determination by Time-Resolved Photoluminescence Spectroscopy. *Appl. Phys. Lett.* **2001**, *78* (9), 1252–1254. <https://doi.org/10.1063/1.1351517>.
- (52) Momma, K.; Izumi, F. VESTA 3 for Three-Dimensional Visualization of Crystal, Volumetric and Morphology Data. *J. Appl. Crystallogr.* **2011**, *44* (6), 1272–1276. <https://doi.org/10.1107/S0021889811038970>.
- (53) Okumura, H.; Misawa, S.; Yoshida, S. Epitaxial Growth of Cubic and Hexagonal GaN on GaAs by Gas-Source Molecular- Beam Epitaxy. *Appl. Phys. Lett* **1991**, *59* (9), 1058–1060. <https://doi.org/https://doi.org/10.1063/1.106344>.
- (54) Yang, H.; Brandt, O.; Ploog, K. MBE Growth of Cubic GaN on GaAs Substrates. *Phys. Status Solidi Basic Res.* **1996**, *194* (1), 109–120. <https://doi.org/10.1002/pssb.2221940112>.
- (55) Daudin, B.; Feuillet, G.; Hübner, J.; Samson, Y.; Widmann, F.; Philippe, A.; Bru-Chevallier, C.; Guillot, G.; Bustarret, E.; Bentoumi, G.; Deneuville, A. How to Grow Cubic GaN with Low Hexagonal Phase Content on (001) SiC by Molecular Beam Epitaxy. *J. Appl. Phys.* **1998**, *84* (4), 2295–2300. <https://doi.org/10.1063/1.368296>.
- (56) Gerthsen, D.; Neubauer, B.; Dieker, C.; Lantier, R.; Rizzi, A.; Lüth, H. Molecular Beam Epitaxy (MBE) Growth and Structural Properties of GaN and AlN on 3C-SiC(001) Substrates. *J. Cryst. Growth* **1999**, *200* (3), 353–361. [https://doi.org/10.1016/S0022-0248\(99\)00060-3](https://doi.org/10.1016/S0022-0248(99)00060-3).
- (57) Martinez-Guerrero, E.; Chabuel, F.; Jalabert, D.; Daudin, B.; Feuillet, G.; Mariette, H.; Aboughé-Nzé, P.; Monteil, Y. Growth Control of Cubic GaN and GaAIN (GaInN) Alloys by RHEED Oscillations. *Phys. Status Solidi Appl. Res.* **1999**, *176* (1), 497–501. [https://doi.org/10.1002/\(SICI\)1521-396X\(199911\)176:1<497::AID-PSSA497>3.0.CO;2-R](https://doi.org/10.1002/(SICI)1521-396X(199911)176:1<497::AID-PSSA497>3.0.CO;2-R).
- (58) Martinez-Guerrero, E.; Chabuel, F.; Daudin, B.; Rouvière, J. L.; Mariette, H. Control of the Morphology Transition for the Growth of Cubic GaN/AlN Nanostructures. *Appl. Phys. Lett.* **2002**, *81* (27), 5117–5119. <https://doi.org/10.1063/1.1527975>.

Bibliography

- (59) Schörmann, J.; Potthast, S.; As, D. J.; Lischka, K. In Situ Growth Regime Characterization of Cubic GaN Using Reflection High Energy Electron Diffraction. *Appl. Phys. Lett.* **2007**, *90* (4), 041918. <https://doi.org/10.1063/1.2432293>.
- (60) Lee, L. Y.; Frentrup, M.; Kappers, M. J.; Oliver, R. A.; Humphreys, C. J.; Wallis, D. J. Effect of Growth Temperature and V/III-Ratio on the Surface Morphology of MOVPE-Grown Cubic Zincblende GaN. *J. Appl. Phys.* **2018**, *124* (10), 105302. <https://doi.org/10.1063/1.5046801>.
- (61) Meier, F.; Protte, M.; Baron, E.; Feneberg, M.; Goldhahn, R.; Reuter, D.; As, D. J. Selective Area Growth of Cubic Gallium Nitride on Silicon (001) and 3C-Silicon Carbide (001). *AIP Adv.* **2021**, *11* (7), 075013. <https://doi.org/10.1063/5.0053865>.
- (62) Littmann, M.; Reuter, D.; As, D. J. Remote Epitaxy of Cubic Gallium Nitride on Graphene-Covered 3C-SiC Substrates by Plasma-Assisted Molecular Beam Epitaxy. *Phys. Status Solidi* **2023**, *260* (7). <https://doi.org/10.1002/pssb.202300034>.
- (63) Meier, F.; Littmann, M.; Bürger, J.; Riedl, T.; Kool, D.; Lindner, J.; Reuter, D.; As, D. J. Selective Area Growth of Cubic Gallium Nitride in Nanoscopic Silicon Dioxide Masks. *Phys. status solidi* **2023**, *260* (8). <https://doi.org/10.1002/pssb.202200508>.
- (64) Martinez-Guerrero, E.; Bellet-Amalric, E.; Martinet, L.; Feuillet, G.; Daudin, B.; Mariette, H.; Holliger, P.; Dubois, C.; Bru-Chevallier, C.; Nze, P. A.; Chassagne, T.; Ferro, G.; Monteil, Y. Structural Properties of Undoped and Doped Cubic GaN Grown on SiC(001). *J. Appl. Phys.* **2002**, *91* (8), 4983–4987. <https://doi.org/10.1063/1.1456243>.
- (65) Kemper, R. M.; Veit, P.; Mietze, C.; Dempewolf, A.; Wecker, T.; Bertram, F.; Christen, J.; Lindner, J. K. N.; As, D. J. STEM-CL Investigations on the Influence of Stacking Faults on the Optical Emission of Cubic GaN Epilayers and Cubic GaN/AlN Multi-Quantum Wells. *Phys. Status Solidi Curr. Top. Solid State Phys.* **2015**, *12* (4–5), 469–472. <https://doi.org/10.1002/pssc.201400154>.
- (66) Lee, L. Y.; Frentrup, M.; Vacek, P.; Kappers, M. J.; Wallis, D. J.; Oliver, R. A. Investigation of Stacking Faults in MOVPE-Grown Zincblende GaN by XRD and TEM. *J. Appl. Phys.* **2019**, *125* (10), 105303. <https://doi.org/10.1063/1.5082846>.
- (67) Vacek, P.; Frentrup, M.; Lee, L. Y.; Massabuau, F. C. P.; Kappers, M. J.; Wallis, D. J.; Gröger, R.; Oliver, R. A. Defect Structures in (001) Zincblende GaN/3C-SiC Nucleation Layers. *J. Appl. Phys.* **2021**, *129* (15). <https://doi.org/10.1063/5.0036366>.
- (68) Xiu, H.; Fairclough, S. M.; Gundimeda, A.; Kappers, M. J.; Wallis, D. J.; Oliver, R. A.; Frentrup, M. Polarity Determination of Crystal Defects in Zincblende GaN by Aberration-Corrected Electron Microscopy. *J. Appl. Phys.* **2023**, *133* (10). <https://doi.org/10.1063/5.0138478>.
- (69) Okumura, H.; Hamaguchi, H.; Koizumi, T.; Balakrishnan, K.; Ishida, Y.; Arita, M.; Chichibu, S.; Nakanishi, H.; Nagatomo, T.; Yoshida, S. Growth of Cubic III-Nitrides by Gas Source MBE Using Atomic Nitrogen Plasma: GaN, AlGaN and AlN. *J. Cryst. Growth* **1998**, *189–190*, 390–394. [https://doi.org/10.1016/S0022-0248\(98\)00321-2](https://doi.org/10.1016/S0022-0248(98)00321-2).

- (70) Koizumi, T.; Okumura, H.; Balakrishnan, K.; Harima, H.; Inoue, T.; Ishida, Y.; Nagatomo, T.; Nakashima, S.; Yoshida, S. Growth and Characterization of Cubic AlGaN and AlN Epilayers by RF-Plasma Assisted MBE. *J. Cryst. Growth* **1999**, 201–202, 341–345. [https://doi.org/10.1016/S0022-0248\(98\)01347-5](https://doi.org/10.1016/S0022-0248(98)01347-5).
- (71) Jonnard, P.; Capron, N.; Semond, F.; Massies, J.; Martinez-Guerrero, E.; Mariette, H. Electronic Structure of Wurtzite and Zinc-Blende AlN. *Eur. Phys. J. B* **2004**, 42 (3), 351–359. <https://doi.org/10.1140/epjb/e2004-00390-7>.
- (72) Goldys, E. M.; Godlewski, M.; Langer, R.; Barski, A. Surface Morphology of Cubic and Wurtzite GaN Films. *Appl. Surf. Sci.* **2000**, 153 (2), 143–149. [https://doi.org/10.1016/S0169-4332\(99\)00342-6](https://doi.org/10.1016/S0169-4332(99)00342-6).
- (73) Martinez-Guerrero, E.; Beneyton, R.; Adelmann, C.; Daudin, B.; Dang, L. S.; Mula, G.; Mariette, H. Modified Stranski-Krastanov Growth in Stacked Layers of Self-Assembled Cubic GaN/AlN Quantum Dots. *Phys. Status Solidi Appl. Res.* **2001**, 188 (2), 711–714. [https://doi.org/10.1002/1521-396X\(200112\)188:2<711::AID-PSSA711>3.0.CO;2-V](https://doi.org/10.1002/1521-396X(200112)188:2<711::AID-PSSA711>3.0.CO;2-V).
- (74) Gundimeda, A.; Rostami, M.; Frentrup, M.; Hinz, A.; Kappers, M. J.; Wallis, D. J.; Oliver, R. A. Influence of Al_xGa_{1-x}N Nucleation Layers on MOVPE-Grown Zincblende GaN Epilayers on 3C-SiC/Si(001). *J. Phys. D. Appl. Phys.* **2022**, 55 (17), 175110. <https://doi.org/10.1088/1361-6463/ac4c58>.
- (75) Iwahashi, Y.; Yaguchi, H.; Nishimoto, A.; Orihara, M.; Hijikata, Y.; Yoshida, S. RF-MBE Growth of Cubic InN Films on MgO (001) Substrates. *Phys. Status Solidi* **2006**, 3 (6), 1515–1518. <https://doi.org/10.1002/pssc.200565312>.
- (76) Lima, A. P.; Tabata, A.; Leite, J. R.; Kaiser, S.; Schikora, D.; Schöttker, B.; Frey, T.; As, D. J.; Lischka, K. Growth of Cubic InN on InAs(0 0 1) by Plasma-Assisted Molecular Beam Epitaxy. *J. Cryst. Growth* **1999**, 201, 396–398. [https://doi.org/10.1016/S0022-0248\(98\)01359-1](https://doi.org/10.1016/S0022-0248(98)01359-1).
- (77) Pacheco-Salazar, D. G.; Leite, J. R.; Cerdeira, F.; Meneses, E. A.; Li, S. F.; As, D. J.; Lischka, K. Photoluminescence Measurements on Cubic InGaN Layers Deposited on a SiC Substrate. *Semicond. Sci. Technol.* **2006**, 21 (7), 846–851. <https://doi.org/10.1088/0268-1242/21/7/003>.
- (78) Chichibu, S. F.; Sugiyama, M.; Kuroda, T.; Tackeuchi, A.; Kitamura, T.; Nakanishi, H.; Sota, T.; DenBaars, S. P.; Nakamura, S.; Ishida, Y.; Okumura, H. Band Gap Bowing and Exciton Localization in Strained Cubic In_xGa_{1-x}N Films Grown on 3C-SiC (001) by Rf Molecular-Beam Epitaxy. *Appl. Phys. Lett.* **2001**, 79 (22), 3600–3602. <https://doi.org/10.1063/1.1421082>.
- (79) Goldhahn, R.; Scheiner, J.; Shokhovets, S.; Frey, T.; Köhler, U.; As, D. J.; Lischka, K. Refractive Index and Gap Energy of Cubic In_xGa_{1-x}N. *Appl. Phys. Lett.* **2000**, 76 (3), 291–293. <https://doi.org/10.1063/1.125725>.
- (80) Kitamura, T.; Cho, S. H.; Ishida, Y.; Ide, T.; Shen, X. Q.; Nakanishi, H.; Chichibu, S.; Okumura, H. Growth and Characterization of Cubic InGaN Epilayers on 3C-SiC by RF MBE. *J. Cryst. Growth* **2001**, 227–228, 471–475. [https://doi.org/10.1016/S0022-0248\(01\)00745-X](https://doi.org/10.1016/S0022-0248(01)00745-X).

Bibliography

- (81) Müllhäuser, J. R.; Jenichen, B.; Wassermann, M.; Brandt, O.; Ploog, K. H. Characterization of Zinc Blende In_xGa_1-xN Grown by Radio Frequency Plasma Assisted Molecular Beam Epitaxy on GaAs (001). *Appl. Phys. Lett.* **1997**, *71* (7), 909–911. <https://doi.org/10.1063/1.119685>.
- (82) Sun, X. L.; Wang, Y. T.; Yang, H.; Zheng, L. X.; Xu, D. P.; Li, J. B.; Wang, Z. G. Strain and Photoluminescence Characterization of Cubic (In,Ga) N Films Grown on GaAs(001) Substrates. *J. Appl. Phys.* **2000**, *87* (8), 3711–3714. <https://doi.org/10.1063/1.372405>.
- (83) Holst, J.; Hoffmann, A.; Rudloff, D.; Bertram, F.; Riemann, T.; Christen, J.; Frey, T.; As, D. J.; Schikora, D.; Lischka, K. The Origin of Optical Gain in Cubic InGaN Grown by Molecular Beam Epitaxy. *Appl. Phys. Lett.* **2000**, *76* (20), 2832–2834. <https://doi.org/10.1063/1.126488>.
- (84) Pacheco-Salazar, D. G.; Li, S. F.; Cerdeira, F.; Meneses, E. A.; Leite, J. R.; Scolfaro, L. M. R.; As, D. J.; Lischka, K. Growth and Characterization of Cubic In_xGa_1-xN Epilayers on Two Different Types of Substrate. *J. Cryst. Growth* **2005**, *284*, 379–387. <https://doi.org/10.1016/j.jcrysGro.2005.07.049>.
- (85) Compeán García, V. D.; Orozco Hinostroza, I. E.; Escobosa Echavarría, A.; López Luna, E.; Rodríguez, A. G.; Vidal, M. A. Bulk Lattice Parameter and Band Gap of Cubic In_xGa_1-xN (001) Alloys on MgO (100) Substrates. *J. Cryst. Growth* **2015**, *418*, 120–125. <https://doi.org/10.1016/j.jcrysGro.2015.02.033>.
- (86) Orozco Hinostroza, I. E.; Avalos-Borja, M.; Compeán García, V. D.; Cuellar Zamora, C.; Rodríguez, A. G.; López Luna, E.; Vidal, M. A. Tuning Emission in Violet, Blue, Green and Red in Cubic GaN / InGaN / GaN Quantum Wells. *J. Cryst. Growth* **2016**, *435*, 110–113. <https://doi.org/10.1016/j.jcrysGro.2015.11.022>.
- (87) Chichibu, S. F.; Setoguchi, A.; Azuhata, T.; Müllhäuser, J.; Sugiyama, M.; Mizutani, T.; Deguchi, T.; Nakanishi, H.; Sota, T.; Brandt, O.; Ploog, K. H.; Mukai, T.; Nakamura, S. Effective Localization of Quantum Well Excitons in InGaN Quantum Well Structures with High InN Mole Fraction. *Phys. Status Solidi* **2000**, *180*, 321–326. [https://doi.org/10.1002/1521-396X\(200007\)180:1%3C321::AID-PSSA321%3E3.0.CO;2-E](https://doi.org/10.1002/1521-396X(200007)180:1%3C321::AID-PSSA321%3E3.0.CO;2-E).
- (88) Compeán-García, V. D.; Hernández-Vázquez, O.; García-Hernández, S. A.; Vidal, M. A. Critical Thickness as a Function of the Indium Molar Fraction in Cubic In_xGa_1-xN and the Influence in the Growth of Nanostructures. *Mater. Sci. Semicond. Process.* **2020**, *115* (105101). <https://doi.org/10.1016/j.mssp.2020.105101>.
- (89) Vilchis, H.; Compeán-García, V. D.; Orozco-Hinostroza, I. E.; López-Luna, E.; Vidal, M. A.; Rodríguez, A. G. Complex Refractive Index of In_xGa_1-xN Thin Films Grown on Cubic (100) GaN/MgO. *Thin Solid Films* **2017**, *626*, 55–59. <https://doi.org/10.1016/j.tsf.2017.02.016>.
- (90) Lemos, V.; Silveira, E.; Leite, J. R.; Tabata, A.; Trentin, R.; Scolfaro, L. M. R.; Frey, T.; As, D. J.; Schikora, D.; Lischka, K. Evidence for Phase-Separated Quantum Dots in Cubic Ingan Layers from Resonant Raman Scattering. *Phys. Rev. Lett.* **2000**, *84* (16), 3666–3669. <https://doi.org/10.1103/PhysRevLett.84.3666>.

- (91) Dunstan, D. J. Strain and Strain Relaxation in Semiconductors. *J. Mater. Sci. Mater. Electron.* **1997**, *8*, 337–375. <https://doi.org/10.1023/A:1018547625106>.
- (92) People, R.; Bean, J. C. Calculation of Critical Layer Thickness versus Lattice Mismatch for $\text{Ge}_{x}\text{Si}_{1-x}/\text{Si}$ Strained-Layer Heterostructures. *Appl. Phys. Lett.* **1985**, *47* (3), 322–324. <https://doi.org/10.1063/1.96206>.
- (93) Weimann, N. G.; Eastman, L. F.; Doppalapudi, D.; Ng, H. M.; Moustakas, T. D. Scattering of Electrons at Threading Dislocations in GaN. *J. Appl. Phys.* **1998**, *83* (7), 3656–3659. <https://doi.org/10.1063/1.366585>.
- (94) Kozodoy, P.; Ibbetson, J. P.; Marchand, H.; Fini, P. T.; Keller, S.; Speck, J. S.; DenBaars, S. P.; Mishra, U. K. Electrical Characterization of GaN P-n Junctions with and without Threading Dislocations. *Appl. Phys. Lett.* **1998**, *73* (7), 975–977. [https://doi.org/https://doi.org/10.1063/1.122057](https://doi.org/10.1063/1.122057).
- (95) Speck, J. S.; Rosner, S. J. Role of Threading Dislocations in the Physical Properties of GaN and Its Alloys. *Phys. B* **1999**, *273–274*, 24–32. <https://doi.org/10.4028/www.scientific.net/msf.353-356.769>.
- (96) Ayers, J. E. New Model for the Thickness and Mismatch Dependencies of Threading Dislocation Densities in Mismatched Heteroepitaxial Layers. *J. Appl. Phys.* **1995**, *78* (6), 3724–3726. <https://doi.org/10.1063/1.359952>.
- (97) Gay, P.; Hirsch, P. B.; Kelly, A. The Estimation of Dislocation Densities in Metals from X-Ray Data. *Acta Metall.* **1953**, *1* (3), 315–319. [https://doi.org/10.1016/0001-6160\(53\)90106-0](https://doi.org/10.1016/0001-6160(53)90106-0).
- (98) Dunn, C. G.; Koch, E. F. COMPARISON OF DISLOCATION DENSITIES OF PRIMARY AND SECONDARY RECRYSTALLIZATION GRAINS OF Si-Fe. *Acta Met.* **1957**, *5* (7), 548. [https://doi.org/https://doi.org/10.1016/0001-6160\(57\)90122-0](https://doi.org/https://doi.org/10.1016/0001-6160(57)90122-0).
- (99) Hasegawa, S. REFLECTION HIGH-ENERGY ELECTRON DIFFRACTION. In *Characterization of Materials*; John Wiley & Sons, Inc., 2012; pp 1925–1938.
- (100) Trejo-Hernández, R.; Casallas-Moreno, Y. L.; Gallardo-Hernández, S.; López-López, M. Crystalline Phase Purity and Twinning of Mg-Doped Zincblende GaN Thin Films. *Appl. Surf. Sci.* **2023**, *636*, 157667. <https://doi.org/https://doi.org/10.1016/j.apsusc.2023.157667>.
- (101) Yakimova, R.; Vasiliauskas, R.; Eriksson, J.; Syväjärvi, M. Progress in 3C-SiC Growth and Novel Applications. *Mater. Sci. Forum* **2012**, *711*, 3–10. <https://doi.org/10.4028/www.scientific.net/MSF.711.3>.
- (102) Kemper, R. M.; Schupp, T.; Häberlen, M.; Niendorf, T.; Maier, H.-J.; Dempewolf, A.; Bertram, F.; Christen, J.; Kirste, R.; Hoffmann, A.; Lindner, J.; Josef As, D. Anti-Phase Domains in Cubic GaN. *J. Appl. Phys.* **2011**, *110* (12), 123512. <https://doi.org/10.1063/1.3666050>.
- (103) Strite, S.; Ruan, J.; Li, Z.; Salvador, A.; Chen, H.; Smith, D. J.; Choyke, W. J.; Morkoç, H. An Investigation of the Properties of Cubic GaN Grown on GaAs by Plasma-assisted Molecular-beam Epitaxy. *J. Vac. Sci. Technol. B Microelectron. Nanom. Struct. Process. Meas. Phenom.* **1991**, *9* (4), 1924. <https://doi.org/10.1116/1.585381>.

Bibliography

- (104) Powell, R. C.; Lee, N. E.; Kim, Y. W.; Greene, J. E. Heteroepitaxial Wurtzite and Zinc-Blende Structure GaN Grown by Reactive-Ion Molecular-Beam Epitaxy: Growth Kinetics, Microstructure, and Properties. *J. Appl. Phys.* **1993**, *73* (1), 189–204. <https://doi.org/10.1063/1.353882>.
- (105) Haynes, W. M.; Lide, D. R.; Bruno, T. J. *CRC Handbook of Chemistry and Physics 97th Edition*; CRC Taylor & Francis Group.
- (106) Wright, S.; Kroemer, H. Reduction of Oxides on Silicon by Heating in a Gallium Molecular Beam at 800°C. *Appl. Phys. Lett.* **1980**, *36* (3), 210–211. <https://doi.org/10.1063/1.91428>.
- (107) Kaplan, R.; Parrill, T. M. REDUCTION OF SiC SURFACE OXIDES BY A Ga MOLECULAR BEAM : LEED AND ELECTRON SPECTROSCOPY STUDIES. *Surf. Sci.* **1986**, *176* (2–3), 45–52. [https://doi.org/https://doi.org/10.1016/0039-6028\(86\)90799-5](https://doi.org/https://doi.org/10.1016/0039-6028(86)90799-5).
- (108) Brown, A. S.; Losurdo, M.; Kim, T. H.; Giangregorio, M. M.; Choi, S.; Morse, M.; Wu, P.; Capezzuto, P.; Bruno, G. The Impact of SiC Substrate Treatment on the Heteroepitaxial Growth of GaN by Plasma Assisted MBE. *Cryst. Res. Technol.* **2005**, *40* (10–11), 997–1002. <https://doi.org/10.1002/crat.200410475>.
- (109) He, B. B. *Two-Dimensional X-Ray Diffraction*; 2018. <https://doi.org/10.1154/1.3427643>.
- (110) Wright, A. F. Elastic Properties of Zinc-Blende and Wurtzite AlN, GaN, and InN. *J. Appl. Phys.* **1997**, *82* (6), 2833–2839. <https://doi.org/10.1063/1.366114>.
- (111) Giessibl, F. J. Advances in Atomic Force Microscopy. *Rev. Mod. Phys.* **2003**, *75* (3). <https://doi.org/https://doi.org/10.1103/RevModPhys.75.949>.
- (112) García, R.; Pérez, R. Dynamic Atomic Force Microscopy Methods. *Surf. Sci. Rep.* **2002**, *47* (6–8), 197–301. [https://doi.org/https://doi.org/10.1016/S0167-5729\(02\)00077-8](https://doi.org/https://doi.org/10.1016/S0167-5729(02)00077-8).
- (113) Cazaux, J. From the Physics of Secondary Electron Emission to Image Contrasts in Scanning Electron Microscopy. *J. Electron Microsc. (Tokyo)*. **2012**, *61* (5), 261–284. <https://doi.org/10.1093/jmicro/dfs048>.
- (114) Seiler, H. Secondary Electron Emission in the Scanning Electron Microscope. *J. Appl. Phys.* **1983**, *54* (11). <https://doi.org/10.1063/1.332840>.
- (115) Klingshirn, C. F. *Semiconductor Optics*, 4th ed.; Springer Berlin Heidelberg, 2012.
- (116) Jentsch, S. A. Growth of Cubic InGaN Thin Film by Molecular-Beam Epitaxy over the Whole Composition Range, Justus-Liebig-Universität Gießen, 2023.
- (117) Sun, W.; Tan, C. K.; Tansu, N. III-Nitride Digital Alloy: Electronics and Optoelectronics Properties of the InN/GaN Ultra-Short Period Superlattice Nanostructures. *Sci. Rep.* **2017**, *7* (1), 1–8. <https://doi.org/10.1038/s41598-017-06889-3>.
- (118) Wang, P. Synthesis and Characterization of Gallium Nitride Study on Nanoparticles and Epitaxial Films, Justus-Liebig-Universität Gießen, 2023.

- (119) Cheng, K.; Leys, M.; Degroote, S.; Van Daele, B.; Boeykens, S.; Derluyn, J.; Germain, M.; Van Tendeloo, G.; Engelen, J.; Borghs, G. Flat GaN Epitaxial Layers Grown on Si(111) by Metalorganic Vapor Phase Epitaxy Using Step-Graded AlGaN Intermediate Layers. *J. Electron. Mater.* **2006**, *35* (4), 592–598. <https://doi.org/10.1007/s11664-006-0105-1>.
- (120) Matioli, E.; Weisbuch, C. Active Region Part A. Internal Quantum Efficiency in LEDs. In *III-Nitride Based Light Emitting Diodes and Applications, Topics in Applied Physics*; Seong, T. Y., Han, J., Amano, H., Morkoç, H., Eds.; Springer, 2013; Vol. 126. <https://doi.org/10.1007/978-94-007-5863-6>.
- (121) Fritze, S.; Dadgar, A.; Witte, H.; Bügler, M.; Rohrbeck, A.; Bläsing, J.; Hoffmann, A.; Krost, A. High Si and Ge N-Type Doping of GaN Doping - Limits and Impact on Stress. *Appl. Phys. Lett.* **2012**, *100* (12). <https://doi.org/10.1063/1.3695172>.
- (122) Deppe, M.; Gerlach, J. W.; Shvarkov, S.; Rogalla, D.; Becker, H. W.; Reuter, D.; As, D. J. Germanium Doping of Cubic GaN Grown by Molecular Beam Epitaxy. *J. Appl. Phys.* **2019**, *125* (9). <https://doi.org/10.1063/1.5066095>.
- (123) As, D. J.; Simonsmeier, T.; Schöttker, B.; Frey, T.; Schikora, D.; Kriegseis, W.; Burkhardt, W.; Meyer, B. K. Incorporation and Optical Properties of Magnesium in Cubic GaN Epilayers Grown by Molecular Beam Epitaxy. *Appl. Phys. Lett.* **1998**, *73* (13), 1835–1837. <https://doi.org/10.1063/1.122298>.
- (124) Dyer, D.; Church, S. A.; Jain, M.; Kappers, M. J.; Frentrup, M.; Wallis, D. J.; Oliver, R. A.; Binks, D. J. The Effect of Thermal Annealing on the Optical Properties of Mg-Doped Zincblende GaN Epilayers. *J. Appl. Phys.* **2021**, *130* (8). <https://doi.org/10.1063/5.0057824>.

Appendix

Supporting Information of Publication 2:

Overcoming the Miscibility Gap of GaN/InN in MBE Growth of Cubic In_xGa_{1-x}N

<https://pubs.acs.org/doi/10.1021/acسامي.3c06319>

Supporting information

Overcoming the Miscibility Gap of GaN/InN in MBE Growth of cubic In_xGa_{1-x}N

*M. F. Zscherp¹, S. A. Jentsch¹, M. J. Müller¹, V. Lider², C. Becker², L. Chen¹, M. Littmann³,
F. Meier³, A. Beyer², D. M. Hofmann¹, D. J. As³, P. J. Klar¹, K. Volz², S. Chatterjee¹,
J. Schörmann^{1*}*

1: Institute of Experimental Physics I and Center for Materials Research, Justus Liebig
University Giessen, Heinrich-Buff-Ring 16, D-35392 Giessen, Germany

2: Materials Science Center and Faculty of Physics, Philipps-University Marburg, Hans-
Meerwein-Strasse 6, D-35032 Marburg, Germany

3: Department of Physics, University Paderborn, Warburger Strasse 100, D-33098 Paderborn,
Germany

*Jörg Schörmann: Institute of Experimental Physics I and Center for Materials Research,
Justus Liebig University Giessen, Heinrich-Buff-Ring 16, D-35392 Giessen, Germany,
Email: Joerg.Schoermann@expl.physik.uni-giessen.de

Reflection high energy electron diffraction (RHEED)

The growth surface is monitored in-situ by RHEED. The RHEED images presented in Figure S1 are taken after 1 min of c-In_xGa_{1-x}N growth. Figure S1a) shows a streaky RHEED pattern of a sample with T_{growth} = approx. 600 °C, whereas Figure S1b) depicts a spotty RHEED pattern of a sample grown at T_{growth} = approx. 475 °C.

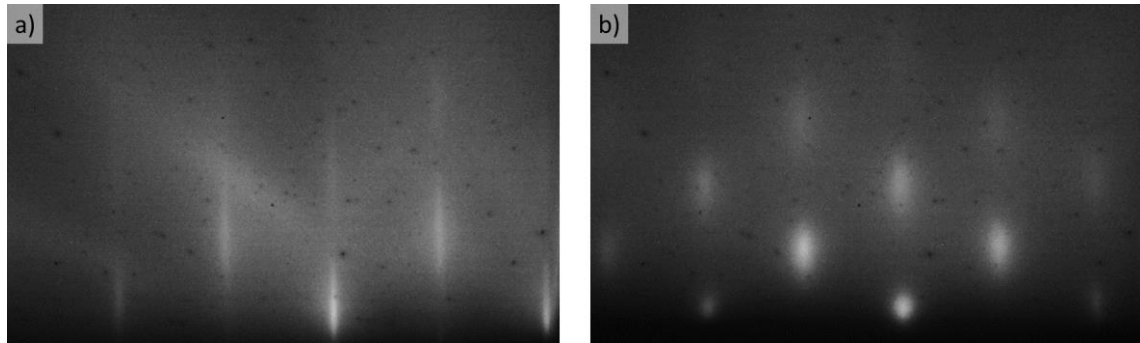


Figure S 1: RHEED images of c-In_xGa_{1-x}N layers approx. 1 min after growth start. A sample grown at T_{growth} = approx. 600 °C exhibits a streaky pattern (a), whereas a sample grown at T_{growth} = approx. 475 °C shows a spotty RHEED pattern (b).

Scanning transmission electron microscopy (STEM)

High resolution STEM image in high-angle annular darkfield (HAADF) mode of a c-In_xGa_{1-x}N layer with x(In) = 0.21 (Figure S2) which does not feature intensity fluctuations on 111 planes.

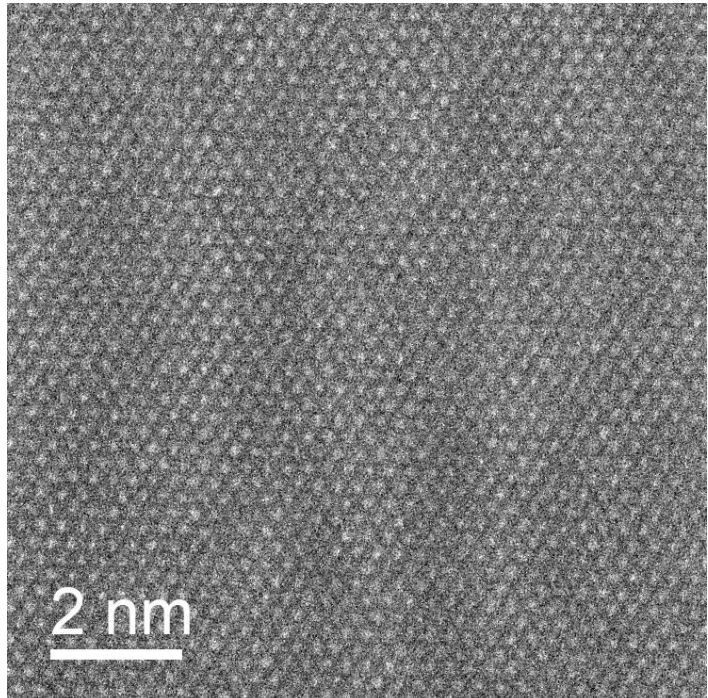


Figure S2: HR-HAADF image in [-110] direction of a c-In_xGa_{1-x}N layer with x(In) = 0.21 which does not exhibit CuPt-type ordering along 111 planes.

Selbstständigkeitserklärung

Ich erkläre:

Ich habe die vorgelegte Dissertation selbstständig und ohne unerlaubte fremde Hilfe und nur mit den Hilfen angefertigt, die ich in der Dissertation angegeben habe. Alle Textstellen, die wörtlich oder sinngemäß aus veröffentlichten Schriften entnommen sind, und alle Angaben, die auf mündlichen Auskünften beruhen, sind als solche kenntlich gemacht. Ich stimme einer evtl. Überprüfung meiner Dissertation durch eine Antiplagiat-Software zu. Bei den von mir durchgeführten und in der Dissertation erwähnten Untersuchungen habe ich die Grundsätze guter wissenschaftlicher Praxis, wie sie in der „Satzung der Justus-Liebig-Universität Gießen zur Sicherung guter wissenschaftlicher Praxis“ niedergelegt sind, eingehalten.

Gießen, 01.11.2023

Mario Fabian Zscherp

Danksagung

Ich möchte mich ganz herzlich bei allen bedanken, die zur Entstehung dieser Dissertation beigetragen haben. Insbesondere möchte ich mich bedanken bei:

Prof. Sangam Chatterjee, Ph.D. für die Möglichkeit diese Dissertation in seiner Arbeitsgruppe anzufertigen. Vielen Dank für das Vertrauen, den Input und die konstante Unterstützung, welche sehr zu meiner Weiterentwicklung und zum Gelingen dieser Arbeit beigetragen haben.

Dr. Jörg Schörmann für die exzellente Betreuung, die unkomplizierte Zusammenarbeit und die angenehme Reisegesellschaft. Danke, dass Du immer konstruktiv, wertschätzend und ansprechbar warst, wenn ich mit Kleinigkeiten vorbeigekommen bin oder aber der MBE meine Aufmerksamkeit nicht ausgereicht hat.

PD. Dr. Matthias T. Elm für das Erstellen des Zweitgutachten, die gute und angenehme Zusammenarbeit, sowie die Geduld mit den Ferriten. Du hast seit meiner Bachelorarbeit sehr viel zu meiner wissenschaftlichen Ausbildung beigetragen. Vielen Dank!

Prof. Dr. Kerstin Volz und Prof. Dr. Christian Heiliger für ihre Teilnahme an meiner Prüfungskommission.

Prof. Dr. Kerstin Volz und ihren Mitarbeitern Dr. Andreas Beyer und Vitalii Lider für mehrere Jahre sehr angenehmer und fruchtbare Kooperation. Danke für die zahlreichen STEM-Aufnahmen meiner Proben.

Prof. Dr. Donat J. As, Dr. Falco Meier und Mario Littmann für die gute Zusammenarbeit und den wertvollen Austausch auf dem einsamen Fachgebiet der kubischen Nitride.

Prof. Dr. Detlev M. Hofmann für den angenehmen Umgang und seine Unterstützung bei der Auswertung der PL-Ergebnisse, Prof. Dr. Peter J. Klar und Dr. Limei Klar für die Interpretation und Aufnahme der Raman-Spektren.

Danksagung

Meinen Kollegen, ehemaligen Kollegen und Freunden am I. Physikalischen Institut für die schöne gemeinsame Zeit inner- und außerhalb der Arbeitszeit, konstante Hilfsbereitschaft und unzählige spektroskopische Messungen mit denen ich Euch überfallen habe.

Meinen (ehemaligen) Bürokollegen Dr. Philip Klement, Lukas Gümbel, Silas Jentsch und Philipp Wang für die gute Atmosphäre und besonders Philip dafür, dass Du immer deine Weisheit mit mir geteilt hast.

Meinen ehemaligen Studenten Silas Jentsch und Philipp Wang, die außerdem durch ihre hervorragenden Abschlussarbeiten wichtige Beiträge zu meiner Forschung geleistet haben.

Dr. Hendrik Hemmelmann, Michele Bastianello und Elisa Monte für unsere deutsch-italienischen Abende und spontane Flurgespräche. Grazie mille, Elisa für das Erschaffen der Cover-Kunstwerke, die mir noch mal Zusatzmotivation zum Paperschreiben gegeben haben.

Meinen Kommilitonen Philip Keller, Dr. Till Fuchs, Dr. Timo Glaser und „Ehren-Mawi“ Fynn Kunze für die gemeinsamen Studienjahre, die durch euch immer Spaß gemacht haben und die tiefe Freundschaft, die sich daraus entwickelt hat.

Meiner Verlobten Simin, sowie meiner Familie und allen Freunden außerhalb der Uni, die mir immer ganz viel Kraft und Unterstützung gegeben haben.